THERMAL CONDUCTIVITY AT THE NANOSCALE: A MOLECULAR DYNAMICS STUDY

by

John W. Lyver, IV, C.S.P.

A Dissertation
Submitted to the
Graduate Faculty
of
George Mason University
in Partial Fulfillment of
The Requirements for the Degree
of
Doctor of Philosophy
Computational Sciences and Informatics

Committee:

_____	Dr. Estela Blaisten-Barojas, Dissertation Director
_____	Dr. Stephen G. Nash, Committee Member
_____	Dr. John Wallin, Committee Member
_____	Dr. Howard Sheng, Committee Member
_____	Dr. Dimitrios A. Papaconstantopoulos, Department Chairperson
_____	Dr. Richard Diecchio, Associate Dean for Academic and Student Affairs, College of Science
_____	Dr. Vikas Chandhoke, Dean, College of Science

Date: 07/12/2010

Summer Semester 2010
George Mason University
Fairfax, VA

Thermal Conductivity at the Nanoscale: A Molecular Dynamics Study

A dissertation submitted in partial fulfillment of the requirements for the degree of Doctor of Philosophy in Computational Science and Informatics at George Mason University

By

John William Lyver, IV
Master of Science in Computational Science
George Mason University, 2008
Master of Science in Electrical and Computer Engineering
George Mason University, 1988
Bachelor of Science
United States Naval Academy, 1978

Director: Estela Blaisten-Barojas, Professor
Department of Computational and Data Sciences

Summer Semester 2010
George Mason University
Fairfax, VA

DEDICATION

I dedicate this dissertation in loving memory of my parents, Geraldine and John W. Lyver, III.

ACKNOWLEDGEMENTS

I would like to thank my wife Sally, my children, John V (*GMU '10*) and Tom, and my stepchildren, Stephanie and Andrew, for their extreme love and support. I would like to thank the National Aeronautics and Space Administration, Office of Safety and Mission Assurance, for giving me the opportunity to pursue this degree. I would like to acknowledge the Computational Materials Science Center of George Mason University for providing me with the high performance computing facilities. I would also like to acknowledge Dr. Murray Black, Dr. Stephen Nash, Dr. John Wallin, and Dr. Howard Sheng, who have participated as committee members on this dissertation. Last, but not least, I would like to thank Dr. Estela Blaisten-Barojas for giving me the opportunity to be her student. It has been a privilege to study under one of the top educators and mentors in this field.

TABLE OF CONTENTS

a

LIST OF TABLES

LIST OF FIGURES

LIST OF ACRONYMS AND ABBREVIATIONS

AMM	Acoustic mismatch model
Ar	Argon
C	Carbon
CPU	Computer processing unit
CSP	Certified Safety Professional
DMM	Diffuse mismatch model
DOS	Density of states
E	Total energy
FCC	Face-centered cubic
g(r)	Radial distribution function
GK	Green–Kubo
K	Kelvin
LJ	Lennard-Jones
MATLAB®	MathWorks, Inc, product
MC	Monte Carlo
MD	Molecular dynamics
MSD	Mean square displacement
N	Number of particles
NE	Non-equlibrium
NEMD	Non-equilibrium molecular dynamics
NPT	Constant pressure, temperature and number of atoms ensemble

ODE	Ordinary Differential Equation
P	Pressure
PBC	Periodic Boundary Condition
PGHPF®	Portland Group High Performance Fortran
PGI®	Portland Group, Inc
Si	Silicon
T	Temperature
T_{cold}	Temperature of the cold bath
T_{hot}	Temperature of the hot bath
V	Volume
W	Watt
C_v	Specific heat at constant volume
$C(\tau)$	Correlation Function
eV	Electron volt
E_i	Total energy of each atom
$\vec{F}_{ij}$	Force for each atomic pair
k_B	Boltzmann's constant
$\vec{J}$	Thermal flux
J_{ph}	Thermal flux due to lattice contribution
ℓ	Mean free path
l_κ	Kapitza length
$p(x)$	Local linear momentum
r_{cut}	Cutoff radius
r_e	Electric conductivity
R_m	Ratio of mass between the reference atom and an atom of a different type
R_ε	Ratio of Lennard Jones interatomic strength parameters

R_σ	Ratio of Lennard Jones hard core parameters
$\vec{r}_{ij}$	Interatomic vectors for each atomic pair
$U(t)$	Energy of the computational box
$\vec{v}$	Particle velocity
$\vec{v}_i$	Velocity of each atom
Δt	Time step
$\Delta T_{interface}$	Temperature jump at the interface
Å	Angström
ε	Interatomic interaction strength
κ	Lattice thermal conductivity
κ_e	Electrical thermal conductivity
λ	Positional disorder factor
μ	Chemical potential
μVT	Grand canonical ensemble
ρ	Density
σ	Hard core radius
τ_{pbc}	Time for spatial translations to become periodic
τ_{relax}	Time correlation time
ω	Frequency
ω_c	Characteristic frequency
Ω_K	Thermal boundary resistance
$\vec{\nabla}T$	Temperature gradient

ABSTRACT

THERMAL CONDUCTIVITY OF NANOMATERIALS: A MOLECULAR DYNAMICS STUDY

John W. Lyver, IV, C.S.P., PhD

George Mason University, 2010

Dissertation Director: Dr. Estela Blaisten-Barojas, Ph.D.

With the growing use of nanotechnology and nanodevices in many fields of engineering and science, a need for understanding the thermal properties of such devices has increased. The ability for nanomaterials to conduct heat is highly dependent on the purity of the material, internal boundaries due to material changes and the structure of the material itself. Experimentally measuring the heat transport at the nanoscale is extremely difficult and can only be done as a macro output from the device.

Computational methods such as various Monte Carlo (MC) and molecular dynamics (MD) techniques for studying the contribution of atomic vibrations associated with heat transport properties are very useful. The Green–Kubo method in conjunction with Fourier's law for calculating the thermal conductivity, κ, has been used in this study and has shown promise as one approach well adapted for understanding nanosystems. Investigations were made of the thermal conductivity using noble gases, modeled with

Lennard-Jones (LJ) interactions, in solid face-centered cubic (FCC) structures. MC and MD simulations were done to study homogeneous monatomic and binary materials as well as slabs of these materials possessing internal boundaries. Additionally, MD simulations were done on silicon carbide nanowires, nanotubes, and nanofilaments using a potential containing two-body and three-body terms. The results of the MC and MD simulations were matched against available experimental and other simulations and showed that both methods can accurately simulate real materials in a fraction of the time and effort.

The results of the study show that in compositionally disordered materials the selection of atomic components by their mass, hard-core atomic diameter, well depth, and relative concentration can change the κ by as much as an order of magnitude. It was found that a 60% increase in mass produces a 25% decrease in κ. A 50% increase in interatomic strength produces a 25% increase in κ, while as little as a 10% change in the hard core radius can almost totally suppress a materials ability to conduct heat. Additionally, for two LJ materials sharing an interface, the atomic vibrations altering the heat energy depend on the type of internal boundary in the material. Mass increases across the interfacial boundary enhance excitation of the very low frequency (ballistic) vibrational modes, while the opposite effect is seen as increases in hard core radius and interatomic strength enhance excitation of higher frequency vibrational modes. Additionally, it was found that this effect was diminished for higher temperatures around half the Debye temperatures. In nanodevices and nanomachines, there is an additional factor that

degrades heat transport at the boundary. In fact, the interface induces a temperature jump consistent with a thermal resistance created by the boundary. It was found that the temperature jump, which is due to a boundary resistance, was significant in boundaries involving small mass changes, lesser in changes in hard core radii changes and even lesser for interatomic strength changes. The study of SiC nanowires and nanotubes showed that the structural changes produced vastly different κ. The κ in closely packed structures like nanowires and nanofilaments approximated that of the bulk SiC, yet were less sensitive to temperature than the 1/T relationship traditionally found in bulk systems. The more open nanostructures, like nanotubes, had vastly lower κ values and are almost totally insensitive to temperature variation.

The results of this study can be used in the design of nano-machines where heat generation and transport is a concern. Additionally, the design of nano-machines which transport heat like nano-refrigerators or nano-heaters may be possible due to a better selection of materials with the understanding of how the materials affect their nanothermal properties at the nano scale.

CHAPTER 1 INTRODUCTION

It is known that heat is transported better through solid materials that are pure and crystalline. Any type of impurity, defect, doping, void, or internal boundary within the material increases the resistance to heat transport, and thus, reduces the ability to transport thermal energy. With the growing interest in nanotechnology, the study of thermal conduction properties of systems with reduced dimensions, thin films, nanotubes, nanowires, and super lattices has increased. In nanomaterials and nanostructures, phenomena are highly dependent on the length scale where vibrations between nearest-neighbor atoms occur. The use of molecular dynamics (MD) and the Green–Kubo (GK) methods for calculating the thermal conductivity, κ, have shown promise as atomistic approaches for understanding nanosystems at the nanometer scale. For example, there are several recent calculations on pure noble gases with Lennard-Jones (LJ) interactions in which MD was the method of choice [1-5]. For binary crystals, the literature is not so abundant. There are over 6000 bi-atomic combinations of elements of which only a few hundred have been tested for their thermal conductivity. For some phenomena, such as thermoelectricity, to decrease the lattice thermal conductivity may increase the performance efficiency of the device by a factor of two or three.

In a crystal, and in nanostructures, the thermal conductivity is composed of two additive contributions: lattice, κ_{ph}, and electronic, κ_e. The lattice contribution captures

phenomena associated with lattice vibrations and phonon scattering and is dominated by the structural characteristics of the crystal or the nanostructure. The electronic contribution is proportional to the electric conductivity through the Wiedemann–Franz law [6-7]. The composition of a crystal affects the lattice symmetry characteristics and, consequently, the lattice vibrations. Therefore, the lattice contribution to the thermal conductivity in a crystal should reflect changes according to its composition. In contrast, κ_e is a function of the conduction properties and these are expected to remain almost constant for families of solids with similar compositional components. A phenomenon that reduces κ_{ph} produces an overall reduction of the thermal conductivity if the electric conductivity is not affected. In dielectrics, and the noble gases specifically, changes in κ_{ph} do not simultaneously affect the electronic conductivity.

The computational approach taken in this research is through atomic-level computer simulations using several simple models of binary LJ solids employing a variety of methodologies, including different types of MD and different types of Monte Carlo (MC) techniques. The simulations were expanded to MD investigation of silicon-carbide (SiC) nanostructures with a classical potential proposed by Vashishta [8]. The approach underlying this calculation, from an atomistic perspective, is linear response theory of many body systems. Under this approach, the lattice thermal conductivity is the "response" of a material to a time dependent perturbation, which is the thermal gradient established through it.

In this dissertation, research is presented which identifies various lattice changes and their effects on the thermal conductivity in binary LJ crystals. The study in this dissertation spans from changes in the lattice thermal conductivity due to atomic vibrations for binary crystals with compositional disorder, to size effects in SiC nanowires and nanotubes. This research work identified ranges of combinations of binary materials, disorder conditions, and nanodevice shapes and sizes which reduce the thermal conductivity of the simulated materials and may warrant further experimental work. This dissertation is organized as follows:

Chapter 2 presents an overview of the theory and methods. The chapter begins with an overview of the modeling techniques employed with the MC and MD simulations. Several of the statistical mechanics ensembles proposed by Gibbs are presented as to their applicability to the simulations addressed in this research. A discussion of the two model potentials of interaction employed in the study is included in this chapter. The work presented in chapters 3 and 4 uses the LJ potential (two-body forces), and the work in chapter 5 uses a model potential proposed by Vastisha [8] containing Coulomb two-body interactions and three-body terms. The next section of this chapter discusses the methods used to analyze the atomic configurations for parameters, including: computational box size in simulations, shape of the computational box, structural and thermodynamic quantities, pressure, order parameters, velocity distribution, mean square displacement, radial distribution functions, and the dynamical properties studied (heat flux, frequency, density of states, and thermal conductivity). The chapter continues with

a discussion of how a thermal gradient was produced across the computational box and finally presents a few conclusions on the methods used.

Chapter 3 presents the results of thermal conductivity as a function of temperature of homogeneous compositionally disordered binary crystals with atoms interacting through LJ potentials. The two species in the crystal differ in mass, hard-core atomic diameter, well depth and relative concentration. The isobaric MC was used to find the equilibration density of the samples at near-zero pressure and various temperatures. The isoenergy MD simulations combined with the Green–Kubo approach were taken to calculate the heat current time-dependent autocorrelation function and determine the lattice thermal conductivity of the sample. The chapter provides a step-by-step discussion of the process used in this phase of the research: (1) how the equilibrium crystal density was obtained for a near zero pressure simulation, (2) how the thermal conductivity was obtained, (3) how compositional disorder was modeled, and (4) how the models and methods were validated against experimental and other computational results. Next the chapter presents discussions of how each physical parameter effects the thermal conductivity (computational box size, changes in mass, hard core radius, and interatomic strengths, temperature, and density). The chapter concludes with a set of observations. This chapter is a synopsis of the work which was published in reference [9].

Chapter 4 contains results on the effects of internal boundaries on the thermal conductivity. The implementation of non-equilibrium molecular dynamics (NEMD) simulations is discussed in the context of determining the thermal conductivity effects of various monatomic and binary materials with internal boundaries. With this

computational strategy, a thermal bath was simulated on each side of the computational box and the Fourier law is used to determine κ. A thorough analysis of the heat contribution on the vibrations of atoms is discussed. Effects on the density of vibrational states due to the interface created between two types of solid LJ systems was investigated as a function of the atomic masses and model potential parameters. The chapter opens with a discussion of the setup and model validation, then proceeds with discussions of the effects of the interface between two LJ solids on the lattice vibrations due to material property changes (similar to those discussed in Chapter 3), as well as mutual orientation of the solid lattices. Further discussions present analyses of the thermal resistance as a function of temperature. The chapter concludes with a summary of conclusions obtained from the research. The results presented in Chapter 4 have been published in [10].

Chapter 5 contains a study of the thermal conductivity in SiC nanostructures. Within the past few years, extensive work has begun on the use of nanodevices in science. The nanodevices can consist of wires, pipes, storage tanks, motors, and pumps, just to name a few. Most of the initial work has been on the use of pure carbon nanowires and nanotubes. Recently, SiC highly ordered structures have begun to be synthesized. The research presented in this chapter is an expansion of the work presented in chapters 3 and 4, now specifically tailored to study SiC in various sizes of nanowires and nanotubes in both their armchair and zigzag chiral configurations. The thermal conductivity of these SiC nanostructures has not been experimentally tested as of today. Therefore, this work makes predictions for SiC nanostructures that will aid the laboratory researchers in their future measurements. This chapter discusses the processes used to determine the thermal

conductivity and determine if the nanostructure configuration was stable. The chapter concludes with a presentation of the results and conclusions. The results of this work are currently under review for publishing in [11].

Chapter 6 presents discussion of three computational challenges which include: (1) the counteracting of the effects of finite computational box sizes with the use of periodic boundary conditions (PBC), (2) software error handling used in the research, and (3) a discussion of the use of an energy balance test using the statistical deviations of the average atomic energies. The chapter also includes a brief overview of the software used in the computational and data analysis portions of the research.

Chapter 7 presents a summary of the results and conclusions from the methods, processes and results in this dissertation. Additionally, a discussion of how this research has contributed to the general body of knowledge within the study of thermodynamic properties within materials and nanodevices is presented.

The dissertation is supplemented by Appendix A, containing a copy of the published papers and Appendix B, containing sample original code developed along with the work. An extensive bibliography is presented after Appendix B.

CHAPTER 2 THEORY AND METHODS

2.1 MODELING

2.1.1 Background on Statistical Mechanics Simulations

Two simulation approaches are used in this research: Metropolis Monte Carlo (MC) and Molecular Dynamics (MD). The MC methods simulate how atoms will act/react as they seek thermal equilibrium using stochastically selected discrete changes of atomic positions for each atom in the computational box. MC methods in statistical physics model equilibrium and nonequilibrium thermodynamic systems by stochastic computer simulations. Starting from a description of the desired physical system in terms of modeling how atoms interact among themselves, pseudo-random numbers are used to construct the appropriate probability with which the various generated states of the system have to be weighted. For equilibrium systems, the probability is defined according to either the microcanonical, canonical, iso-pressure-iso-temperature, or grand canonical ensembles.

The purpose of MC simulations is to obtain numerically the ensemble averages of desired system properties. In practice, the implementation is simple and can be seen as a sequence of simulation steps that build a Markov chain. At each MC step, a single atom is selected and then relocated to a new position. The new position is determined by

randomly selecting a direction and moving the atom a predetermined distance in that direction. After moving the atom, the potential energy of the system is recalculated. The next step in the process is to determine if the movement should be accepted, or the atom returned to its previous position. The acceptance criterion depends on the statistical mechanics ensemble that is being simulated. The process is repeated until the desired equilibrium is reached.

MD simulations are similar to real experiments. In a laboratory experiment, a sample of the system to be studied is first prepared. Next the researcher "connects" the sample to a measuring instrument. Finally, the property is measured. In a MD simulation, one follows the same approach. First, a sample is prepared by selecting a model of how the atoms will interact between themselves. Next, the sample is placed in the instrument, which in MD means that the classical equations of motion of the atoms (ordinary differential equations (ODE)) need to be solved numerically. Once the coupled ODEs are solved, the process is repeated until the system no longer changes with time (equilibrium); then the actual measurements are taken. In MD, the measured quantities are expressed as time averages of the modeled quantities, once the system has reached thermal equilibrium.

In both simulation approaches, MC or MD, a computer experiment is performed, with the purpose of calculating the average value of desired properties. Average values are to be compared with measured properties in the laboratory. Average values with MC stochastic-based averages in MD are based on the knowledge of the probability of how

the atoms evolve in time. If the system under study is ergodic, both types of averages should be equal.

$$\langle A \rangle_{MD} = \bar{A}_{MC} \tag{1}$$

A system is ergodic when averages do not depend on the initial conditions.

The use of statistical mechanics allows the study of many body systems by computer simulations. Through experimentation, the parameters within the system (T, P, V, and N) can be measured as averages over the atoms in the system. Unfortunately, unless the experiment is carefully controlled, the measurement itself can disturb the system as a whole. For example, measuring the heat generated within a solid system can only be measured from the outside of the solid. Thus, what is actually happening internal to the solid becomes a postulate. Likewise, experimentation cannot measure instantaneous quantities for many properties like the velocity of a given atom at a given instant. Therefore, statistical mechanics simulations can be used to study properties at the atomic scale that experimentation cannot.

2.1.2 Gibbs Ensembles of Statistical Mechanics

To analyze a system by simulation, a set of thermodynamic parameters must be fixed. The more popular parameters used during the research to define ensembles include: number of particles (N), pressure (P), temperature (T), energy (E), volume (V), or density (ρ), and chemical potential (μ) [12-14]. Depending upon which of these fundamental parameters are kept constant, different types of probabilistic functions are associated to the thermodynamic states of the system. The four basic statistical mechanics ensembles

are microcanonical, canonical, isobaric-isothermal, and grand canonical. A brief description of how these ensembles are implemented in simulation is given in the following paragraphs.

For this dissertation, a combination of MC and MD methods were used. The MC was used for determining pressures and establishing base static parameters. The MD was used for dynamical properties in both equilibrium and NEMD methods.

2.1.2.1 NVE Ensemble

The NVE ensemble (a.k.a. micro-canonical ensemble) is defined by having a constant number of particles in a constant volume at a constant energy. This represents an isolated system and these systems are conservative [12-13]. This is the most commonly used ensemble in MD. Within an MD simulation, the motion is governed by the Hamilton equations of motion:

$$\frac{\partial H}{\partial \vec{r}_i} = -\vec{p}_i \;\; ; \;\; \frac{\partial H}{\partial \vec{p}_i} = -\vec{r}_i \tag{2}$$

where H is the Hamiltonian of the system, which has the general form

$$H = \sum_{i=1}^{N} \left(\frac{1}{2} p_i^2\right) + U(\vec{r}_1, \vec{r}_2, \ldots, \vec{r}_N) \tag{3}$$

Here N is the number of atoms in the system, m_i are the atomic masses, v_i are the atomic velocities, and U is the potential energy function which depends on the positions $\vec{r}_i$. The first term is the kinetic energy that depends on the linear momenta, $\vec{p}_i = m_i \vec{v}_i$.

The set of 6 N ODE's, Eqn (2), are coupled through U. There are many numerical methods used in the literature for their solution. In this research, the Verlet algorithm in its velocity form is adopted [15]. Thus, the ODEs are transformed into finite difference equations, such that for each coordinate, the two finite differences are:

$$x_i(t+dt) = x_i(t) + v_i(t)\Delta t + \frac{1}{2}\frac{F_{xi}(t)}{m_i}\Delta t^2 \tag{4}$$

$$v_{x_i}(t+dt) = v_{x_i}(t) + \left[\frac{F_{x_i}(t)+F_{x_i}(t+dt)}{2m_i}\right]\Delta t \tag{5}$$

where Δt is the time step adopted and $\vec{F}_i = -\vec{\nabla}_i U$. Equations (4) and (5) are iterated, starting with time $t = 0$, until the quantities that depend on both $\vec{x}_i(t)$ and $\vec{v}_i(t)$ do not change much with time.

A time averaged quantity A is obtained from

$$\langle A \rangle = \lim_{t_{total}\to\infty} \frac{1}{t_{total}} \int_0^{t_{total}} A\left(\vec{r}(t), \vec{p}(t)\right) dt \tag{6}$$

In practice t_{total} is finite. The numeric implementation of this integral is

$$\langle A \rangle = \frac{1}{M\Delta t} \sum_{k=1}^{M} A_k \Delta t \tag{7}$$

where Δt is the numeric time step and M is the number of time steps.

2.1.2.2 NVT Ensemble

In the NVT ensemble (a.k.a. canonical ensemble) the number of particles (N), volume (V), and temperature (T) are constant thermodynamic parameters. This ensemble is the

most commonly used in MC simulations. In practice, for MC simulations, the criterion for accepting a move is the following:

- ✓ If the potential energy of the system, U_{new}, after a move decreases (becomes more negative) with respect to the potential energy prior to the move, U_{old}, the move is accepted.

- ✓ If the potential energy of the system after the move (U_{new}) increases (becomes less negative) than the potential energy prior to moving (U_{old}), then the following test is performed to determine if the move is accepted:

$$probability\ (old \rightarrow new) = exp\left(-\frac{U_{old}-U_{new}}{k_B T}\right) \quad (8)$$

  where k_B is the Boltzmann constant and T is the temperature. If this probability is greater than a random number picked from a uniformly distributed set 0 to 1, then the move is accepted. Otherwise, the move is rejected, and the atom is returned to its previous position, and the previous energy U_{old} is kept for the system. It is very important that the random number generator used gives rise to a true uniform distribution of random numbers.

The MD simulations at constant temperature allowed the particles to move freely and interact and then the velocities are corrected via different methods referred to as thermostats to maintain temperature constant. Two algorithms are commonly used, the Anderson thermostat and the Nosé-Hoover thermostat [14]. However, there is the Hoover thermostat that is less computer processing intensive. In this research, the latter

was used. One starts from the definition of the temperature as an average value over time:

$$T = \frac{2}{3N}\langle\sum_{i=1}^{N} m_i v_i^2\rangle \quad (9)$$

where the sum is twice the total kinetic energy of the system of *N* atoms. This thermostat is set in such a way that the velocities are multiplied by a factor, *f*, in order to reach the desired temperature, $T_{desired}$. The factor is easily defined as $f = \sqrt{\frac{T_{desired}}{T}}$. Once the factor is defined, the velocities are multiplied by that factor. The *f* changes dynamically as the MD proceeds in time. After some time, the *f* sets to be very close to one.

2.1.2.3 NPT Ensemble

The NPT ensemble (a.k.a.; isobaric-isothermal ensemble) is defined as having a constant number of particles (N), constant pressure (P), and constant temperature (T). In MC simulations, the volume of the computational cell is changed at random with some frequency. The criterion for accepting or rejecting a particle move in the MC considers a different probability than in equation (8) because the volume of the computational cell is modified to maintain P constant. This is physically represented as a piston inside of a very large volume. The piston allows exchange of energy from and out of the computational box but does not permit atoms to escape. The piston moves in or out at a preset frequency.

The NPT ensemble implementation with MC includes the extra change in volume (from V_{old} to V_{new}) after each of the particles is moved in the same manner as they were moved

in the NVT ensemble. The potential energy of the resulting computational box is calculated and compared to the potential energy from immediately before the change. If the potential energy, $U_{new}(V_{new})$, decreases (become more negative), the change is accepted. If the potential energy is greater (less negative than the old potential energy $U_{old}(V_{old})$), then the following test is made:

$$probability(old \rightarrow new) =$$

$$exp\left(\frac{-1}{k_B T}\left(U_{new}(V_{new}) - U_{old}(V_{old})\right) + P(V_{new} - V_{old}) - \frac{N}{k_B T} ln\left(\frac{V_{new}}{V_{old}}\right)\right) \quad (10)$$

where P is the set pressure, N is the number of atoms, V_{new} and V_{old} are the volumes of the computational box before and after the move, respectively. If the resulting value of equation (10) is greater than a random number uniformly distributed between 0 and 1, then the move is accepted. Otherwise, the move is rejected and the volume and atomic positions are reset back to the values in the old step.

In MD simulations, the NPT is simulated by allowing the outer boundaries of the computational box to expand or contract based on the internal forces of the box.

2.1.2.4 μVT Ensemble

In this ensemble, (a.k.a. grand canonical ensemble) the chemical potential (μ), volume and temperature are fixed while particles are added or removed to maintain fixed chemical potential. This ensemble is mostly used in MC simulations and was not implemented in this research but is included in this listing for completeness. Physically,

this ensemble is good to simulate osmosis phenomena where particles can pass through a membrane wall.

2.2 INTERATOMIC POTENTIALS

During the research, two model potentials were adopted. The first was the LJ potential which modeled prototype rare gas systems where the interatomic forces contain a repulsive and a dispersive attractive component. The LJ potential is well suited for atoms without bonds such as the noble gasses. This model potential was used in the work presented in Chapters 3 and 4. A second potential used in the research was a potential for SiC introduced in refs [8, 16-18], containing terms including Coulomb interactions and three-body terms modeling covalent bonding between Si and C atoms.

2.2.1 Lennard-Jones Potential

A prerequisite of the atomic simulations is to have reasonable interatomic potentials to model the interactions between the atoms. A well known potential model: the LJ potential (equation 11) was used during the first two phases of the research for solid materials. The LJ describes dispersive classical interatomic forces at long range, and is strongly repulsive at short range. Figure 1 depicts the LJ model potential.

The LJ potential has two parameters: σ (hard core radius), which is the distance between the atom centers when the potential equals zero, and ε (interatomic strength), which is the

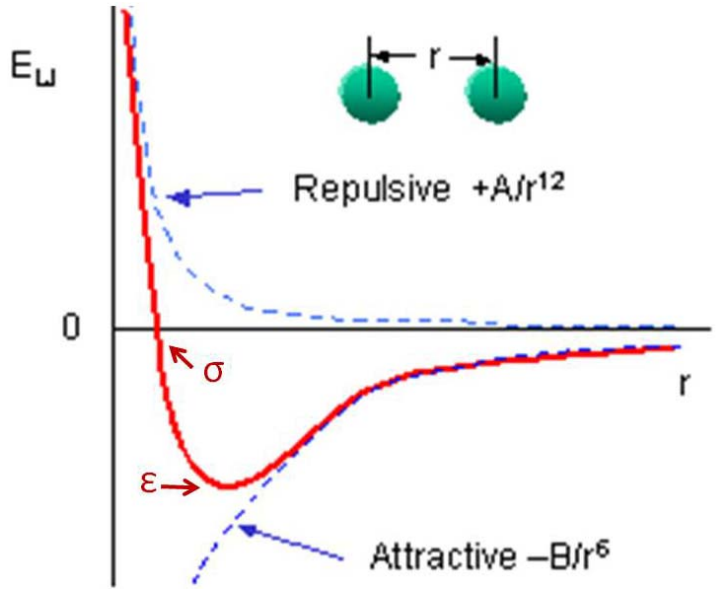

Figure 1: LJ Potential Model

depth of the attractive well (the lowest point of the potential in Figure 1). The LJ model is defined as:

$$u(r) = 4\varepsilon\left[\left(\frac{\sigma}{r}\right)^{12} - \left(\frac{\sigma}{r}\right)^{6}\right] \tag{11}$$

where r is the distance between two atoms, σ and ε are parameters depending on the material. In the simulations, a computational box containing N atoms at a given density is defined.

For a system of N atoms, the total potential energy when atoms interact through LJ is:

$$U = \sum_{i=1}^{N-1}\sum_{j>i}^{N} u(r_{ij}) \tag{12}$$

where $u(r_{ij})$ is the energy per atomic pair (equation 11), and r_{ij} is the distance between atoms *i* and *j*.

For monatomic solids, equation 12 gives the crystal potential energy. For binary solids (i.e. atoms of type A and atoms of type B), a combination rule for the parameters is considered. Now atoms of type A interact with atoms of type A with LJ that have parameters σ_A, and ε_A. Likewise, atoms of type B interact with LJ potentials that have parameters σ_B, and ε_B. The interactions between pairs AB are modeled by LJ potentials with parameters:

$$\sigma_{AB} = \frac{(\sigma_A + \sigma_B)}{2} \; ; \; \varepsilon_{AB} = \sqrt{\varepsilon_A \varepsilon_B} \tag{13}$$

Even though each pair interaction is represented very simply, there are three different pairs of interactions to be taken into consideration. Each pair carries different parameters. A solid system of binary nature (e.g. a binary alloy) is then composed of sums of three non-equivalent pair interactions for AA, BB, and AB.

2.2.2 Silicon Carbide Model Potential

This model potential includes both a two-body Coulomb interaction as well as a three-body interaction describing the covalent bonding between Si and C atoms. This was suggested by published work on Si grain boundaries (see section 4.1). The total potential energy of the system is given by

$$V = \sum_{i<j}^{N} V_{ij}^{(2)}(r_{ij}) + \sum_{i,j<k}^{N} V_{jik}^{(3)}(r_{ij}, r_{ik}) \tag{14}$$

where $V_{jik}^{(3)}$ is the three-body potential, and $V_{ij}^{(2)}$ is the two-body potential which is determined as

$$V_{ij}^{(2)}(r_{ij}) = \frac{H_{ij}}{r_{ij}^{\eta_{ij}}} + \frac{Z_i Z_j}{r_{ij}} e^{-r_{ij}/\lambda} - \frac{D_{ij}}{2{r_{ij}}^4} e^{-r_{ij}/\xi} - \frac{W_{ij}}{{r_{ij}}^6} \quad (15)$$

where H_{ij} is the strength of the steric repulsion of 23.67291 eVÅ^7 for Si-Si, 447.09026 eVÅ^9 for Si-C, and 471.74538 eVÅ^7 for C-C pairs, Z_i is the effective charge of +1.201 electron charges for Si and -1.201 for C, D_{ij} is the strength of the charge-dipole attraction of 2.1636 e^2Å^3 for Si-Si, 1.0818 e^2Å^3 for Si-C, and zero for C-C pairs, W_{ij} is the van der Waals strength of zero for Si-Si and C-C, and 61.4694 eVÅ^6 for Si-C pairs, η_{ij} is the exponent of the steric repulsion term of 7 for Si-Si and C-C, and 9 for Si-C interactions, λ and ξ are screening lengths of 5.0 Å and 3.0Å, and r_{ij} is the distance between the atoms i and j. A cutoff radius, r_{cut}, of 7.35Å is used as the longest distance up to which atoms interact for two-body interactions. The three-body potential $V_{jik}^{(3)}$ is determined as

$$\mathrm{V}_{\mathrm{jik}}^{(3)} = R^{(3)}(r_{ij}, r_{ik})\, P^{(3)}(\Theta_{jik}) \quad (16)$$

where $P^{(3)}$ is the bond-bending contribution and $R^{(3)}$ is the bond-stretching contribution of

$$R^{(3)}(r_{ij}, r_{ik}) = B_{jik} exp\left(\frac{\gamma}{r_{ij}-r_o} + \frac{\gamma}{r_{jk}-r_o}\right) \delta(r) \quad (17)$$

with B_{jik} being the strength of the interaction of 9.003 eV, γ is a unit conversion of 1Å, r_o is 2.90 Å and $\delta(r)$ is a step function limiting the maximum distance for three-body

interactions at r_o between the i-j or j-k atoms. The bond bending potential as

$$P^{(3)}\left(\Theta_{jik}\right) = \frac{\left(cos(\Theta_{jik}) - cos(\bar{\Theta})\right)^2}{1 + C_{jik}\left(cos(\Theta_{jik}) - cos(\bar{\Theta})\right)^2} \tag{18}$$

where Θ_{jik} is the bond angle between j-i-k atoms, $\bar{\Theta}$ is 109.47^o, and C_{jik} is a constant of 5.0. Even though the interior angle in a hexagon is 120^o, 109.47^o is the relaxed bond angle for a Si-C-Si or C-Si-C bond [8, 18]. The alternation of Si and C atoms was such that bonds of around 1.9 Å are the dominant majority, based on the model potential [8, 19-21].

2.3 UNITS

During the research described in Chapters 3 and 4, the work was done to derive relationships between model potential parameters and both dynamical and thermodynamic properties. By using dimensionless units (called "reduced units"), systems that can be modeled with the same model potential are addressed in a universal fashion, thus permitting an intrinsic saving of time and effort. Table 1 presents a summary of the reduced units used for systems modeled by LJ potentials. For example, for simulating the properties of a noble gas (neon, argon, krypton, xenon), all of these atoms are well modeled by the same LJ potential. As a result, it is not needed to repeat calculations for all of these elements. One simulation in appropriate reduced units will give universal results, which are valid for all noble gasses. Reduced units are obtained in terms of the parameters of the model potential. Table 1 gives the reduced units of

quantities used in Chapters 3 and 4. Quantities in reduced units are normally referred to by an asterisk super index. For deriving the reduced units of binary LJ systems, the actual units of one type of atom were selected as the reference atom and then the reduced units of the second/third atoms were determined in terms of the reference atom. Under these assumptions, the reduced units of the reference atom were nominally 1. The work described in Chapter 5 was done in real/physical units.

Table 1: Summary of reduced units for the LJ potential. Here k_B is the Boltzmann constant.

Quantity	**Unit**	**Reduced Units**
Energy (E)	ε	$E^* = E/\varepsilon$
Force (F)	$\frac{\varepsilon}{\sigma}$	$F^* = F\sigma/\varepsilon$
Length (x)	σ	$x^* = x/\sigma$
Mass (m)	m	$m^* = m/m = 1$
Time (t)	$t_0 = \sigma\sqrt{m/\varepsilon}$	$t^* = t/t_0$
Velocity (v)	$\sqrt{\varepsilon/m}$	$v^* = v\sqrt{m/\varepsilon}$
Particle Density (ρ)	$\frac{1}{\sigma^3}$	$\rho^* = \rho\sigma^3$
Temperature (T)	$\frac{\varepsilon}{k_B}$	$T^* = k_B T/\varepsilon$
Thermal Conductivity (κ)	$\frac{k_B}{t_o\sigma}$	$\kappa^* = \kappa\left(t_0\sigma/k_B\right)$

2.4 SIMULATION DETAILS

2.4.1 Boundary Conditions

The best calculations are done with very large systems that, in effect, are nearly infinite systems from a microscopic viewpoint. This is obviously not practical for computational resources because a lot of computer time is required for just one calculation point. Therefore, finite sized computational boxes were needed to be defined in Chapters 3 and 4 that would simulate actual infinite systems. To simulate infinite size samples with finite computational sized boxes in 1, 2, or 3 dimensions, periodic boundary conditions (PBC) were used. PBCs assume that a computational box is repeated periodically in each of the working space dimensions out to infinity. PBC replicate the entire box by a translation operator in each direction. For example a finite wire can be simulated as being infinitely long with PBC along its length direction. A finite cubic box can simulate an infinite 3D system by using PBC along the three coordinate axes. An effective numerical method to implement PBCs is the "minimum image convention." The algorithm allows inclusion of the actual computational box and its first shell of periodic images surrounding it. Furthermore, the implemented simulation will only calculate the forces for the minimum distance between the given atom and the real or image of the second atom. Therefore calculations will be limited to atoms (real or replicated) that are apart by less than half of the width of the computational box as the cutoff radius. For this research, 49% of the width of the computational box was used. Effectively, this is

achieved by introducing a cutoff distance in the forces. Thus, any two atoms separated by distances larger than the cutoff, do not interact.

When using PBCs, the simulation must be carefully set up such that the computational box is small enough to permit reasonable calculational times, yet large enough to not experience the edge effects of the computational box. For example, an edge effect would manifest itself in the study of a collective vibration with wave length longer than the size of the computational box. For the LJ simulations, it was determined that the computational box needed to be a minimum of 4 or 5 times the pattern of atoms in the unit cell of the FCC crystal. The effects were minimized by choosing a size of 5 times the FCC unit cell (Chapters 3 and 4) and 15 atomic planes in the case of the SiC nanostructures.

2.4.2 Cubic Computational Box

A homogeneous block of material was modeled with PBCs in all 3 directions. These blocks were used in both MC and MD methods. Simulations with these PBCs were used for the homogeneous mono- and binary materials described in Chapter 3.

2.4.3 Slab Computational Box

For simulations described in Chapter 4, a simulated 3-D infinite slab of material was modeled, which had a hot thermal bath on one side and a cold bath on the other. Figure 2 shows a schematic view of the infinite slab model. The computational box has periodic boundary conditions in the two dimensions perpendicular to the flow of energy (green

arrows on Figure 2). The third direction is connected to two simulated thermal baths creating a cold side and a hot side of the sample as shown in Figure 2. There are no PBC's in this direction. The region in between the thermal baths is divided into several sub-regions along the x-direction (which are referred to as "slices" in the remainder of this dissertation), as shown in Figure 3. This geometrical setup, plus the two thermal baths, produced a temperature gradient across the short direction within the analyzed material. Figure 3 shows an expanded view of the computational cell being modeled for the non-equilibrium MD (NEMD) studies. Because a constant gradient of temperature was maintained, there was a flux of energy flowing from the hot to the cold end.

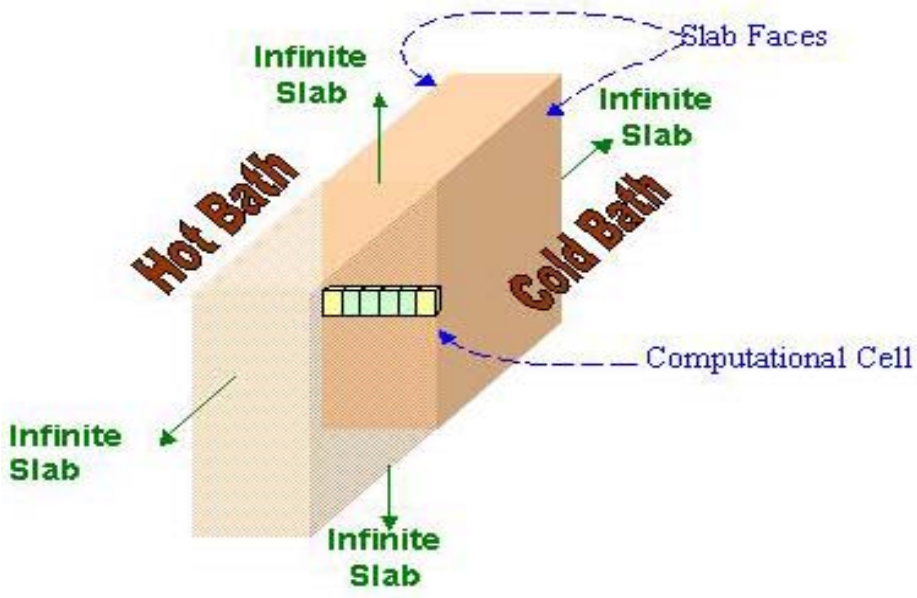

Figure 2: Schematic view of the computational box used in the NEMD studies of Chapter 4

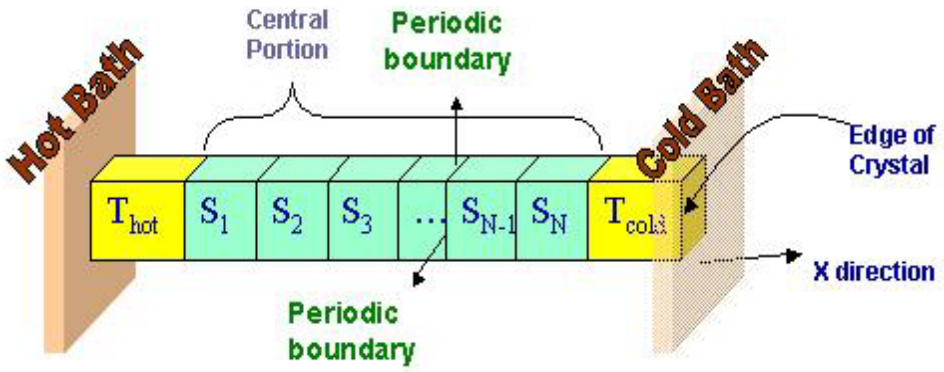

Figure 3: Expanded view of simulated system of slices for NEMD work with slabs

The thermal baths were modeled using an isothermal MD approach. Within each bath, the temperature was calculated for the bath atoms, then corrected, as described in 2.2.1 PBC's were not used in the direction of the thermal baths.

2.4.4 Nanostructures Computational Box

The simulation setup for the nanodevices was similar to the slab NEMD, except that a finite nanowire or nanotube was placed between the thermal baths. The PBC's were not used. The conventions used were the same as those for the slab computational box as shown in Figure 4, except PBC's were not used in any direction. Additionally, for the SiC nanostructures, a hard wall was used on each axial end of the nanostructure. This hard wall was simulated by not allowing motion to the atoms in the last plane in the axial direction at each end. The hard wall prevented the nanotubes from necking down as the nanotube slowly grew in length.

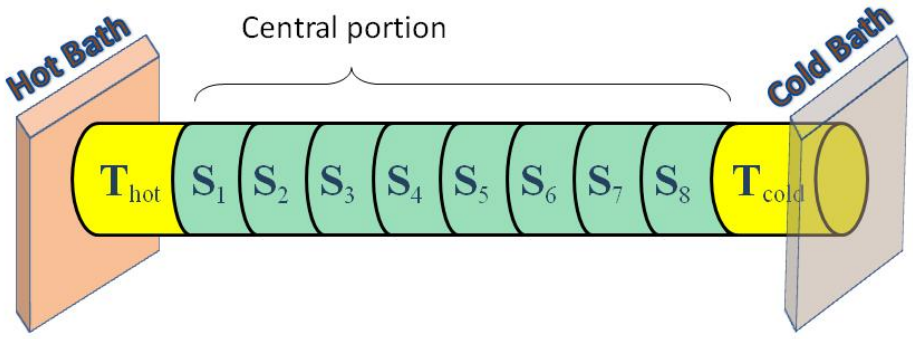

Figure 4: Expanded view of simulated system of slices for NEMD work with nanostructures described in Chapter 5

For these nanostructures, it was of paramount importance to first determine the length of the system. Systems that were too short failed to yield reliable data. On the average, the length of the central portion needed to be about 3.5nm or longer for the SiC nanowires and nanotubes.

2.5 STRUCTURAL AND THERMODYNAMIC QUANTITIES

Simulations must reach a state of thermal equilibrium. In equilibrium, the system has relaxed, and is away from the initial arbitrary configuration. In this dissertation, systems that are isolated (Chapter 3) or subjected to thermal gradients (Chapters 4 and 5) were considered. No other external forces were present. In all cases, the systems were first allowed to reach thermal equilibrium. For the slab and nanostructures, the thermal baths were set, once the system had reached equilibrium. Then, in these NEMD simulations, the infinite slab and nanostructures were further allowed to reach a steady state condition,

such that the heat flux was constant over time. Only then, could the data collection begin.

Several parameters were monitored to reach both thermal equilibrium and steady state heat flow as described in the following sections. The first 4 parameters described were found to be effective but were very computationally intensive as compared to monitoring the temperature stabilization.

2.5.1 Pressure

There are several different (but equivalent) ways to measure the pressure of a classical N-body system [12]. The most common among these is based on the virial equation for the pressure. The virial equation is:

$$P = \rho k_B T + \langle \frac{1}{Vd} \sum_{i<j}^{N} f(r_{ij}) \cdot r_{ij} \rangle \tag{19}$$

where P is the average system pressure, ρ is the system density, T is the average temperature, V is the volume, d is the dimensionality of the system, f is the force between atoms i and j at a distance r_{ij} and the brackets < > indicate either an ensemble average or a time average. The virial sum gave an indication of equilibrium in the MC simulations when it stabilized on a given pressure with small fluctuations.

2.5.2 Positional Order Parameter

Positional order parameter, λ, is a measure of the shift from the initial 'perfectly placed' locations in a crystalline configuration. λ was determined by comparing the current

atoms position to atoms placed in a perfect FCC lattice. When the values of λ stabilized, then the system was approaching equilibrium. For atoms in the FCC lattice, λ gives a measure of how close or far from the FCC the system is. The λ is calculated as:

$$\lambda_\alpha = \frac{1}{N}\sum_i^N \cos\frac{4\pi\alpha_i}{a} \tag{20}$$

where α is x, y, or z and a is the lattice constant.

2.5.3 Boltzmann's H-function

At thermal equilibrium, the velocity distribution of the atoms in the computational box should be Maxwellian [14]. Thus the atomic momenta p_i are distributed according to the following function:

$$N(p) = \int N(r,p)dr = \frac{N}{C} exp\left(-\frac{p^2}{2mk_BT}\right) \text{ or } f(v_x) = \frac{N}{C} exp\left(-\frac{mv_x{}^2}{2k_BT}\right) \tag{21}$$

where C is a constant that ensures normalization. The Boltzmann H-function is defined as:

$$H_x(t) = \int_{-\infty}^{\infty} f(v_x) ln\big(f(v_x)\big)\, dv_x \tag{22}$$

where v_x is the x component of the velocity. The H-function requires an update of the function $f(v_x)$ given in equation (21) as the MD simulation progresses. Because for an isolated system equilibrium is the most probable state, and because the Maxwell distribution of velocities $f(v_x)$ is positive and normalized, then $ln\big(f(v_x)\big)$ is negative, and as a function of time, the H-function should decrease and have a negative value.

2.5.4 Mean Square Displacement (MSD)

The mean square displacement (MSD) is defined as the time average of the square of the distance between the initial position r_o and the current position of each atom. When the time averaged MSD becomes stable, then the atoms (on average) are vibrating around a constant position and, therefore, equilibrium is reached [14]. On the other hand, the MDS grows linearly with time, according to Einstein's relation of diffusion.

$$\langle |r - r_o|^2 \rangle \equiv MSD \propto \frac{Dt}{2d} \tag{23}$$

where D is the coefficient of self diffusion and d the dimensionality of the system. In simulation, one deals with a finite size computational box; therefore, a particle can only diffuse as much as the size of the box. Figure 5 is an example of a LJ system in the liquid state. At short time intervals, the linear dependence is clear. However, after about 0.08

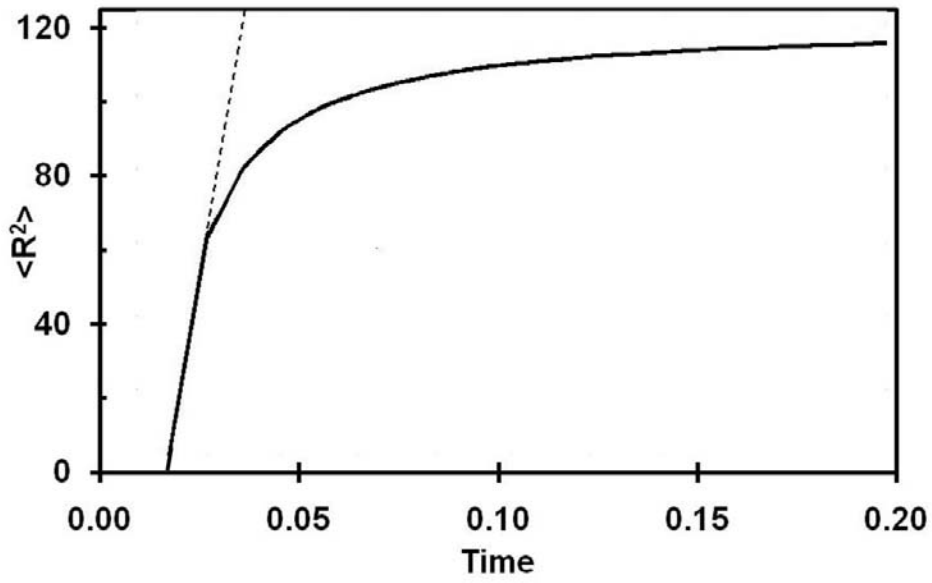

Figure 5: MSD as a function of time for a LJ fluid

time units, the particles have reached the size of the box cannot go further away, and the MSD reaches its maximum possible value.

2.5.5 Temperature Stabilization

The temperature stabilization was perhaps the best determination that thermal equilibrium was reached. The temperature profile would either be a constant for equilibrium runs or would develop a slope as a function of position for the non-equilibrium runs.

During the equilibrium runs, the atom velocities were scaled by a factor to reset the temperature to the desired temperature (or profile) at periodic intervals. This trick was implemented to be dynamic. The frequency of scaling was initially set to be a nearly every time step. As the scaling factor changed to near 1, the frequency of the scaling was decreased. The process of scaling was terminated when the scaling factor would be 10^{-5} away from 1. This process gave a speedup to calculations, saving well over half of the CPU time required to reach an equilibrium or steady state condition.

2.5.6 Pair Distribution Function

The pair distribution function, $g(r)$, is a signature of the structure in an N-body system. The $g(r)$ represents the probability of finding atoms at distances r away from any given atom in the system. The following equation was used:

$$g_\alpha = \frac{\sum_{k=1}^{M} N_k(r,\Delta r)}{M\left(\frac{1}{2}N\right)\rho V(r,\Delta r)} \tag{24}$$

where N_k is the number of distances between r and $r + \Delta r$ at time $k\Delta r$, M is the total number of time steps used, ρ is the system number density, and $V(r, \Delta r)$ is the volume between two spheres, one of radius r and the other of radius r+Δr. Here α is an atom pair type (A-A, A-B, B-B), $N(r_\alpha)$is the number of atom pairs at distance r apart, Δr is the binning width. Figure 6 is a sample plot for a liquid binary mixture at a low temperature (T=36K) at equilibrium. The $g(r)$ for type A to type A atoms is shown by the solid line, A-B atoms is the short dash line, and B-B atoms is represented by the long dash line. $g(r)$ gave an indication of equilibrium being reached when the function stabilized with the predicted plotted peak values.

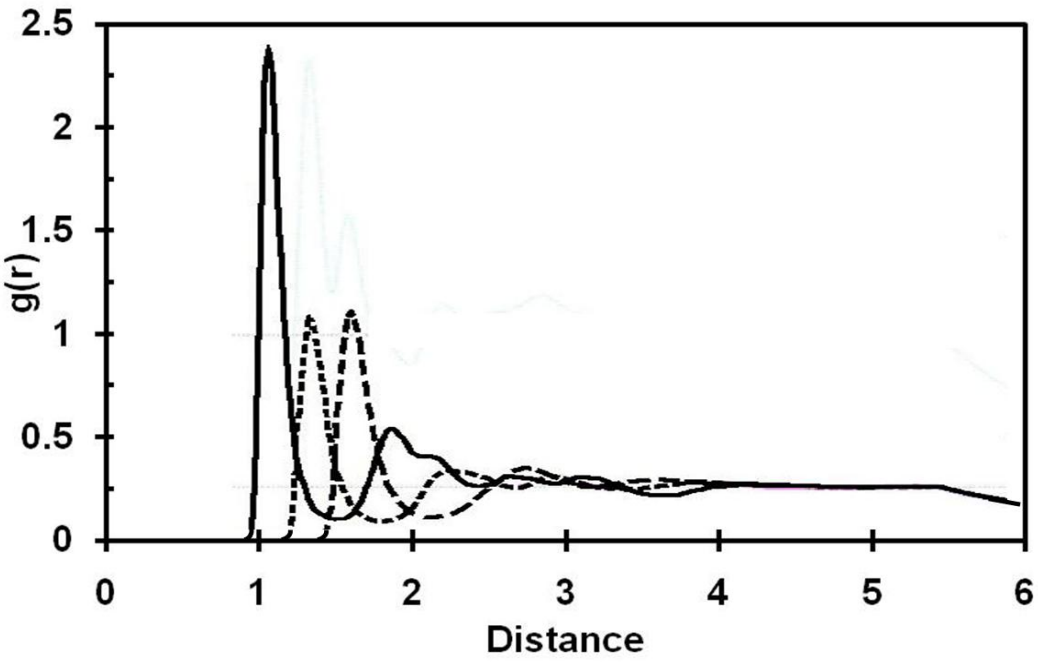

Figure 6: Pair correlation function as a function of distance for a binary LJ system at T=36K, ρ=0.382. Solid line is for A-A atoms, short dashed line is for B-B atoms and long dashed line is for A-B atoms.

2.6 DYNAMICAL PROPERTIES

Several dynamical functions were employed in the research as described in this section.

2.6.1 Time Dependent Correlation Function and Green-Kubo Formalism

A dynamical approach to calculate the thermal conductivity, κ, is based on the Green-Kubo (GK) formula [22-23]. The GK expression relates the two-times autocorrelation function, $C(\tau)$, of the heat current, $\vec{J}(\tau)$, to the thermal conductivity, κ [13, 24-26]:

$$C(\tau) = \frac{\langle \vec{J}(t+\tau)\vec{J}(t)\rangle}{\langle J(t)^2\rangle} \tag{25}$$

where the angular brackets <.> indicate an average at thermal equilibrium, $\vec{J}(t)$ is the heat current at a given time, and $\vec{J}(t+\tau)$ is the heat current at τ time later. The correlation function describes the memory decay of a system property as a function of time. For this work, the desired thermal property was the thermal conductivity:

$$\kappa = \frac{1}{3Vk_BT^2}\int_0^\infty C(\tau)d\tau \tag{26}$$

where V is the volume of the sample, k_B is Boltzmann's constant, and T is the temperature.

The GK approach works well for both amorphous and crystalline models, as long as the system is homogeneous. GK takes full account of anharmonic properties, but is classical in nature.

Ladd, et al. [24] were the first to use the GK formalism to calculate thermal conductivity for solids with interactions following an inverse-twelfth power law potential. Later, Gillan extended this method for the study of $\vec{J}$ in palladium doped with hydrogen [27]. More recently, Chen et al. used this same approach to study the thermal conductivity of pure Ar doped with Xe [28].

The proportionality between a transport coefficient, such as κ, and the associated time correlation function of a quantity coupled to the external force producing the transport process, is a general result of linear response theory. It was first demonstrated to be applicable to the transport of heat when Mori [29] introduced the concept of "local thermal equilibrium." Indeed, when a heat current is flowing through a material, the solid is not in thermal equilibrium. However, the system is locally close to being in thermal equilibrium. Small regions within the material may be thought to be in thermal equilibrium, thus having the same T. It is only under that assumption that equation (26) is valid.

A generalization for an isotropic system is to consider the tensor $\kappa_{\alpha\beta,}$ where α and β are the coordinates x, y, z.

2.6.2 Heat Flux

The heat flux (a.k.a. J_i) across the computational box was monitored as the sample approached the steady state condition. The conduction of heat occurs through flow of energy and can be expressed as a vector in terms of the dynamical variables $\vec{r}$, $\vec{p}$ of each

atom. The heat current operator assumes the following microscopic expression [13, 24, 30-32]:

$$J_\alpha(r,p) = \sum_{i=1}^{N}\left[\frac{p^2}{2m_i} + \frac{1}{2}\sum_{j\neq i}^{N} u(r_{ij})\right]\left(\frac{p_{i\alpha}}{m_i}\right) + \frac{1}{2}\sum_{i=1}^{N}\sum_{j\neq i}^{N}\left[\left(\frac{\vec{p}_i}{m_i}\right)\cdot F_{ij}\right] r_{ij\alpha} \quad (27)$$

where α = x,y,z, the p_i are the momenta of atoms with mass m_i, $u(r_{ij})$ are the interatomic potential energies, and F_{ij} are the forces between atoms i and j. Equation (27) can be simplified to [30]:

$$\vec{J} = \sum_{i=1}^{N} \mathrm{E_i}\,\vec{v}_i + \frac{1}{2}\sum_{i=1}^{N}\sum_{j\neq i}^{N}(\vec{v}_\mathrm{i}\cdot\vec{F}_{ij})\,\vec{r}_{ij} \quad (28)$$

where E_i is the total energy of each atom, and $\vec{v}_i$ is its velocity.

In the NEMD, one is interested in the flow of thermal energy along the direction that has the applied thermostats (Figures 2, 3, and 4). Although the heat flux perpendicular to this axis (J_y and J_z) is not relevant to the calculation of κ, checking that the transversal components were small ensured that the NEMD simulation was reliable. Small values for the J_y and J_z were due to the round-off errors and truncated variables in the simulation. Therefore, when the cross term heat currents calculated were on the order of 0.1% to 5% of the longitudinal heat current, the runs were considered to be good.

2.6.3 Vibrational Spectrum from a Classical Approach

Phonons are quanta of lattice vibrations. In MD simulations, phonons are not explicitly calculated, yet their properties can be simulated from the movements of the atoms in the system [5]. The vibrational spectrum of the monatomic case (all atoms are of type A)

was determined from the time dependent autocorrelation function of velocities of each atom and then taking a Fourier transform (FT). The resulting FT is proportional to the absorption spectrum of the system [33].

The velocity autocorrelation function, $C_{vel}(\tau)$, and Fourier transform are:

$$C_{vel}(\tau) = \sum_{i=1}^{N} \langle \vec{v}_i(t+\tau) \cdot \vec{v}_i(t) \rangle \tag{29}$$

$$\tilde{C}_{vel}(\omega) = \frac{1}{2\pi} \int_{-\infty}^{\infty} e^{-i\omega\tau} C_{vel}(\tau) d\tau \tag{30}$$

Atomic velocities in each direction were used from a time period of about 2^{14} steps. The data was divided into 16 discrete sections and the $C_{vel}(\tau)$ taken for each, in each of the three directions. The $C_{vel}(\tau)$ values were calculated then padded with zeros as the input to the Fourier transform. The Fourier transform was taken on the resulting values and then averaged and normalized over the entire range. The resulting histogram showed the density of states of vibrational modes.

Figure 7a shows a typical result of $\tilde{C}_{vel}(\omega)$ for the entire frequency range and with an expansion of the scales in Figure 7b showing the peaks more clearly. This density of states (DOS) changes with temperature. To study the thermal effect, runs were made at three temperatures, 7.5K, 17.5K, and 27.5K. Table 2 shows the frequency at peak values of DOS of vibrational states for the three temperatures, for the case of Ar, $\varepsilon = 120K$ and $\sigma = 3.4$Å. Values of ω were obtained by realizing that for a Δt=0.05*2.15 10^{-12} sec and 256 points in the FFT, the $\Delta\omega = \frac{2\pi}{256*\Delta t}$ was approximately 20 THz. Similar results are reported in [5] of the phonon spectrum for solid Ar in the near infrared region.

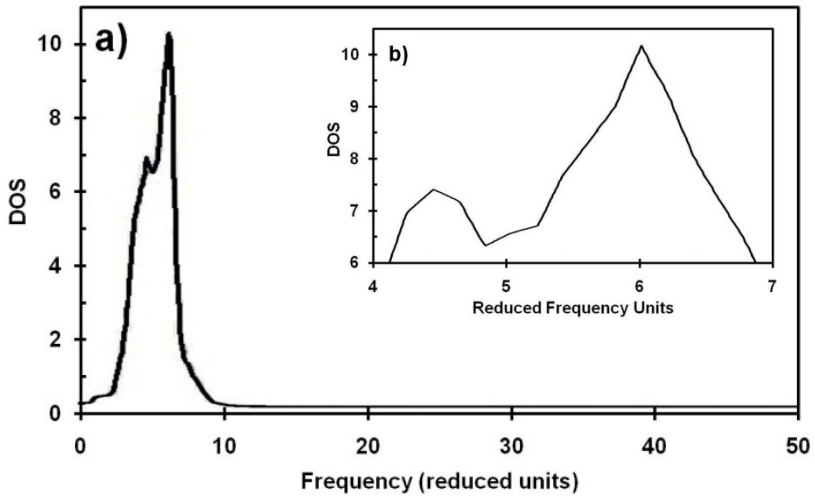

Figure 7: Typical DOS of vibrational states for a 50:50 solid mixture of LJ atoms at T=0.167

Table 2: Frequency of the peaks in the vibrational spectrum for argon

Temperature	Frequency of the highest peak	Frequency of the secondary peak
27.5K	3.35 10^{13} Hz	2.50 10^{13} Hz
17.5K	3.3 10^{13} Hz	2.39 10^{13} Hz
7.5K	3.26 10^{13} Hz	2.39 10^{13} Hz

The results match those experimentally determined for argon in [34].

2.7 NON-EQULIBRIUM MD SIMULATIONS

In 1958, Mori [29] proposed a crucial concept for the development of the statistical mechanics of non-equilibrium systems, systems where the temperature of the system is

not the same in all points of space. If the macroscopic quantities vary very slowly over a mean free path between collisions, then these same collisions quickly drive the system to a state that is as close as possible to the thermal equilibrium state. Mori defined the concept of a "local equilibrium." The local equilibrium concept is simple to understand if one thinks that the one-particle velocity distribution probability is of Maxwell type, but the five fundamental parameters of thermodynamics -- density, $\rho(x)$, local linear momentum, $p(x)$, and the energy depend slowly on space (x) and time. An instantaneous state of the system deviates only slightly from local equilibrium. What Mori did was to extend the local equilibrium concept from the one-particle distribution to the complete N-body distribution. The reader should remember that the atomic description of the heat current operator, equations (27) and (28), are valid for non-equilibrium systems.

The heat flux, $\vec{J}$, may be thought as the net amount of energy transported across unit area in unit time when the system is under a thermal gradient, e.g., in contact with two reservoirs at temperatures T_{hot} and T_{cold} (see Figures 2 and 3). Then the local equilibrium average of $\vec{J}$ becomes proportional to the local gradient of temperature T, following the Fourier law:

$$\vec{J} = \frac{\langle \vec{J} \rangle_{local}}{V_{local}} = -\kappa \langle \vec{\nabla} T \rangle_{local} \tag{31}$$

The lattice thermal conductivity, κ, of a solid, is then defined as the coefficient of proportionality between the steady-state flow of heat and the temperature gradient within the material. Fourier's law implies that the thermal energy transfer within the material is

a random process and thus behaves as a diffusive quantity undergoing many collisions along its travel through the material. The underlying partial differential equation representing this behavior is the heat conduction equation, which is a diffusion equation:

$$\rho C_v \, {d\varepsilon}/{dt} = \kappa \nabla^2 \varepsilon(\mathrm{r}, \mathrm{t}) \tag{32}$$

where $\varepsilon(\mathrm{r}, \mathrm{t})$ is the energy above the average energy, ρ is the mass density of the material, and C_v is the specific heat at constant volume. This is the continuum representation of the process of heat conduction. In the literature, instead of $\varepsilon(\mathrm{r}, \mathrm{t})$, one finds the temperature, T, but the two quantities are proportional, because, from a microscopic approach, the solid is given an atomistic description, such that the total energy of N atoms is,

$$\mathrm{E}(\mathrm{r}, \mathrm{t}) = \sum_{\mathrm{i}=1}^{\mathrm{N}} [\varepsilon_{\mathrm{i}} - \langle \varepsilon_{\mathrm{i}} \rangle] \delta(\mathrm{r} - \mathrm{r}_{\mathrm{i}}) \tag{33}$$

here r_i is the instantaneous position of every atom and δ is the Dirac delta function. This means that the thermal energy being conducted is now scattered by an array of vibrating atoms.

CHAPTER 3 THERMAL CONDUCTIVITY STUDY OF BINARY LENNARD-JONES SYSTEMS

3.1 INTRODUCTION

The focus of this portion of the research work was to investigate the lattice thermal conductivity of binary crystals with compositional disorder. It is known that heat is transported better through solid materials that are pure and crystalline. Any type of impurity, defect, doping, or internal boundary within the material increases the resistance to heat transport, and thus, reduces the ability to conduct thermal energy. With the growing interest in nanotechnology, the study of thermal conduction properties of systems with reduced dimensions and super lattices has increased. In nanomaterials and nanostructures, phenomena are highly dependent on the length scale where vibrations between nearest neighbor atoms occur. The use of MD with Green-Kubo (GK) approach has shown promise as an atomistic approach to understand the thermal conductivity of nanoscale systems. For example, there are several recent calculations on pure noble gasses with LJ interactions in which MD simulations were the method of choice [1-5]. The present work focused on identifying ranges of disorder conditions which reduce the lattice thermal conductivity, κ, of the simulated binary solids and may warrant further experimental work.

The effect of disorder on thermal conductivity was investigated using several simple models of binary LJ solids. Disorder was investigated due to differences in the LJ parameters of hard core radius (σ), interatomic bond strength (ε), and mass (m) of the atoms in the system. Several relative concentrations of simulated binary mixtures were studied as a function of selected potential parameters and analyzed across various temperatures. The computational approach taken was to perform atomic-level computer simulations employing a combination of isoenergy MD and NPT MC to calculate the κ within the GK approach of many body systems (see section 2.6.1). To validate the work, results were compared to other reported results and experimentation available for monatomic crystals of noble gases.

3.1.1 Setup

A crystalline binary mixture of 500 atoms was simulated in a cubic computational box with periodic boundary conditions (PBC) in each direction. The LJ potential was used as a prototype interaction between atoms. In the calculations, the cutoff radius, r_c, was taken as 49% of the width of the computational box. The compositional disorder introduced in the reference lattice due to the guest atoms is modeled parametrically by changes of σ, ε, and mass. The system is homogeneous since the A and B atoms are distributed at random within the sample as shown in Figure 8. The composition of the binary crystal uses atoms of type ‘‘A’’ as the reference and atoms of type ‘‘B’’ as the guest. There are three types of LJ parameters: (1) atoms of type A have LJ parameters σ_A and ε_A; (2) atoms of type B interact through LJ potentials with parameters σ_B and ε_B; (3)

interactions between A and B atoms are modeled with LJ parameters σ_{AB} and ε_{AB} (see section 2.2.1). All parameters were compared relative to the reference A atoms. Quantities are expressed in reduced units with respect to the reference atoms' LJ parameters (σ_A, ε_A and m_A) (See section 2.3). Densities considered correspond to solid mixtures.

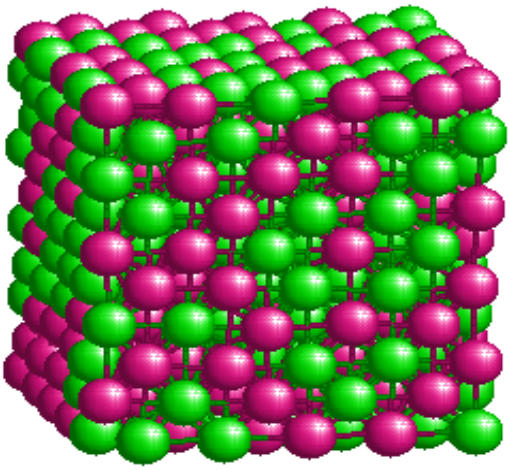

Figure 8: Schematic view of a compositionally disordered binary LJ solid with a 50:50 mixture of green and red atoms

Four compositional mixture cases were considered with the following characteristics: 100% of pure A atoms, 75% of A atoms and 25%B atoms, 50% of each type, and 25% of A atoms and 75% of B atoms. Simulations started at a reduced temperature of 0.5 from a configuration with atoms placed in a perfect FCC lattice. Next, an initial atom type assignment was constructed such that atoms were randomly assigned as type A or B consistent with the desired relative concentration of the two types of atoms. Throughout

this study, to indicate the ratio of parameters, the symbols R_σ, R_ε, and R_m are used for σ_B/σ_A, $\varepsilon_B/\varepsilon_A$, and m_B/m_A, respectively.

The system was equilibrated by NPT MC, which allowed for moves of the atoms in random directions and changes of the entire computational box volume (V). The acceptance criterion between old (V_{old}) and new (V_{new}) configurations is given by [12] (see equation 10 in section 2.1.2.3 . The equilibrium density of the binary system was then obtained for several temperatures.

The NPT MC simulations were run between 1 and 3 million steps, with each step being a single atom movement of each atom and one volume adjustment. The density and other calculated quantities were determined as averages over the final quarter of the NPT MC run. Therefore, the final position of the atoms within the box is consistent with this average density. The average density is defined as $N/\langle V \rangle$ irrespective of the types of atoms. Because the computational box is finite, the value of the pressure was adjusted by subtracting the pressure that would be exerted by a structureless infinite-sized sample outside of the computational box [12].

For the monatomic system, the equilibrium structure was FCC for all temperatures considered. At low temperatures, no stable amorphous phase was found. The result is consistent with those previously reported in Ref [3]. Because the NPT MC calculation does not include the mass in the simulation, the equilibrium ρ for binary samples with A and B atoms having equal σ and only different ε is the same as the density of the monatomic system. Therefore, the NPT MC calculations were carried out to determine ρ

at different temperatures when $R_\sigma \neq 1$. Figure 9 shows the temperature behavior of the average ρ for equilibrated systems at zero pressure for samples with a 50:50 relative concentration. The curves correspond to different R_σ. The value of ρ of pure Ar reported in Ref. [3] compares well with the results. As expected, when R_σ increases, the volume must also increase, decreasing ρ. The standard deviation (SD) of the average density is very low, of the order of the symbol size used in Figure 9. These small fluctuations certainly ensure that the decrease of ρ with temperature illustrated in Figure 9 is indeed realistic.

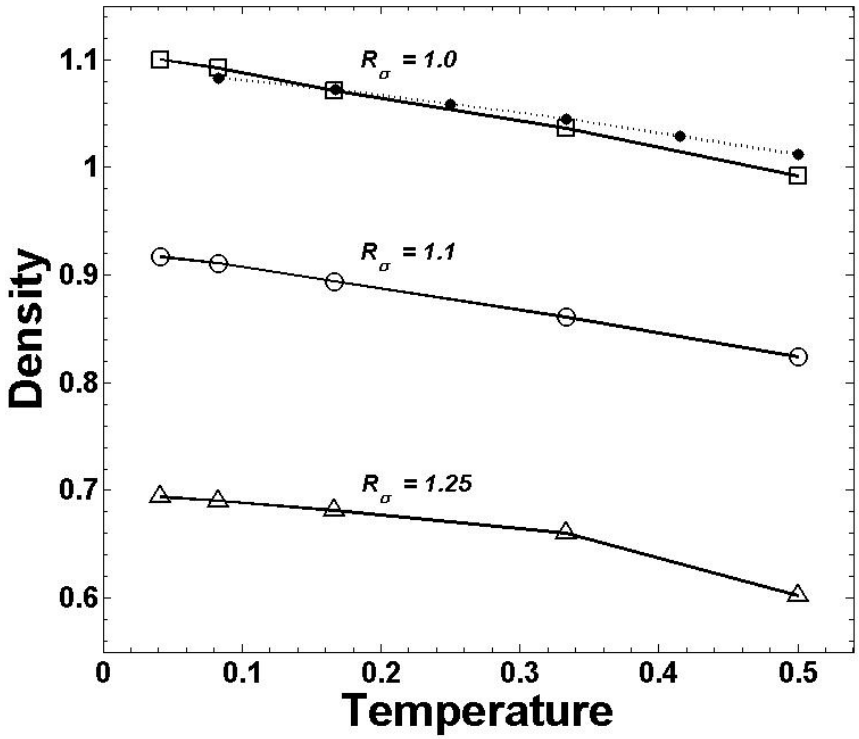

Figure 9: Density as a function of temperature for the binary LJ system with 50:50 relative concentration. Quantities are in reduced units.

3.1.2 Determining Thermal Conductivity

The next step was to initiate the isoenergy MD study using the output of the NPT-MC runs. Each MD trial was run 350,000 time steps of $\Delta t = 0.005$ to allow the system first to equilibrate at the desired temperature, then run for another half a million time steps to calculate the desired heat current operator values. Next was to calculate the time dependent autocorrelation function, $C(\tau)$, of the heat current operator (see sections 2.6.1 and 2.6.2). Each autocorrelation function run typically used 2^{14} time steps. It was found that for R_σ, R_ε, and R_m near a value of one, required longer times to compute the autocorrelation function than when disorder sets in.

The κ was obtained by integrating $C(\tau)$ over the range of $[0, t_{traj}]$, according to equation (25) where t_{traj} is the total time for which the autocorrelation function was calculated. Optimally, it would be best to calculate $C(\tau)$ out to an infinitely long trajectory instead of just the finite trajectory length, but this is not possible numerically. It was observed that $C(\tau)$ could be approximated as shown in Figure 10 by an exponentially decaying cosine function, $e^{-\zeta' t}\cos(\zeta t)$, and fit the parameters ζ and ζ' to the numerical MD results. Then the integration in equation (26) was done from the actual simulation data for $0 \le \tau \le t_{fit}$ and used the decaying cosine function for $t_{fit} \le \tau \le \infty$. The value t_{fit} of was set to be 1.25 times the period of the fitted cosine function. The time $1/\zeta'$ defines the correlation relaxation time. In Figure 10, t_{fit} was about 5.5 time units.

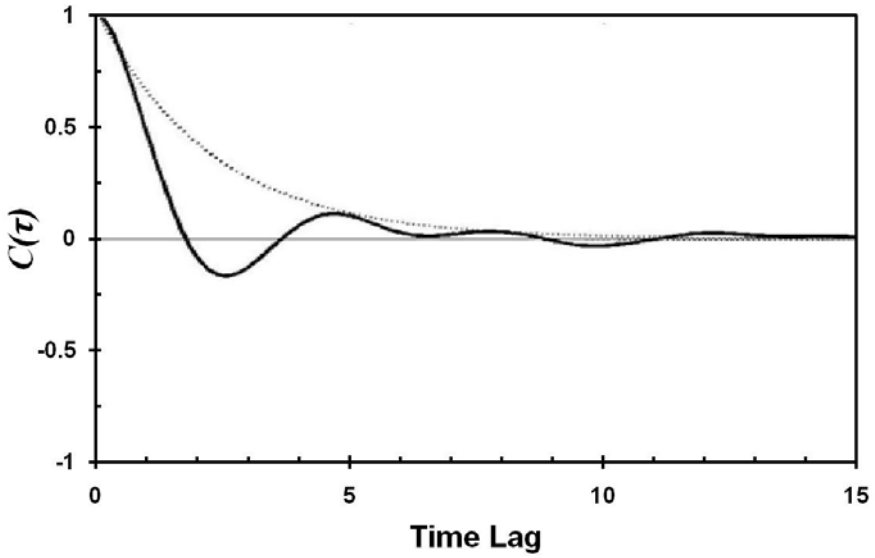

Figure 10: Calculated time dependent autocorrelation function of the heat current operator as a function of time lag

3.1.3 Computational Disorder

The NPT MC samples prepared in the manner described in previous paragraphs represent different types of compositional disorder. For all values of R_ε and R_m simulated, but keeping $R_\sigma = 1$, the structure of the equilibrated sample is the FCC lattice. Thus the system disorder is based on a random mixture of atoms A and B which are positioned on a perfect lattice. In contrast, when size disorder was introduced with $R_\sigma > 1.1$, the FCC lattice collapses. This is shown in Figure 11 (top) which depicts the pair correlation function g(r) of a 50:50 mixture sample at $T = 0.0167$ with $R_\varepsilon = 1$ and $R_m = 1$ and three different R_σ values (1.0, 1.1 and 1.25 – solid, dashed, dotted lines, respectively) (See section 2.5.6) in which the $g_{AA}(r)$, $g_{AB}(r)$ and $g_{BB}(r)$ values have been depicted

together. Note that the subscripts in g(r) indicate which type of atoms the distance was measured for. Figure 11(bottom) shows the same case as the top with a scaling of $\rho^{1/3}$ applied to the distance dependence. It is very clear that for $R_\sigma = 1.25$ (dotted line), the compositional disorder of the 50:50 sample affects the structure very significantly and the FCC crystal collapses into a homogeneous amorphous solid. The structure of this amorphous solid mixture is very different from the structure found in atomic clusters [35], where the atoms with smaller σ segregated and formed a subcluster surrounded by the large σ atoms.

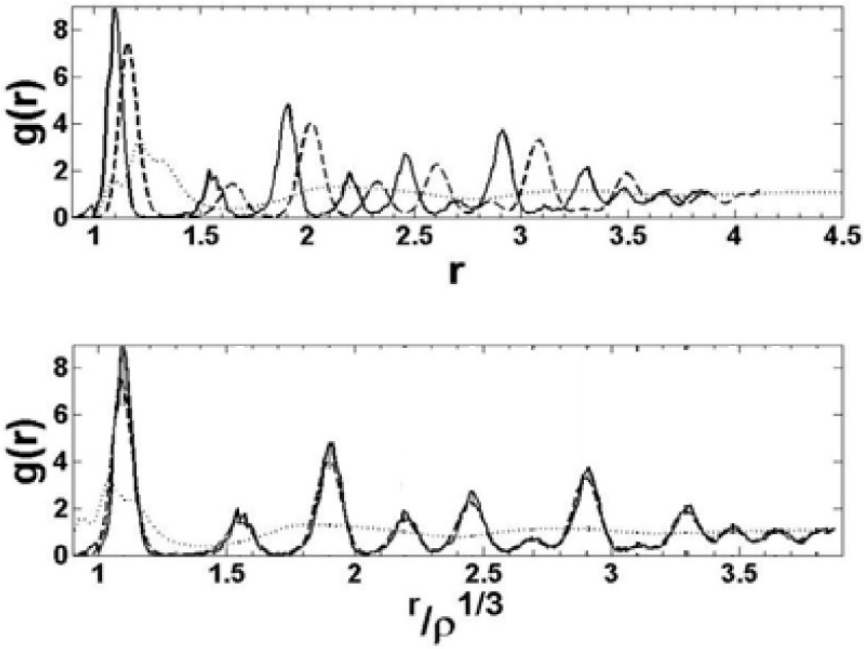

Figure 11: Pair distribution function of a 50:50 mixture at T=0.167: (top) g(r) vs. interatomic distance, (bottom) same results as in (a) as function of scaled distances by $\rho^{1/3}$. Solid lines are g_{AA}, dashed lines are g_{BB}, and dotted lines are g_{AB}

3.2 DETERMINATION OF THE LATTICE THERMAL CONDUCTIVITY

3.2.1 Calibration of Results

A sample with 500 atoms ($N = 4n^3$ where n is the number of FCC cells on each direction) with only one type of atom was prepared, and κ was obtained for several temperatures using the steps described in section 3.1.2. These results allowed a validation of the method by comparison with several calculations done in [3, 24, 27, 35] as well as with experimental results [36]. Figure 12 shows this comparison, indicating that the results (✱) are in full agreement with previous calculations and with the experimental results presented in Ref. [3] (◊), Ref. [28] (○), Ref. [25] (Δ), Ref. [36] (+), Ref. [37] (□), and follows the expected inverse power relationship as a function of temperature.

In the GK approach, there is an implicit dependence of κ on the volume of the sample. Sample size effects were studied in Ref. [25] where the authors considered computational box sizes containing between 108 and 4000 atoms. Those authors concluded that for Ar in the temperature domain of 20–70 K, the size effects are irrelevant for all practical purposes when calculating κ for a pure Ar system. This is consistent with the findings for computational cells containing 108–2048 atoms. It was found that computational boxes smaller than 108 atoms were too small for meaningful results. Figure 13 illustrates the dependence of the equilibrium system density, κ, and potential energy averages as a function of the number of FCC cells (n) that build the computational box edge. The

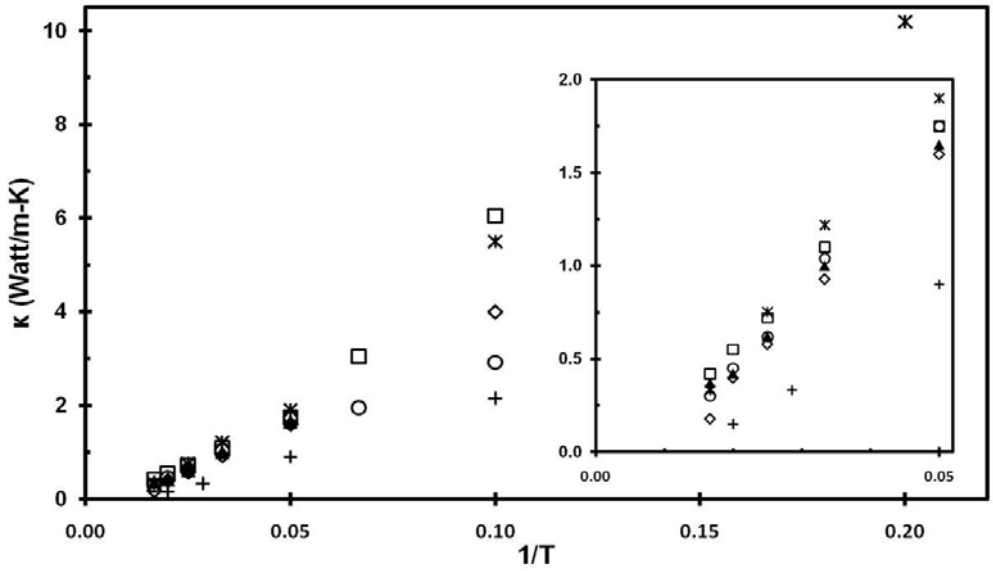

Figure 12: Thermal conductivity as a function of temperature (⁎) compared to other theoretical and experimental works for pure Ar at zero pressure. Inset is expansion of region near (0,0) {Ref. [3] (◊), Ref. [28] (○), Ref. [25] (Δ), Ref. [36] (+), Ref. [37] (□)}

number of atoms is $N = 4n^3$. The study further ensures that results of κ with systems containing roughly 500 atoms are reliable.

3.2.2 Thermal conductivity of binary mixtures as a function of the compositional disorder

Based on the continued good agreement with both the previously discussed comparisons, a system size of 500 atoms was selected for all results reported in this work. The following compositional mixtures were considered: R_σ of 1.0, 1.1, 1.25, 1.5 and 2.0; R_ε of 1.0, 1.25 and 1.5; and R_m of 1.0, 1.6, 2.1 and 3.3; at the following different relative concentrations of A and B atoms ranging 100% A atoms, 75% A with 25% B, 50% A with 50% B, and 25% A with 75% B.

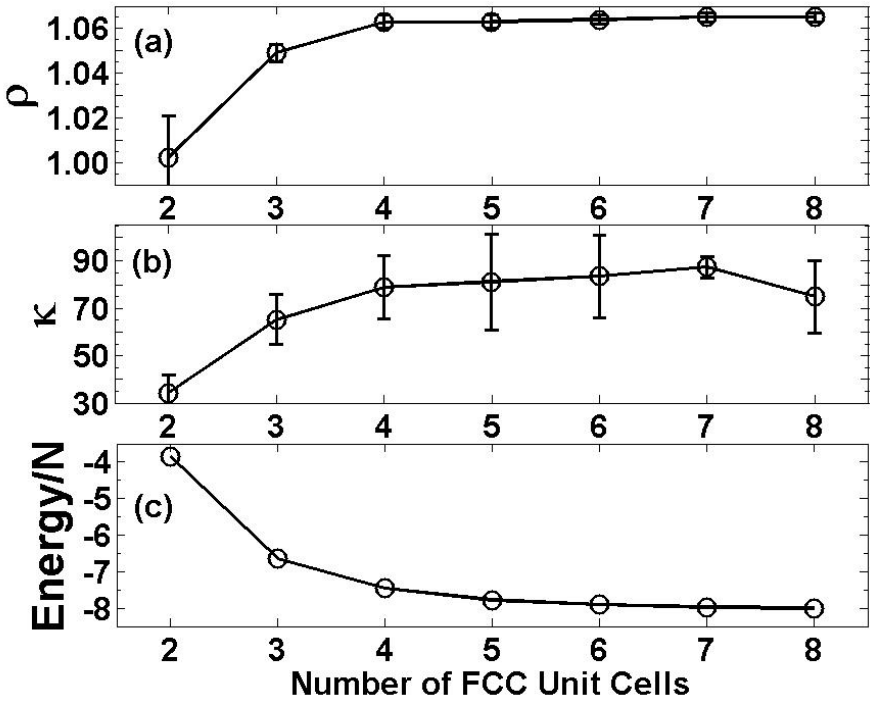

Figure 13: Finite size effects due to computational box size for Ar systems at T=0.167

For samples with relative concentrations of 50:50, at a temperature of T = 0.167, Figure 14 illustrates the lattice κ as a function of one parameter ratio (R_σ, R_ε, or R_m), while the other two parameter ratios are kept constant. Figure 14 (a) and (b) show a dramatic decrease of κ with increasing R_σ. In fact, Figure 14(a) shows that κ decreases by a factor of over 6 between $R_\sigma = 1$ and $R_\sigma = 1.1$ for a constant mass ratio and various values of R_ε. Likewise, Figure 14(b) shows a dramatic decrease in κ between $R_\sigma = 1$ and $R_\sigma = 1.1$ for different mass ratios. In this case again, κ decreases by factors up to 6 depending upon R_m. While Figure 14(b) shows a substantial decrease in κ between $R_\sigma = 1$ and $R_\sigma = 1.1$, the two atom types would have to be the same to have $R_\sigma = 1$ and $R_m = 1$,

which is an unrealistic case. On the contrary, Figure 14(c) shows that, for $R_\sigma = 1$ and $R_m = 1$, κ increases slightly as a function of R_ε and decreases as R_σ increases. This increase lies within the SDs of the κ results and might not be a real effect.

The conclusion of the parameter analysis is that at T= 0.167, both radius disorder and mass disorder impose a strong depletion of κ. Even a slight difference in atomic radius of only 10% has a major effect on decreasing κ, while the mass ratio has a more gradual depleting effect on κ. The mass disorder leaves the crystalline symmetry intact. In comparison, the radius disorder allows the solid to acquire incipient amorphous

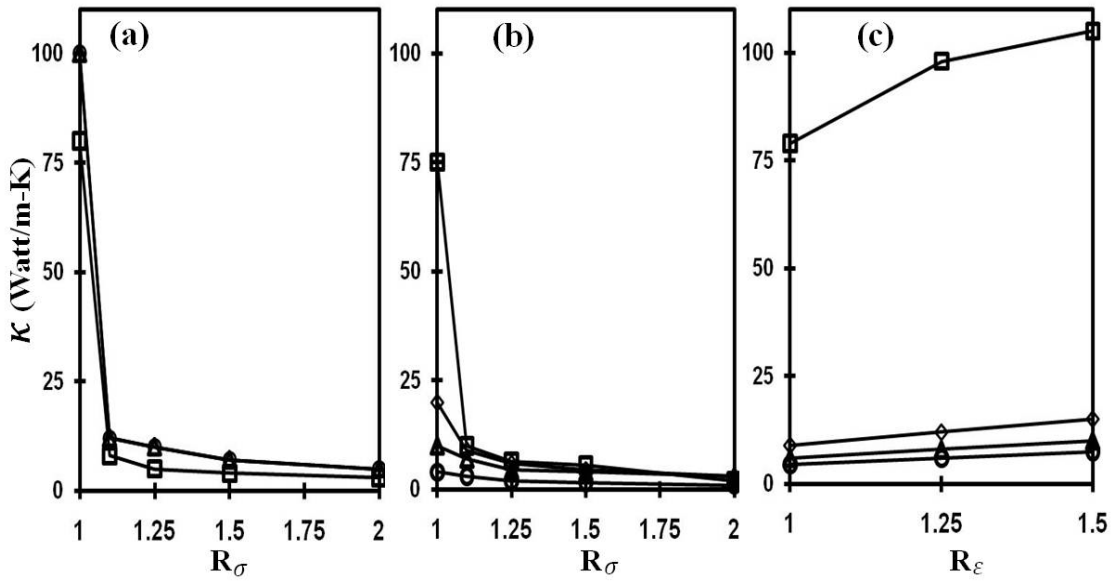

Figure 14: Thermal conductivity as a function of parameter ratios for a sample at T=0.167 and ρ=1.035; (a) $R_m = 1$, $R_\varepsilon = 1.0(\triangle), 1.25(\circ), 1.5\ (\square)$, (b) $R_\varepsilon = 1$, $R_m = 1.0(\ \square), 1.6(\Diamond), 2\ .1(\triangle), 3.3(\circ)$; and (c) $R_m = 1$, $R_\sigma = 1.0\ (\square), 1.1(\Diamond), 1.25(\triangle), 2.0(\circ)$

characteristics as evidenced by the pair correlation function signature illustrated in Figure 11. In fact, for the large difference in atomic radii of 25%, Figure 11 indicates that the FCC symmetry is already lost and the solid is no longer a crystal.

3.2.3 Temperature Effects on the Thermal Conductivity

For monatomic crystalline materials, the expected theoretical dependence of the thermal conductivity with temperature follows an inverse power law [6-7]. While previous MD simulations [28] reported κ exhibiting this expected behavior, the results show a departure for any of the proposed samples with disorder. Figure 15 shows the κ behavior for various values of R_ε of 1.0, 1.25 and 1.5 and $R_m = 1$ for a 50:50 concentration. In Figure 15 the inverse temperature dependence is plotted with a dotted line to guide the eye. Figure 15(a) depicts the temperature dependence for $R_\sigma = 1$ with the square, circle and triangle symbols identifying the three values of R_ε (1.0 (□), 1.25 (○), and 1.5 (Δ)), respectively. SDs are shown for the $R_\varepsilon = 1.25$ case and are representative of the other cases. Figure 15(b) gives results for systems with $R_\sigma = 1.1$ as solid lines corresponding to R_ε = 1.0, 1.25, and 1.5 (top, middle and bottom) and dashed lines for $R_\sigma = 1.25$. SDs are about 1–2 units of κ for all results. It is apparent from these plots that the ordered crystal with no core radius disorder follows the 1/T relationship very closely (Figure 15(a)), while any of the compositionally disordered systems (Figure 15(b)) present a nearly constant κ as a function of temperature. This degrading of the thermal conduction is similar to that predicted for covalent binary crystals with defects [38] where κ was found to be essentially temperature independent. In the study, it should be remembered

that compositional disorder in which the atomic radii differ by only 10% produces a dramatic reduction of κ to a minimum value, which keeps fairly constant for the temperatures investigated. In summary, it should be emphasized that the radii disorder has an extremely strong effect to reduce κ, bringing its value to be a minimum for all calculations with widely varying material parameters.

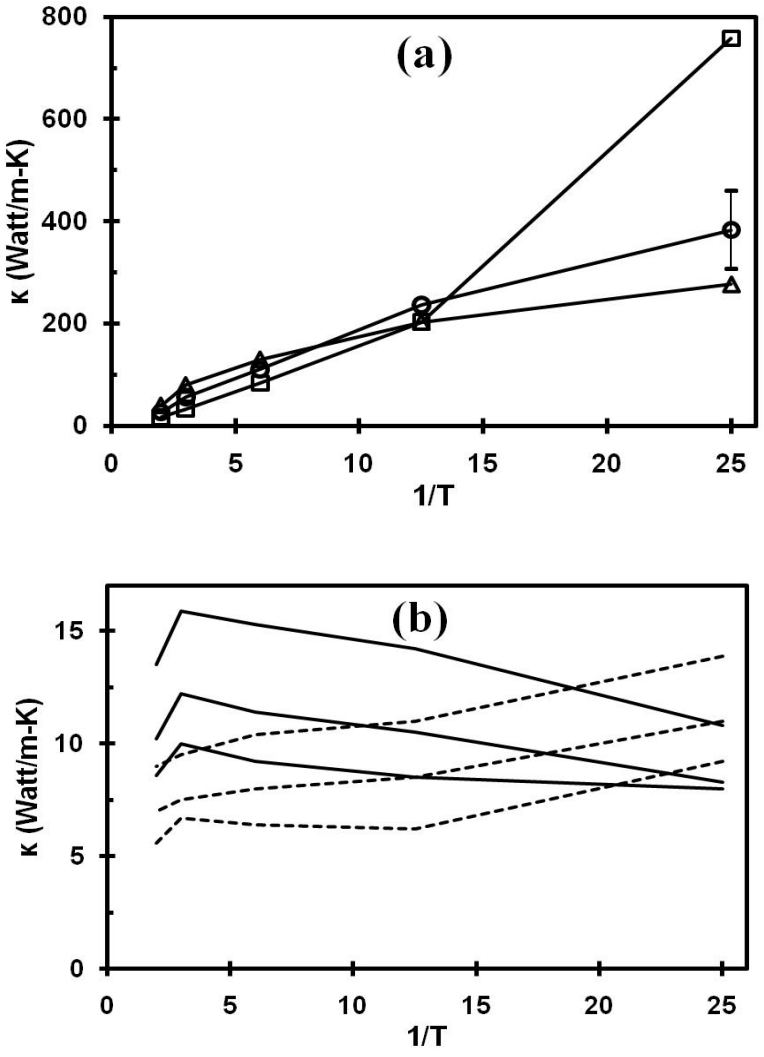

Figure 15: Thermal conductivity as a function of temperature for parameter ratios: (a) $R_\sigma = 1.0$, $R_\varepsilon = 1.0$ (□), 1.25(∘), 1.5(△) , and (b) $R_\sigma = 1.1$ (solid) $R_\sigma = 1.25$ for $R_\varepsilon = 1.0$ $(top), 1.25(middle), 1.5(bottom)$

3.2.4 Concentration Effects

The last part of this study pertains to changes in the relative concentrations of the A and B atoms. Relative concentrations of A:B atoms of 25:75 and 75:25 were analyzed in addition to the 100% type A and the 50:50 mixture cases discussed above. As the concentration changes, when the disorder is on the radii, there is a significant effect on the equilibrium density, ρ, as shown in Figure 16 for the case of a 50:50 mixture.

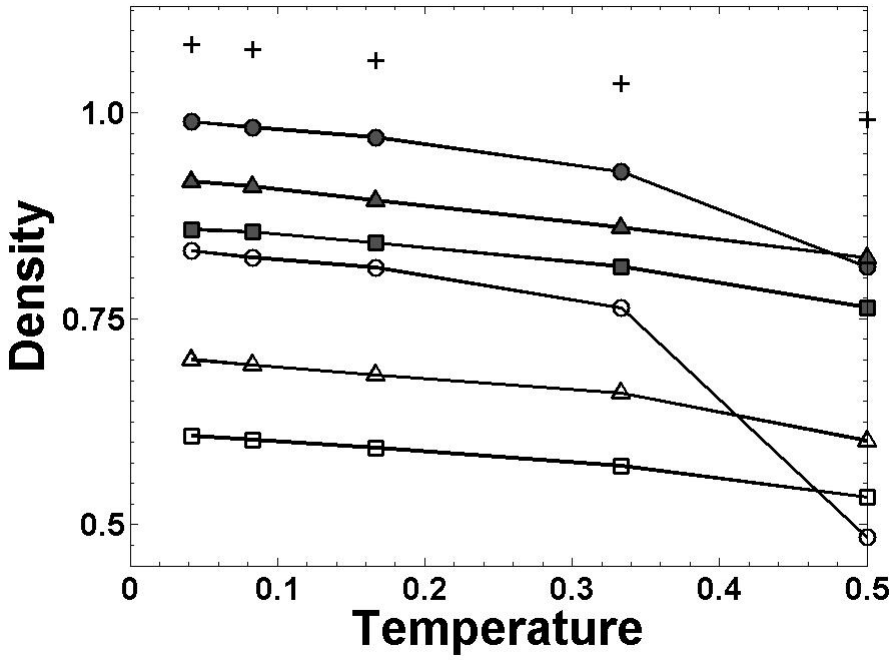

Figure 16: Density as a function of temperature for 50:50 relative concentrations in the mixture. Filled symbols for R_σ = 1.1 and open symbols for R_σ = 1.25. The circle, triangle and square are for R_ε = 1.0, 1.25 and 1.5, respectively. R_σ= R_ε = R_m =1 is shown as crosses.

In analyzing mixtures with the 25:75, 50:50 and 75:25 relative concentrations over the range of T, R_σ, R_ε and R_m, the behavior of κ was very similar to that of the 50:50 case. Table 3 summarizes all results of κ for the various disorder cases at five temperatures.

Once again, for these relative concentrations studied, the maximum decrease in κ is through R_σ.

Table 3: Lattice thermal conductivity for mixtures with various relative concentrations at temperatures 0.042, 0.083, 0.167, 0.333, and 0.5 in reduced units

Relative Concentration	**Temp**	$R_\sigma = 1$ $R_m = 1$ $R_\varepsilon = 1$	R_σ		R_ε		R_m		
			1.1	**1.25**	**1.25**	**1.5**	**1.6**	**2.1**	**3.3**
100% A	0.042	476.6							
	0.083	200.1							
	0.167	79.5							
	0.333	31.9							
	0.5	14.5							
75% A, 25% B	0.042		8.8	5.8	331.5	184.2	-	-	-
	0.083		9.5	7.1	201.1	138.8	-	-	-
	0.167		10.4	6.6	98.9	75.4	22.9	12.4	7.2
	0.333		10.6	6.0	37.4	35.8	-	-	-
	0.5		6.8	3.2	16.8	18.1	-	-	-
50% A, 50% B	0.042		8.3	9.1	329.4	230.1	-	-	-
	0.083		8.5	6.3	193.2	164.7	-	-	-
	0.167		8.4	6.0	98.4	113.1	18.9	9.4	4.8
	0.333		10.0	6.1	41.8	49.9	-	-	-
	0.5		7.6	5.5	23.5	26.2	-	-	-
25% A, 75% B	0.042		7.5	9.4	231.2	275.1	-	-	-
	0.083		9.0	6.2	331.8	199.6	-	-	-
	0.167		16.9	6.3	107.9	141.3	22.8	14.7	3.6
	0.333		11.2	5.8	55.3	79.1	-	-	-
	0.5		8.5	5.4	24.6	39.8	-	-	-

Additionally, as is shown in Figure 14(c) for the 50:50 relative concentrations, the effect of increasing R_ε while R_σ and R_m remain constant, produced an apparent slight increase in κ. This effect is also present for the other relative concentrations as reported in Table 4 at T = 0.042, 0.083, 0.167, 0.333 and 0.500 (top to bottom in each table entry). For any parameter ratio ≠ 1, the other two parameter ratios = 1. Values are in reduced units.

3.2.5 Compositional Disorder Effect on the Heat Current Autocorrelation Function Time

To compute the lattice thermal conductivity, the autocorrelation function of the heat current operator $C(\tau)$ was approximated by an exponentially decaying cosine function (see section 2.6.1). In Figure 17, the vertical axis on both plots depicts the system relaxation time and is plotted as a function of R_σ in Figure 17(a) and R_m in Figure 17(b). This figure clearly illustrated that the relaxation time is directly related to the core radius and mass disorder present in the sample. The change in relaxation time due to the R_ε disorder is small as evidenced by the three curves in Figure 17(a) and (b).

3.3 SUMMARY AND CONCLUSIONS

Throughout this phase of the research work, it has been shown that studying the effects of compositional disorder and temperature on the thermal conductivity of binary mixtures can be demonstrated in computer-simulated experiments. The work was performed on a personal computer with a single Pentium 4 processor (3.2 GHz) and each NPT MC and MD run consumed about 9 and 4 hr of processing time, respectively, per data point, making the work reasonable to accomplish.

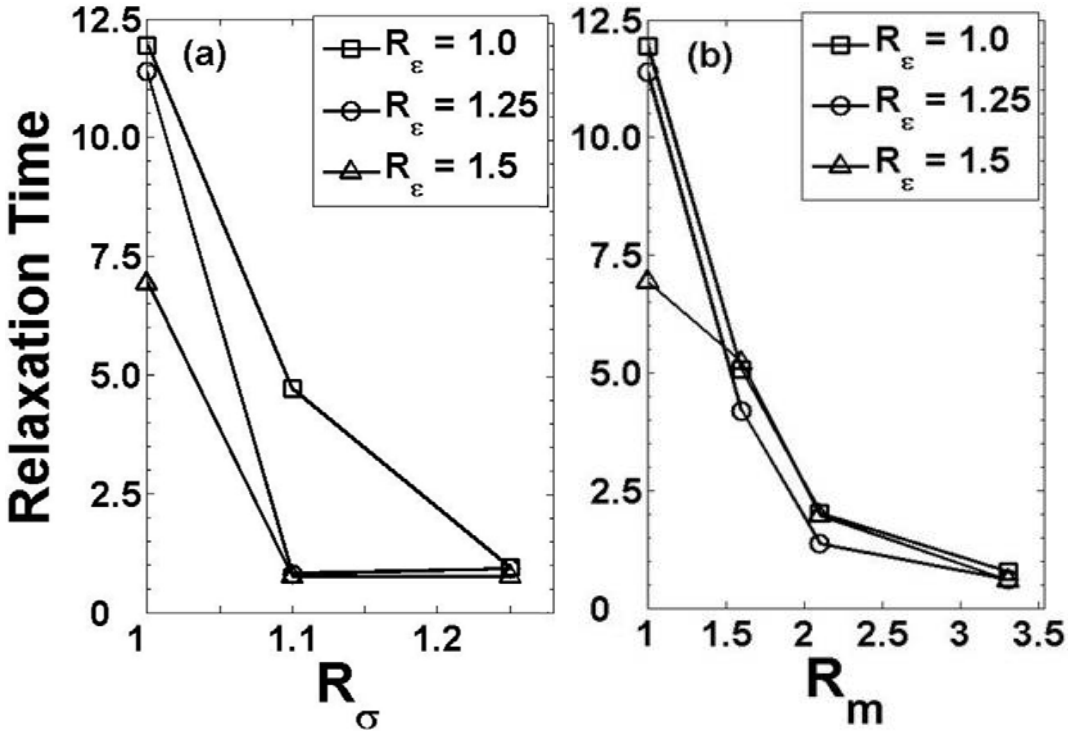

Figure 17: Relaxation time as a function of parameter ratios for the 50:50 sample for T=0.167, ρ=1.035, (a) $R_\varepsilon = 1.0\ (\square), 1.25(\circ), 1.5(\triangle)$, (b) on each plot.

The results of this work show that compositional disorder at the nanoscale in crystalline and amorphous binary mixtures decrease the lattice thermal conductivity in a dramatic fashion. Findings in this work are important for tailoring the synthesis of new materials with low heat conduction characteristics. The relative properties of LJ solid mixtures are summarized below in order of importance for degrading the lattice thermal conductivity:

(1) Core radius. Atoms should have different core radius. Even a 10% difference brings the lattice thermal conductivity to a minimum constant value and suppresses the inverse power law dependence with temperature. The reason for the dramatic degradation of the

heat conduction is the additional phonon scattering imposed at the nanoscale by atoms that are displaced from the crystal structure yielding an amorphous solid.

(2) Mass. Atoms should have different masses. Differences of 60% in mass decrease the thermal conductivity by about half at any temperature below the melting point.

(3) Interatomic interaction strength. Atoms should have almost equal values. With a 50% difference in strength, thermal conductivity can be increased up to 25%, which is not a desired outcome.

(4) Temperature. Temperature is a key factor for any application searching to deplete heat conduction due to atomic vibrations. This work was done for reduced temperatures of up to 0.5, which are below the melting points of the pure LJ crystals studied. In this temperature range, when core radius disorder exists, the lattice thermal conductivity is essentially temperature independent and markedly degraded due to the enhanced phonon scattering induced by atoms with different radii randomly located on an FCC crystal.

(5) Composition relative concentration. Relative concentration of the two components in the crystal appears to have only a minor effect on the thermal conductivity.

CHAPTER 4 DETERMINATION OF INTERFACE EFFECTS ON THERMAL CONDUCTIVITY

4.1 BACKGROUND

Large scale integrated circuitry, components, and sensors rely on internal solid-solid interfaces for controlling the operation of the device and on efficient thermal energy management for dissipating heat generated inside the device. Since the discovery of a thermal boundary resistance at cryogenic solid-liquid interfaces by Kapitza in 1938 [39], researchers have investigated the cause of the thermal resistance and quantify its magnitude as a function of material properties, temperature, and pressure. The thermal boundary resistance internal to a system is referred to as the Kapitza resistance (Ω_K).

In solids, the thermal boundary resistance plays an important role in determining heat flow, both in cryogenic and room-temperature applications. Two approaches have been used successfully in the past to model thermal transport at a solid-solid interface at low temperatures: the acoustic mismatch model (AMM) and the diffuse mismatch model (DMM) [40,41]. The AMM is more applicable at extremely low temperatures, while the DMM works better at slightly higher temperatures. However, at intermediate cryogenic temperatures and above, the experimental Ω_K is larger than that predicted by AMM and

DMM. At an interface, phonon scattering has a large effect on the heat transport across the interface, unfortunately the AMM and DMM do not take this into account.

Several researchers have studied with computational-theory approaches the boundary resistance at flat interfaces [42], diffuse scattering of the vibrational states at each side of the interface [41,43], structural ordering on each side of an interface [41-42,44-47], and effect of mass changes on each side of the interface on the eventual overlapping of vibrational states and energy transport [48,49]. NEMD techniques with LJ interactions has been applied to study thermal properties in non-homogeneous systems such as grain boundaries [1, 50-53] and for simulating the directional heat flow perpendicular to infinite thin films in one-, two-, or three-dimensional LJ systems [1,32,42-44,48-55]. Additionally, researchers have used NEMD to determine the Kapitza resistance at grain boundaries [42,43,53,54,56]. Other studies [43,53,54,57,58] have proposed that the Kapitza effect is due to reflection of the harmonic phonons at the interface or grain boundary, or to inelastic effects and anharmonicities. Additionally, a few researchers have investigated a silicon grain boundary simulated with the Stillinger-Weber potential [43,53], and a combination of two FCC lattices, one LJ and one Morse potential [54].

Reference [57] is a study of the thermal boundary resistance of a LJ system with geometry similar to the one presented in this paper; however, the acoustic mismatch model is used instead of exploiting directly the NEMD computer experiment results. The NEMD was used in [58] to study the temperature jump at a liquid-solid boundary. Based on these few studies, it is apparent that there is no general understanding of the Kapitza

resistance as a function of the atomic parameters entering in the modeling of the materials.

The research presented in this chapter addresses the effects of an interface on the atomic vibrations in LJ solids, without or with a heat current flowing through the solid sample. Selection of the type of materials could limit, encourage, or restrict the flow of thermal energy through a solid-solid interface. The study expands the work in [9] by focusing on the thermal boundary resistance occurring at the interface between two LJ solids as a function of the ratio of atomic parameters of these solids.

4.2 MODELING

4.2.1 Setup

MD simulations were performed using a square-prism computational box elongated along the X axis with periodic boundary conditions in the two perpendicular directions (Y and Z) (see 2.4.1 and Figure 2). The system contained 2000 atoms placed in an FCC lattice of size $5x5x20$ unit cells in a [100] orientation with a density of $\rho = 1.07$ at $T = 0.12$, and $\rho = 1.04$ at $T = 0.33$. The system was divided in half with reference atoms (type A) on the 'hot' (or positive X) side and atoms of either A or B type on the 'cold' side. Atoms were allowed to interact using the LJ potential with the parameters discussed in the previous chapter. Figure 18 is a schematic representation of the simulated interface.

When the core radius for type B atoms was different than the core radius of the type A atoms, the FCC lattice contained a different number of XY-planes and XZ-planes on each

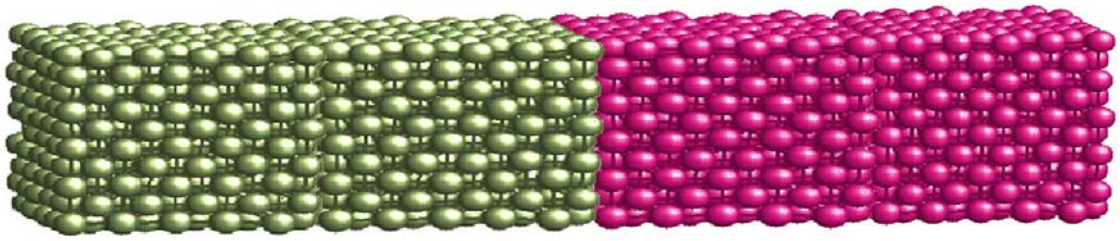

Figure 18: Schematic representation of the system used to simulate the interface between two LJ solids

side of the interface. This was done to permit the use of the PBC. The time step (in reduced time) in the MD runs was $\Delta t = 0.005$. A radial cutoff of 3.8 σ_A was adopted. The following values of the parameters ratios are considered: i) for parameter ε, R_ε = 1.0, 1.25, 1.5, and 2.0; ii) for parameter σ, R_σ = 1.0, 1.1, and 1.2; iii) for mass, R_m = 1.0, 1.6, 2.1, and 3.3.

To simulate a thermal current flowing from the hot to the cold ends, a non-equilibrium MD (NEMD) was used. At each end of the system, a thermal bath containing about 200 atoms was simulated as described in section 2.4.3. Atoms in each thermal bath move according to a constant temperature MD, with their velocities scaled at every time step to ensure the temperature desired for that bath. Atoms in between these two thermal bath regions move with iso-energy MD and data is collected only on these central atoms (typically 1600 atoms) (See Figure 3). When the NEMD runs were initiated, the system had to be run for enough time steps to reach a steady state condition. The steady state condition was known when the thermal energy current was constant along the length of the computational box in the direction of the energy flow. This NEMD arrangement has

been used by other authors in calculations of the lattice thermal conductivity [1,32,49-54,57,58].

Steady state data of all studied properties are averaged over each slice of approximately 100 atoms in equal sized regions perpendicular to the computational box length (see Figure 3). As a result of the different MD methods between the atoms in the thermostat and the atoms in the active central region where data are taken, a few planes of atoms adjacent to the thermal baths were not considered for reporting of results. A similar consideration was adopted by other researchers [1,32,51,53].

4.2.2 Model Validation

In the NEMD, a temperature gradient $\vec{\nabla}T$ sets in due to the flow of energy across the computational box. With this geometrical setup, the heat current components perpendicular to the energy flow should be negligible. Indeed, that is the case in the calculations. The temperature difference between the two thermal baths was chosen to be large with respect to the temperature fluctuations, but small enough to reproduce attainable laboratory situations. In these runs, the cold bath temperature was about 60% of the hot bath temperature. This choice is similar to the 65% - 70% employed in other works [1,51,55].

Figure 19 shows the thermal conductivity as a function of temperature for one-component systems with different values of the parameters ε, σ and mass. Six different masses and LJ parameters were considered: Figure 19a: R_ε= 0.7 (●), 0.8 (▲), 0.9 (■), 1.25 (□), 1.5

(Δ), 2.0 (○). Stars and standard deviations are from [9]. Solid diamonds pertain to the reference LJ system and dotted line (in a,b,c) is the best fit to these values. Crosses and standard deviation are from [9].); Figure 19b: R_σ= 0.7 (●), 0.8 (▲), 0.9 (■), 1.1 (□), 1.2 (Δ), 1.25 (○); Figure 19c: R_m= 0.3 (●), 0.5 (▲), 0.7 (■), 1.6 (□), 2.1 (Δ), 3.3 (○). In all cases, the dotted line corresponds to the reference system R_ε= R_σ= R_m =1. Standard deviations are shown on the figure; however, their values of about 3% to 7% of the average value are within the size of the symbols.

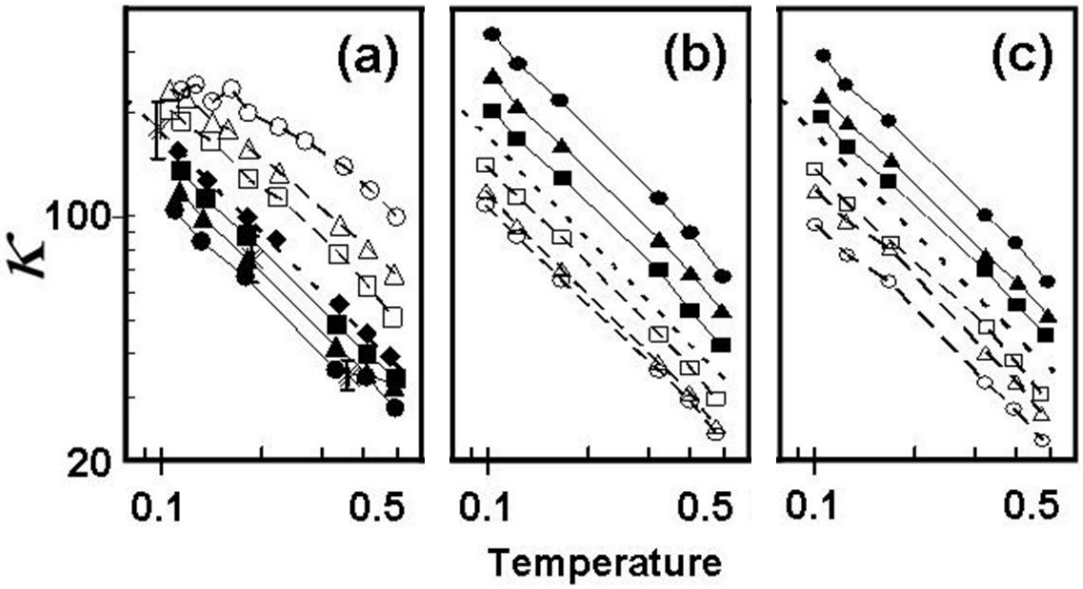

Figure 19: Thermal conductivity as a function of temperature. (a) R_ε= 0.7 (●), 0.8 (▲), 0.9 (■), 1.25 (□), 1.5 (Δ), 2.0 (○), Stars and standard deviations are from [9]. Solid diamonds pertain to the reference LJ system and dotted line (in a,b,c) is the best fit to these values. Crosses and standard deviation are from [9].); (b): R_σ= 0.7 (●), 0.8 (▲), 0.9 (■), 1.1 (□), 1.2 (Δ), 1.25 (○); (c) R_m= 0.3 (●), 0.5 (▲), 0.7 (■), 1.6 (□), 2.1 (Δ), 3.3 (○).

The parameter dependence of κ compares well with the previous work within the GK approach described in Chapter 3 and in [9]. The expected inverse temperature relationship for crystalline systems is clearly shown by the log-log plot of Figure 19 and can be used to interpolate between different LJ systems, as suggested by other authors for other potentials [42,43,53,54,57,58]. Based on the results, such interpolation yields a power law relationship for each varied parameter (σ, ε, and mass): R_{σ}^{-2}, $R_{\varepsilon}^{3/2}$, and $R_{m}^{-1/2}$.

4.2.3 Effect of the elongated computational box on the lattice vibrations

The velocity autocorrelation function for N atoms defined in equation (29) (section 2.6.3) is calculated better after normalization, such that:

$$C_{vel}(t) = \frac{\sum_{i=1}^{N}(\overrightarrow{v_i}(t)*\overrightarrow{v_i}(0))}{\sum_{i=1}^{N}(\overrightarrow{v_i}(0)*\overrightarrow{v_i}(0))} \tag{34}$$

where $\overrightarrow{v_i}$ are the atom velocities and t is a time lag. Typically $500{,}000\ \Delta t$ time steps were required to reach equilibrium followed by $20{,}000\Delta t$ for data collection. The data was subdivided into short sequential time segments and then an autocorrelation function was performed on each segment. The final $C_{vel}(t)$ is then an average over several functions. A Fourier transform was made of the result according to equation (30) and the density of vibrational states (DOS) was obtained for prismatic computational boxes. The resulting DOS compared very well with published results in which the computational box was cubic [59,60]. Therefore, it was concluded that an elongated shape of the computational box does not affect significantly the distribution of vibrational frequencies.

4.3 EFFECTS ON THERMAL CONDUCTIVITY

4.3.1 Vibrational Modes of Monatomic Systems

A sample was established using the computational box shown in Figure 18 for LJ atoms with $R_\sigma = R_\varepsilon = R_m = 1.0$, ρ = 1.07 at T = 0.12, and also at ρ = 1.04, T = 0.33. This was referred to as the reference system. MD runs were made allowing the system to reach thermal equilibrium first, then the vibrational mode DOS was determined. In subsequent runs, all atoms in the system were changed to have a different LJ parameter and the DOS was determined for each monatomic system. Each of the DOS obtained was normalized over the entire frequency spectrum and are shown in Figure 20. Figure 20 shows the DOS for each LJ parameter for each of the two temperatures. Figure 20 a-c are for T = 0.12 and Figures 20 d-f are for T = 0.33. In each plot, the solid line is the reference system. Figure 20 a and d show the DOS for R_ε = 1.25 (●), 1.5 (□), and 2.0 (Δ) with $R_\sigma = R_m$= 1. Figure 20 b and e show the DOS for R_σ = 1.1 (●) and 1.2 (□) with and $R_\varepsilon = R_m$ = 1. Figure 20 c and f show the DOS for R_m = 1.6 (●), 2.1 (□), and 3.3 (Δ) with $R_\varepsilon = R_\sigma$ = 1.

It can be seen that there is a strong difference between the DOS for the reference system and the DOS for monatomic systems with different atomic parameters. It is to be noted that the DOS is shifted towards smaller frequencies as the mass is increased. On the other hand, increases in ε, and to a lesser extent σ, with respect to the reference system, tend to add high frequency vibrational modes to the DOS.

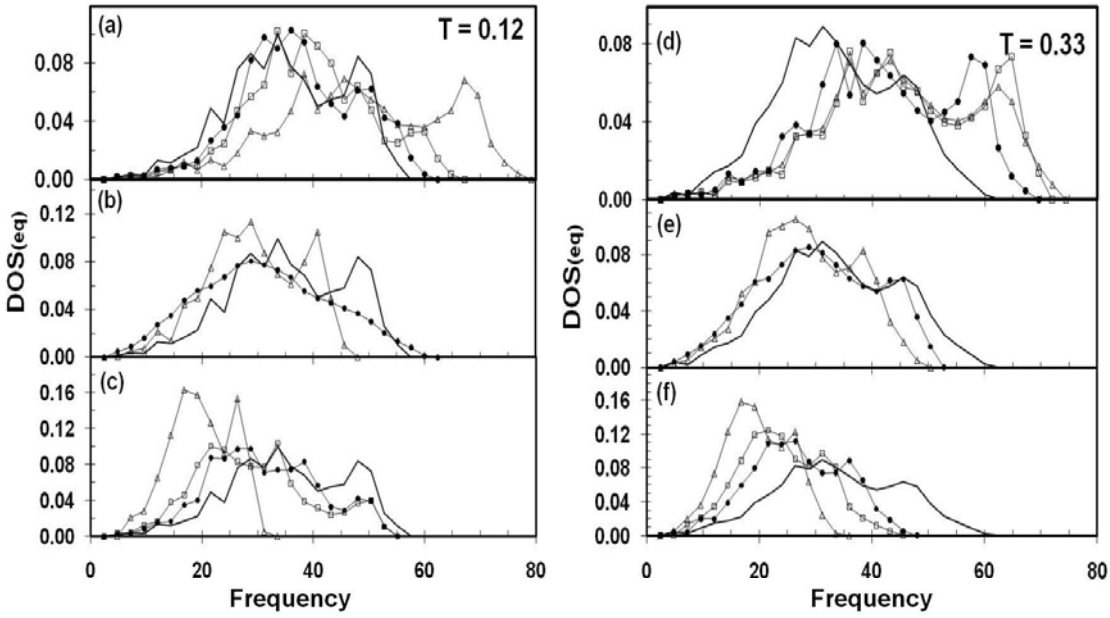

Figure 20: Normalized density of states (DOS) of one-component systems in thermal equilibrium for various LJ parameters. (a-c) are for T = 0.12 and (d-f) are for T = 0.33. The solid line is for $R_\varepsilon = R_\sigma = R_m = 1$ in all plots. In (a) and (d) the DOS for R_ε = 1.25 (●), 1.5 (□), and 2.0 (Δ) with $R_\sigma = R_m$= 1. In (b) and (e) the DOS for R_σ = 1.1 (●) and 1.2 (□) with and $R_\varepsilon = R_m$ = 1. In (c) and (f) show the DOS for R_m = 1.6 (●), 2.1 (□), and 3.3 (Δ) with $R_\varepsilon = R_\sigma$ = 1.

4.3.2 Vibrational Modes of Binary Systems across the Interface of Two LJ Systems in Equilibrium

It is known that any disorder or change in a material property will affect the ability of a material to transport heat, especially that of an interface. It was unknown as to how the vibrational modes of a system would change with the presence of an interface. To study this, a sample was established with reference (type A) atoms on the 'hot' end and atoms with one of the three studied LJ parameters changed (type B) on the 'cold' end. NEMD runs were made using the method described in the previous section to determine the

vibrational mode DOS for ρ = 1.07 at T = 0.12, and also with ρ = 1.04 at T = 0.33. Subsequent runs were made varying the type B through the range of values previously studied. Figure 21 shows the difference between the reference system of $R_\varepsilon = R_\sigma = R_m = 1$ which is shown as the solid line on Figure 20 and the DOS obtained for each two-component system at each of the two temperatures.

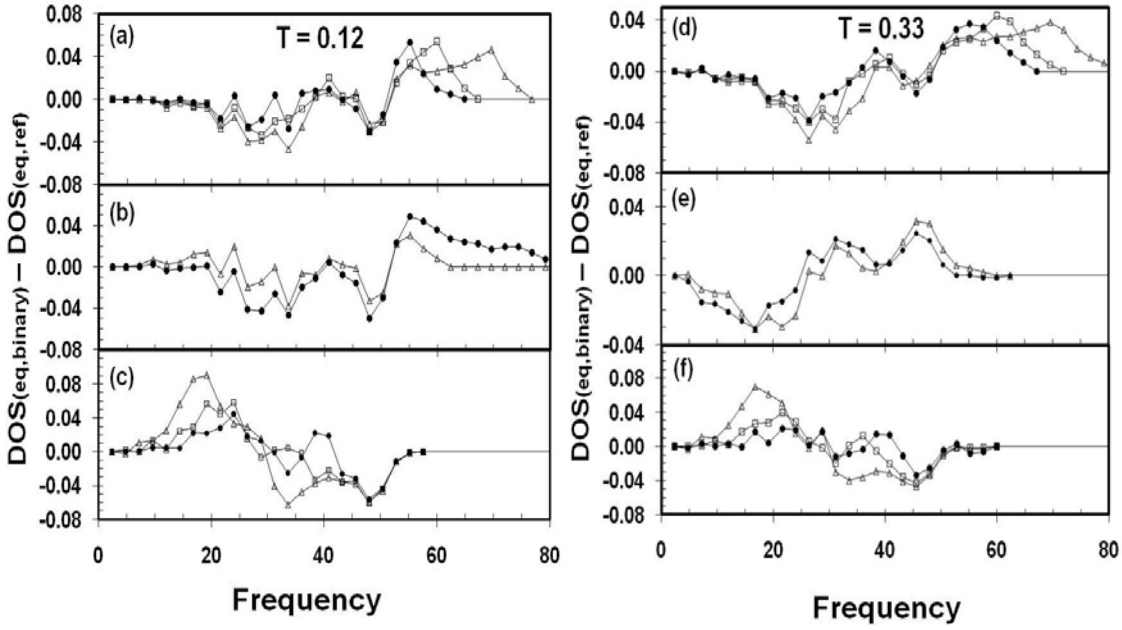

Figure 21: Normalized density of states (DOS) of binary systems in thermal equilibrium relative to the DOS of the one-component reference system for various LJ parameters. (a-c) are for T = 0.12 and (d-f) are for T = 0.33. In (a) and (d) the DOS for R_ε = 1.25 (●), 1.5 (□), and 2.0 (Δ) with $R_\sigma = R_m$= 1. In (b) and (e) the DOS for R_σ = 1.1 (●) and 1.2 (□) with and $R_\varepsilon = R_m$ = 1. In (c) and (f) show the DOS for R_m = 1.6 (●), 2.1 (□), and 3.3 (Δ) with $R_\varepsilon = R_\sigma$ = 1.

For interfaces due to changes in ε_B, Figure 21 a and d show an increase in the DOS of vibrational modes at high frequencies (60-80) and a decrease at lower frequencies around

20-40, both of which persist at T = 0.33. The effect is about the same for all R_ε values. Interfaces due to different σ_B shown in Figure 21 b and e display DOS changes similar to the changes in ε_B, but now in different frequency regions. On the other hand, as shown in Figure 21 c and f, the effect of mass changes produce a depletion of modes in the DOS in the range $30 \leq \omega \leq 50$ and an increase of mode density in the lower frequency region $10 \leq \omega \leq 30$. The mass effect is more acute the larger R_m becomes, in agreement with previous findings [49]. In all cases, the effect of the interface is identified by DOS changes above and below a characteristic frequency of $\omega_c \cong 30$.

4.3.3 Vibrational Mode Changes between Equilibrium and non-Equilibrium Systems with a Boundary Interface

It was investigated as to whether the presence of a heat current affects the vibrational mode DOS. To study this, the reference system was again composed of only reference atoms with $R_\sigma = R_\varepsilon = R_m = 1.0$, with ρ = 1.07 at T = 0.12, and also with ρ = 1.04 at T = 0.33. For each temperature, one run of the system with an interface was done in equilibrium and its DOS was collected. A second run of the same system was done with NEMD, such that an imposed thermal gradient is established across the system. After the systems were allowed to reach either equilibrium or a steady state, data was collected, and the normalized vibrational mode DOS was calculated. The two results are shown on Figure 22.

Figure 22 clearly shows that at the higher temperature, the DOS displays marginal changes when the system is in NE. However, at the lower temperature, the DOS of the NE system is slightly enhanced around $\omega = 30$.

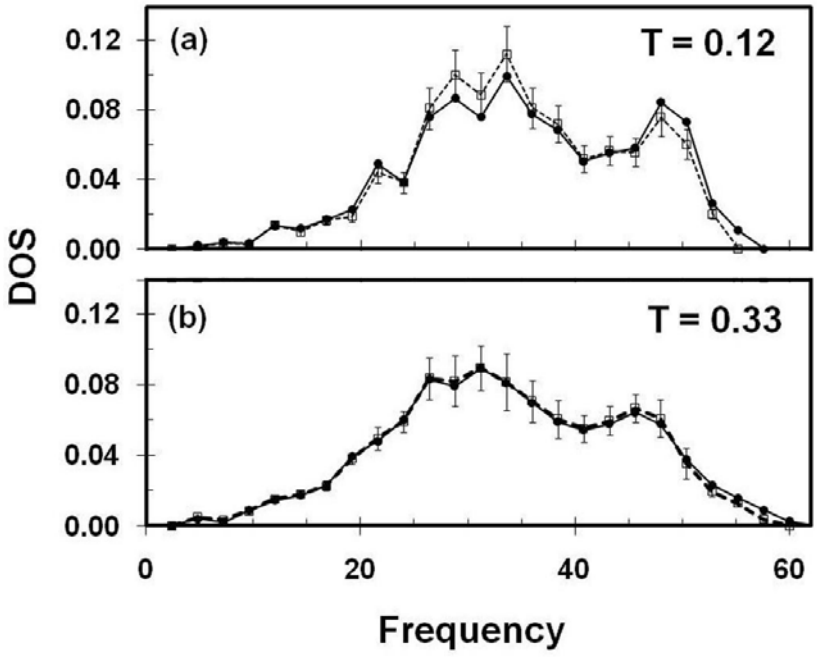

Figure 22: Normalized vibrational modes DOS for non-equilibrium (dashed line) and equilibrium (solid line) monatomic system at (a) ρ = 1.07, T = 0.12, and (b) ρ = 1.04, T = 0.33. Error bars identify the average SD of the correlation functions.

The work was continued to investigate how the normalized vibrational mode DOS changes for the two-component system with a boundary in Figure 18, and when a thermal current is imposed with thermal baths. Figure 23 shows the differences between the normalized NE DOS and the equilibrium DOS. Figure 23 a-c are for T = 0.12 and Figure 23s d-f are for T = 0.33. Figure 23s a and d show the DOS for R_ε = 1.25 (●), 1.5 (□), and

2.0 (Δ) with $R_\sigma = R_m = 1$. Figure 23 b and e show the DOS for $R_\sigma = 1.1$ (●) and 1.2 (□) with $R_\varepsilon = R_m = 1$. Figure 23 c and f show the DOS for $R_m = 1.6$ (●), 2.1 (□), and 3.3 (Δ) with $R_\varepsilon = R_\sigma = 1$.

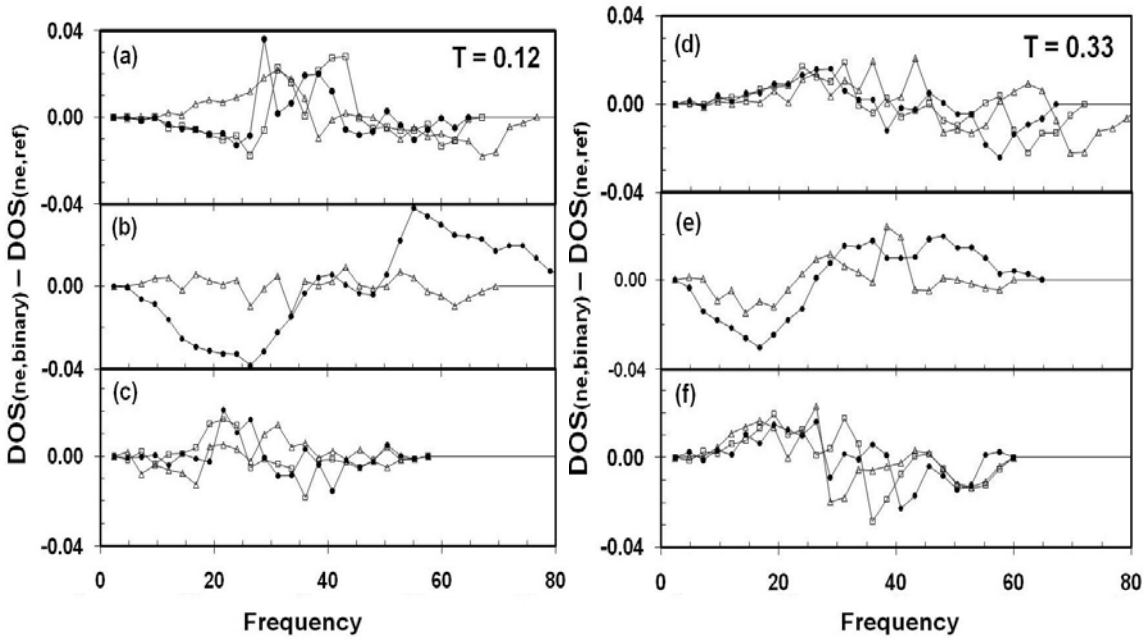

Figure 23: Non-equilibrium DOS of binary systems relative to their DOS in thermal equilibrium for various LJ parameters. (a-c) are for T = 0.12 and (d-f) are for T = 0.33. In (a) and (d) the DOS for $R_\varepsilon = 1.25$ (●), 1.5 (□), and 2.0 (Δ) with $R_\sigma = R_m = 1$. In (b) and (e) the DOS for $R_\sigma = 1.1$ (●) and 1.2 (□) with $R_\varepsilon = R_m = 1$. In (c) and (f) show the DOS for $R_m = 1.6$ (●), 2.1 (□), and 3.3 (Δ) with $R_\varepsilon = R_\sigma = 1$.

In systems with ε and mass changes and at T = 0.12, there is a modest increase of the DOS at frequencies around 30 and a small decrease around 50-60 due to the heat flow. At T = 0.33, the DOS is enhanced in a broader range at the low frequencies and depleted at higher frequencies for all binary systems involving atoms with two values of the

parameter ε or the mass. However, two-component systems with different σ (Figure 23b) display an enhancement of the NE DOS at higher frequencies and depletion at low frequencies. This effect tends to disappear at higher temperatures.

Summarizing, at T = 0.12, the overall effect of a 2-atom type interface in equilibrium is to modestly enhance the DOS at frequencies above ω_c, and deplete it below this characteristic frequency for R_ε, $R_\sigma > 1$, whereas, the opposite behavior is demonstrated for $R_m > 1$. When these two-component systems are not in thermal equilibrium, at T = 0.12, the trend is an enhancement of the DOS below the ω_c region for systems with different ε or mass. This is indicative that the heat flow enhances scattering of the transverse frequency phonons. These trends are smeared out at a higher temperature. On the other hand, interfaces built with atoms that have different σ values display a reverse behavior where the DOS is depleted of modes at frequencies below ω_c and enhanced above it.

4.4 INTERFACE EFFECTS ON THERMAL CONDUCTIVITY

4.4.1 Thermal Boundary Resistance

It is well known that solid-solid and liquid-solid interfaces act as a resistance to the heat flow perpendicular to them and give rise to the Kapitza resistance (Ω_K). This effect is measurable because of the discontinuity in the temperature profile occurring at the interface. Such temperature discontinuity is quite distinct across an interface built with two types of atoms and is detectable even for 1-D systems where atoms are linked

harmonically [42]. The calculation focuses on Ω_K of binary LJ solid-solid interfaces as a function of ε, σ and atomic mass. Figure 24 shows a typical temperature profile at T = 0.3 (R_m = 3.3, $R_\varepsilon = R_\sigma$ = 1 with ρ = 1.04) where the temperature discontinuity at the interface $\Delta T_{interface}$ is clearly seen. The Kapitza length (discussed in the following section) is shown on Figure 24 as well.

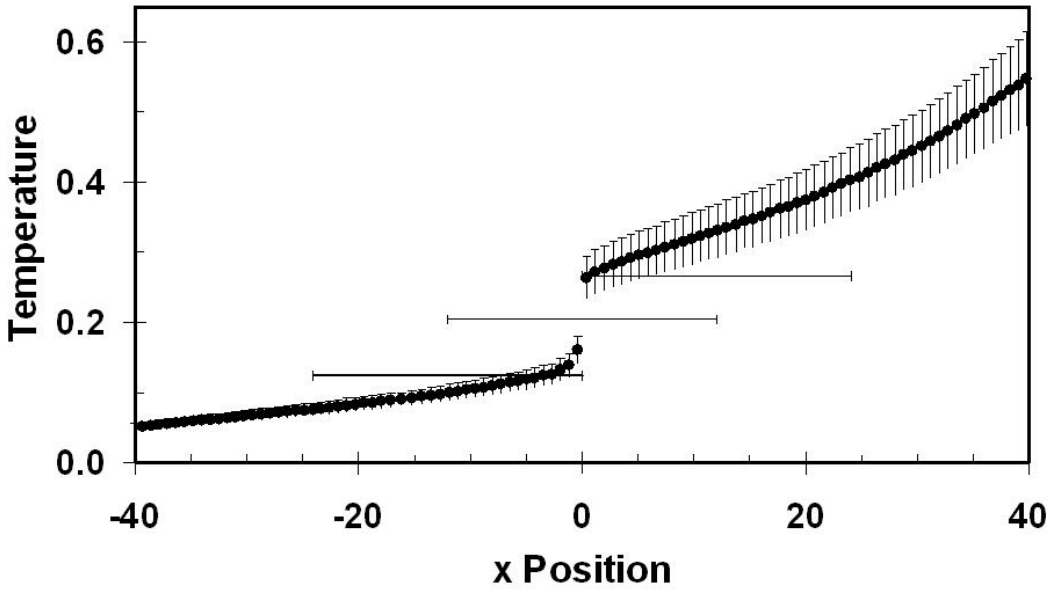

Figure 24: Temperature profile of the LJ system across the interface at T = 0.3 with R_m = 3.3, $R_\varepsilon = R_\sigma$ = 1 and ρ = 1.04. Horizontal lines show the Kapitza length calculated for hot side, interface, and cold side (top, middle, bottom), respectively). Temperature standard deviation is shown as vertical error bars.

The thermal resistance, Ω_K, is calculated as [53]:

$$\frac{1}{\Omega_K} = \kappa_0 \frac{\nabla T}{\mathrm{T_{interface}}} \tag{35}$$

where κ_0 is the bulk thermal conductivity. However, since it is known the κ at each side of the solid-solid interface, the atomistic approach for calculating Ω_K is to use the actual κ and ∇T values for the LJ crystal at each side of the interface. In fact, a thermal current sees the interface as two resistances in series because the heat current must be the same at both sides of the interface if no additional energy sources or sinks exist. It follows that:

$$\Omega_K = \Delta T_{interface} \left(\frac{1}{\kappa_A \nabla T_A} + \frac{1}{\kappa_B \nabla T_B} \right) \tag{36}$$

where $\kappa_{A,B}$ and $\nabla T_{A,B}$ are the thermal conductivity and temperature gradient of the LJ systems A and B that meet at the interface. Figure 25 shows the dependence of the temperature jump $\Delta T_{interface}$ at the interface as a ratio to the average temperature at the interface and the resulting Ω_K of the two-component systems for various temperatures and parameter ratios.

It is observed that as the parameter ratio moves away from the 1:1 ratio (no interface) the temperature discontinuity and the Ω_K become more pronounced. Runs were made to compare the thermal resistance for each of the three parameter ratios. Temperate drops are plotted relative to the temperature difference between the hot and cold thermal baths. Additionally, as the average temperature in the system is increased, the interface temperature discontinuity and the Kapitza resistance are less pronounced. It can also be seen that the Ω_K increases at about the same rate with changes of R_ε, R_σ,and R_m. In general, the building up of this thermal resistance is assigned to an increased reflectance of phonons by the interface [41,57].

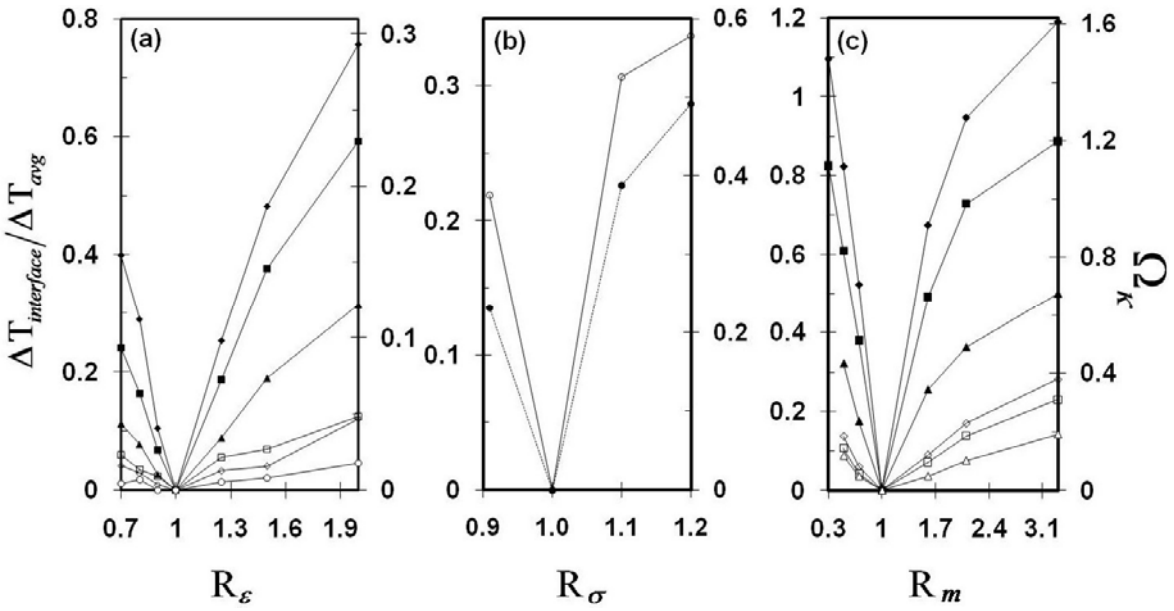

Figure 25: Temperature drop ratio at the interface (left scale) and Kapitza resistance (right scale) as a function system parameters at various temperatures of : 0.10 (♦), 0.125 (■), 0.165 (▲), 0.33 (□), 0.425 (◊), and 0.5 (○).

As discussed above, the equilibrium MD simulation shows that the interface increases the DOS of vibrational states in the region of high frequencies for two-component systems with different ε or σ, but for systems with different masses the increase occurs at lower frequencies. Based on these results, it immediately follows that two-component systems with different ε or σ should display larger Ω_K than the case with different masses at the same temperature. Illustrated in Figure 25 is a confirmation of this result. However, in the non-equilibrium situation, when the system reaches the steady state, the DOS of vibrational states is significantly populated in the region of ω_c. For systems with different ε and mass, as shown in Figure 25, is based on this result. It is then expected that the $\Delta T_{interface}$ for two-component systems with different ε and mass would be larger

than for systems with different σ as is shown in Figure 25. Increasing the temperature should reduce the Kapitza resistance and the temperature jump at the interface should be decreased. The results confirm both effects.

4.4.2 Interface Width

An additional characteristic quantity of interfaces is the Kapitza length

$$l_\kappa = \kappa \Omega_K \tag{37}$$

associated to the effective thickness of material involved in the interface [39,58]. It has been theorized [58] that when κ is large, l_κ will be large and the effect may be observed, but no data were provided for supporting the analysis. In the example of Figure 24, values of κ and Ω_K are 32 and 0.3, respectively, yielding a l_κ of about 9. This example was studied for several lengths of the computational prism to determine their eventual effect on l_κ. The Ω_K calculated for prism-shape computational boxes with lengths of 42.3, 73.7, 105, and 136.4, were all within the standard deviation of 11.4%, indicating that this property is basically insensitive to the length of the computational prism and the temperature jump at the interface is observed in all cases. From the results summarized in Figure 23 and Figure 25, it is predicted that l_κ varies as $1/T^2$.

4.4.3 Crystal Orientation at the Interface

The effect on κ and Ω_K, due to changes in the orientation of the crystals on each side of the interface, was also studied. First, it was determined that one-component systems did

not give rise to a discontinuity in the temperature at the interface when the interface was created by rotating atoms in the 'cold' half of the box to Miller Indices [110], [111], [120], [121], [122], while keeping atoms in the reference (or 'hot') half of the box at [100]. Second, the κ for these rotated systems is within the standard deviation of values reported in Figure 23. Third, in the case of two-component systems in which the A system is in the [100] orientation and the B system is rotated and its parameters change, the results for the temperature jump and the Ω_K are within 3% to 9% of values reported in Figure 25. Based on these calculations, it is concluded that the relative orientation of the crystal planes meeting at the interface do not affect the thermal properties.

4.5 INTERFACE BOUNDARY EFFECTS ON THERMAL CONDUCTIVITY CONCLUSIONS

In this work it has been quantitatively demonstrated that the influence of the interface between two LJ solid systems on the density of vibrational states as a function of the atomic mass and LJ parameters. A characteristic frequency of $\omega_c = 30$ (in reduced units) is predicted below which the DOS is depleted and enhanced above it for R_ε, and $R_\sigma > 1$, while the opposite behavior is demonstrated for R_m> 1. However, when a thermal energy flow is established, the DOS is enhanced below, ω_c and depleted above it for the cases R_ε, and $R_m > 1$. This is indicative that the heat flow enhances scattering of the transverse frequency phonons only in these two cases. At higher temperatures, these effects are less visible.

The NEMD computer experiment of two-component LJ systems sharing an interface leads to very clear observations that allow for identification of the thermal boundary resistance and its dependence on the LJ parameters and atomic mass. Both the Kapitza resistance and the temperature discontinuity at the interface increase as the parameter ratio between properties of the targeted material to the reference material moves away from the value of one. Additionally, both the Kapitza resistance and the interface temperature discontinuity increase with decreasing temperature. It is predicted that the Kapitza length increases as $1/T^2$ as temperature is decreased and is independent of the size of the computational box. The relationships contained in this dissertation and reference [10] may serve as reference for scientists and engineers in search of novel combination of materials in problems related to thermal management at the nanoscale.

The interface is responsible for a depletion of modes at low frequency and an enhancement at higher frequencies when the potential parameters are increased relative to the reference solid. Opposite trends are observed when the atomic mass increases. When a heat current is established across the interface, the density of vibrational states at low frequency is increased and the temperature profile across the binary sample displays a discontinuity at the interface, which is more pronounced as the material parameters become more dissimilar. The thermal boundary resistance (Kapitza resistance) increases as the difference between the two material properties increase and decrease with increasing temperature. Plots of the thermal conductivity as a function of temperature for solids with various parameters are provided, all of them showing the expected T^{-1} behavior. All of the calculations of κ_{ph} will be done at near room temperature (300 K).

CHAPTER 5 DETERMINATION OF THERMAL CONDUCTIVITY IN NANOWIRES, NANOTUBES, AND NANOFILAMENTS

5.1 BACKGROUND

Nanostructures began to emerge in the mid-1980s as building blocks useful to assemble larger materials and design special macromolecular constructs with novel mechanical and thermal characteristics. Today, nanodevices are fundamental for achieving improved mechanical, thermal, and electronic controls. Among other properties, the thermal conductivity of the device may be critical to control functioning and the stability of the macro-system to perform efficiently [61]. One postulated application of nanodevices is to act as heat conduits/sinks or refrigeration units for computer circuitry [62]. An important question is to whether these nanodevices are good or bad heat conductors and at the same time they remain stable at operational temperatures. Silicon carbide (SiC) is a broadly used material in nanoelectronics and has proven to sustain a variety of stable nanostructures. SiC nanotubes and nanowires have been fabricated experimentally, and a multitude of hollow fullerine-like clusters have been predicted which could be useful in building nanodevices [20,63].

Carbon and silicon are both group IVA elements on the periodic table and as a result can exhibit either sp^2 or sp^3 bonds [19]. These bonds cause bulk SiC to be among the hardest materials and is very well suited for electronic devices being operated in extreme environments [21]. In fact, bulk SiC has a wide band gap, high thermal conductivity, and is even resistant to various forms of radiation. It has been postulated that the use of SiC in nanostructures and nanodevices should exhibit these same properties. Although experimental advances are seen every day, it is still difficult to perform measurements of thermal properties at the nanoscale. Therefore, the uses of computational simulations of thermal properties are useful for adding understanding of the mechanisms in nanosystems. A number of non-equilibrium molecular dynamics (NEMD) studies for the determination of thermal properties in non-homogeneous systems have been published [1,10,50-52]. For example, NEMD was used for obtaining the lattice thermal conductivity by simulating the directional heat flow perpendicular to infinite thin films in one-, two-, or three-dimensional Lennard-Jones (LJ) systems [1,10,33,42-44,48-53,55]. However, little has been investigated for SiC nanostructures other than tensile strain simulations using a Brenner-Tersoff potential [47,64-66] and tight binding approaches concerning their energetic stability [19,20].

5.2 MODELING

5.2.1 Setup

Simulations were performed on SiC tubes, elongated filaments, and wires laid along the X-axis. The initial configurations of nanowires were obtained from cuts of the 3C and 2H crystalline polytypes. For nanotubes, initial configurations with either armchair or zigzag chirality were considered. The alternation of Si and C atoms was such that bonds of around 1.9 Å [8,19-21] are the dominant majority. Please note that real units were used in this phase of the research.

The simulations for nanostructures used the silicon carbide model potential described in Section 2.2.2. No periodic boundary conditions were used. A simulated thermostat was attached at each end of the nanostructure as a continuation of that structure. Each thermostat contained 100-150 atoms that were kept at a constant temperature. The thermostats were sized such that their width along the X-axis would be greater than 7.3Å, which is the cutoff distance of the 2-body part of the model potential. On the outside ends of the bath three-to-four planes of atoms were kept fixed in position to prevent deformations of the cross sections of the nanostructures. Atoms in-between the two thermal bath regions move with iso-energy MD and data are collected only on these central atoms (typically 320-384 atoms). Figure 26 depicts this setup.

When a temperature drop exists between the two thermal baths, a thermal energy flow is established along the elongated tube or wire and the system is neither in thermal

equilibrium nor in a steady state. However, after about 200 ps the system reaches the steady state and the thermal energy current is roughly constant along the length of the

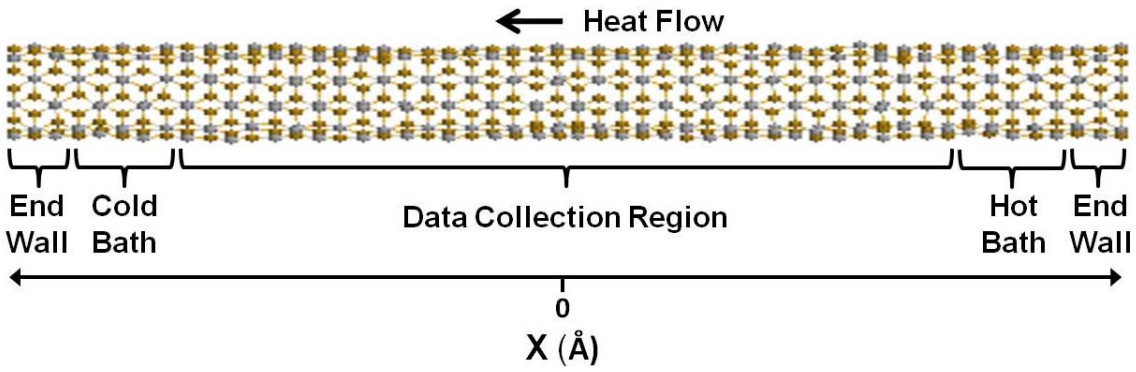

Figure 26: Nanotube computational setup

nanostructure. This NEMD arrangement is similar to that used in calculations of the lattice thermal conductivity [1,10,32,48-52,54,57,58,65,67]. The temperature difference between the two thermal baths was chosen to be large with respect to the temperature fluctuations but small enough to reproduce attainable laboratory situations. In the simulations, the cold bath temperature was about 40% of the hot bath temperature, which is less than the 60% cold:hot temperature ratio used in Chapter 4. This choice is similar to that employed in other works [1,10,50,55].

For the non-equilibrium analysis, the data section of each nanostructure, was subdivided in eight slices along its length as shown in Figure 4. Each slice contains typically 40- to 48-atoms. The purpose of this set up is to be able to average properties locally in each slice. Simulations were started for the equilibrated configuration of all systems. Once

the steady state of thermal energy conduction is reached, then the thermal current is the same in all slices, and the temperature profile is remarkably constant. Figure 27 shows both temperature profile and thermal current across a 3C nanowire. Nanotube and nanofilaments thermal profiles were similar.

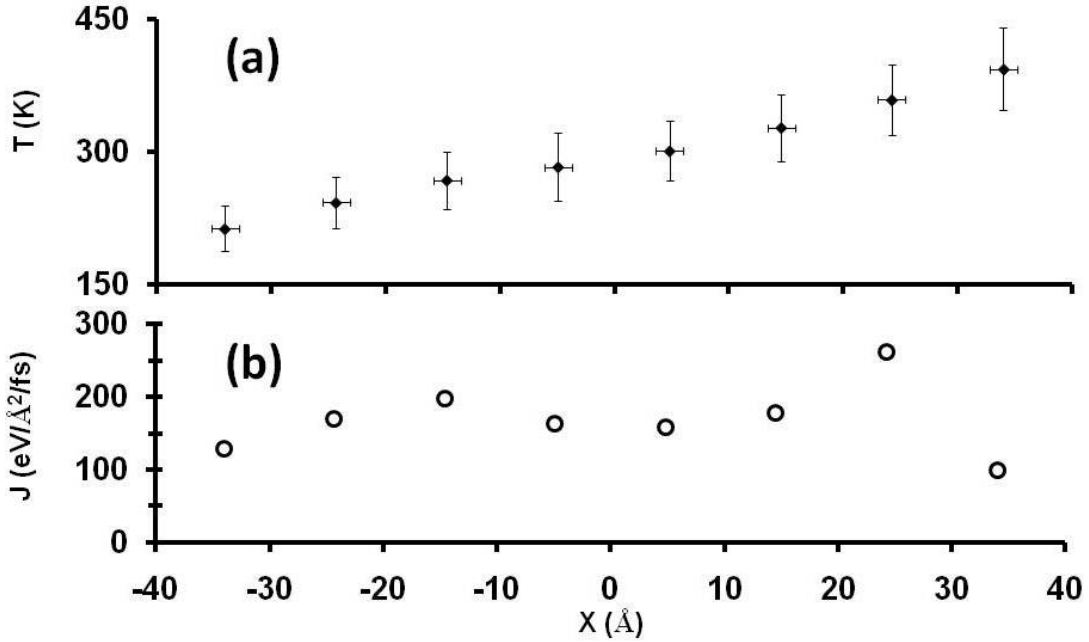

Figure 27: Temperature and heat current profile across a nanowire in the steady state at 300K: (a) temperature profile (♦) with SD for temperature and position, (b) heat current profile (○)

Points in Figure 27 correspond to averages for each slice over 6 psec after the steady state is reached. As a result of the different dynamics between the atoms in the thermostat and the atoms in the active central region where data are taken, a few planes of atoms adjacent to the thermal baths were not considered for reporting of results in the sections

to follow. A similar consideration has been adopted in the literature by several authors [1,10,32,50,52].

5.2.2 Model Validation

With this geometrical setup, the heat current components perpendicular to the energy flow should be negligible. Indeed, that is the case where the perpendicular flow was around 1% of the axial flow. As expected, the longer the time over which the data were averaged, the lower the perpendicular flow became.

Both $\vec{J}$ and T were calculated in the NEMD setup described above and then the lattice thermal conductivity κ is obtained from Fourier's law (Equation 31). The κ was determined for five temperatures: 150K, 300K, 500K, 750K, and 1000K. Results obtained here are close to results in Ref. [68] using a potential proposed by Halicioglu [69]. The results closely match the experimental values for bulk SiC in Ref. [70], the κ values and temperature relationship for armchair nanotubes in Ref. [71] and for nanowires in [62,68]. The work presented in this dissertation has investigated more temperature variations and more types of nanowire configurations and has included the previously unstudied zigzag nanowires.

5.3 THERMAL CONDUCTIVITY IN NANOSTRUCTURES

5.3.1 Nanowires

Nanowire configurations carved from the 3C and 2H crystalline polytypes of SiC in the [-100], [-111] and [001], [110] directions, respectively, (Figure 28) have been previously demonstrated to be stable under a tight binding model [20]. The nanowires simulated kept their structure up to temperatures of 1000K under the model potential used in this work. The MD averaged energies per SiC pair extrapolated to zero temperature were -11.75 eV and -11.46 eV for 3C [100], [-111] and -11.98 eV and -11.43 eV for the 2H [100], [110], nanowires, respectively. These results matched qualitatively the tight binding energies per SiC pair of -11.7 eV and -11.0 eV for 3C [-100], 3C [-111], and -11.6 eV and -10.3 eV for 2H [001], [110] nanowires calculated in Ref. [20].

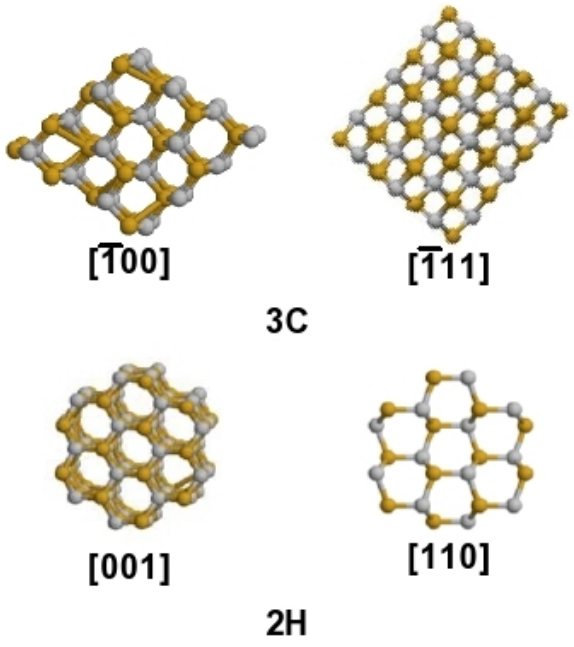

Figure 28: SiC Nanowire cross sections

The MD equilibrated configurations of these four nanowires were taken as initial configurations for the NEMD simulation. The results are shown in Figure 29, where the filled symbols (♦, ▲) correspond to the 3C wires and empty symbols (○, □) correspond to the 2H wires.

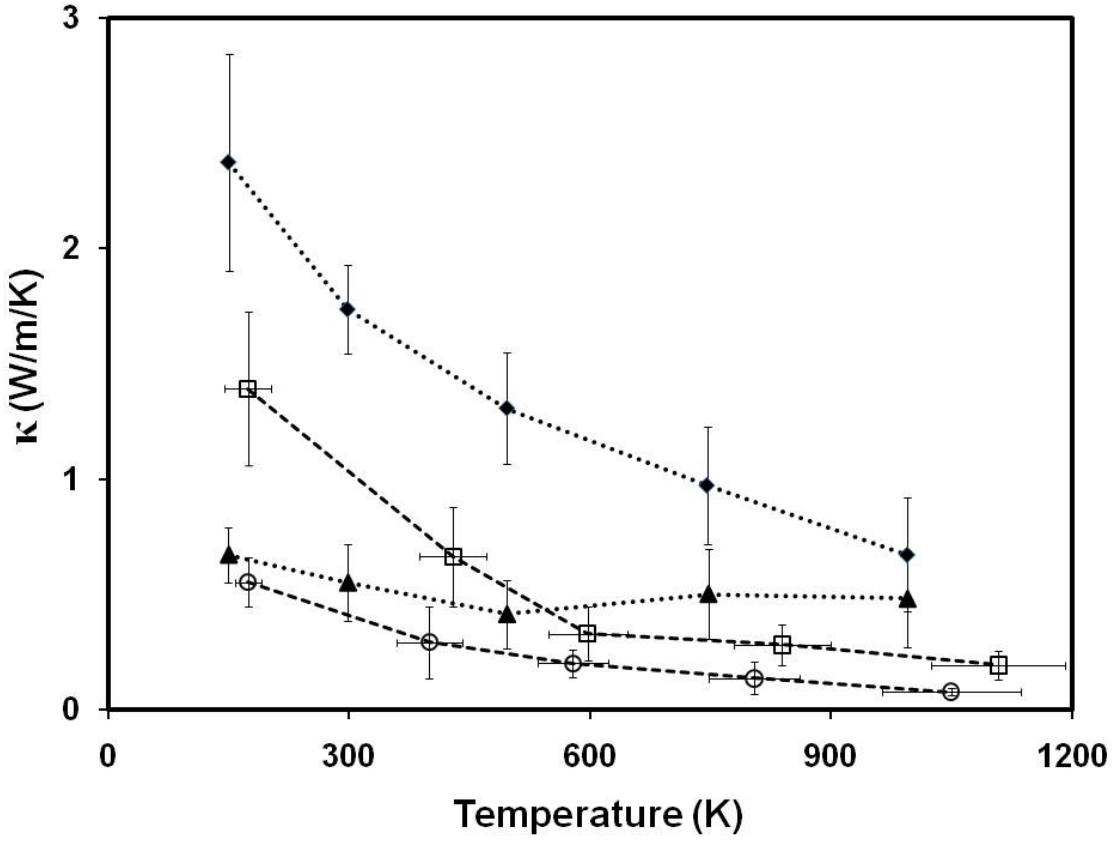

Figure 29: Thermal conductivity as a function of temperature for nanowires: 3C [$\bar{1}00$] (♦), 3C [$\bar{1}11$] (▲), 2H [001] (○), and 2H [110] (□)

The 2H [110] and the 3C [$\bar{1}00$] nanowires follow an inverse power law for temperature as is expected in bulk systems and described in Chapters 3 and 4. The inverse power law

is $\kappa = \frac{\alpha}{T}$ where α is a constant. However, the other two wires in the temperature range studied, display an almost constant thermal conductivity suggesting that these wires are less sensitive to temperature variations.

5.3.2 Armchair Nanotubes

Four armchair nanotube sizes were simulated: (2,2), (3,3), (4,4), and (5,5), as suggested by [68]. In reaching an equilibration for the four nanotubes, the (2,2) and (5,5) armchair nanotubes were stable and remained as nanotubes in the range 150 K – 1000 K, while the (3,3) and (4,4) armchair nanotubes collapsed into a flatten structure which are referred to as nanofilaments. Once the nanotube collapsed to the nanofilaments for the (3,3) and (4,4) armchair nanotubes, the resulting structures remained stable and equilibrated well. Figure 30 shows these resulting configurations.

The dependence of κ with temperature for these armchair tubes and filaments is shown in Figure 31, where ♦ and ▲ correspond to the armchair nanotubes (2,2) and (5,5) and □, ○ correspond to nanofilaments generated from the (3,3), (4,4) nanotubes, respectively.

The (2,2) nanotube follows the inverse power law for temperature. However, the others follow a power law to a power of -0.65 for the two nanofilaments and -0.4 for the (5,5) nanotube. These results suggest that the (5,5) nanotube is too open a structure to carry heat efficiently and therefore insensitive to temperature variations with regards to its thermal conductivity.

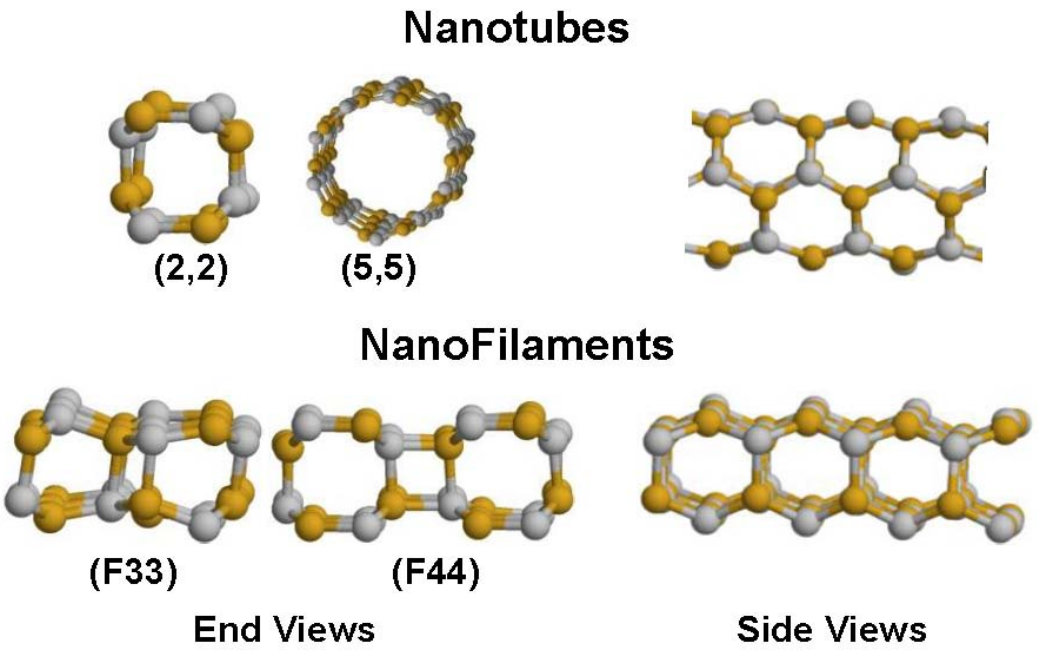

Figure 30: Armchair nanotubes and nanofilament configurations

The average energy per SiC pair extrapolated to zero temperature was -11.4 eV for both the (2,2) and (5,5) nanotubes and -11.5 eV, -11.63 eV for the (3,3), (4,4) tubes that collapsed to nanofilaments. Energies of both the (2,2) and (5,5) nanotubes are in qualitative agreement with the tight binding results of 10.0 eV, 10.5 eV [20] and are close to those calculated with MD by [62].

5.3.3 Zigzag Nanotubes

The zigzag nanotube (4,0) remained stable and equilibrated well in a configuration similar to the initial structure while zigzag nanotubes (6,0), (8,0), and (10,0) collapsed into a nanofilaments. The structure of these filaments was different from filaments obtained from the armchair nanotubes. The resulting zigzag filaments have structure

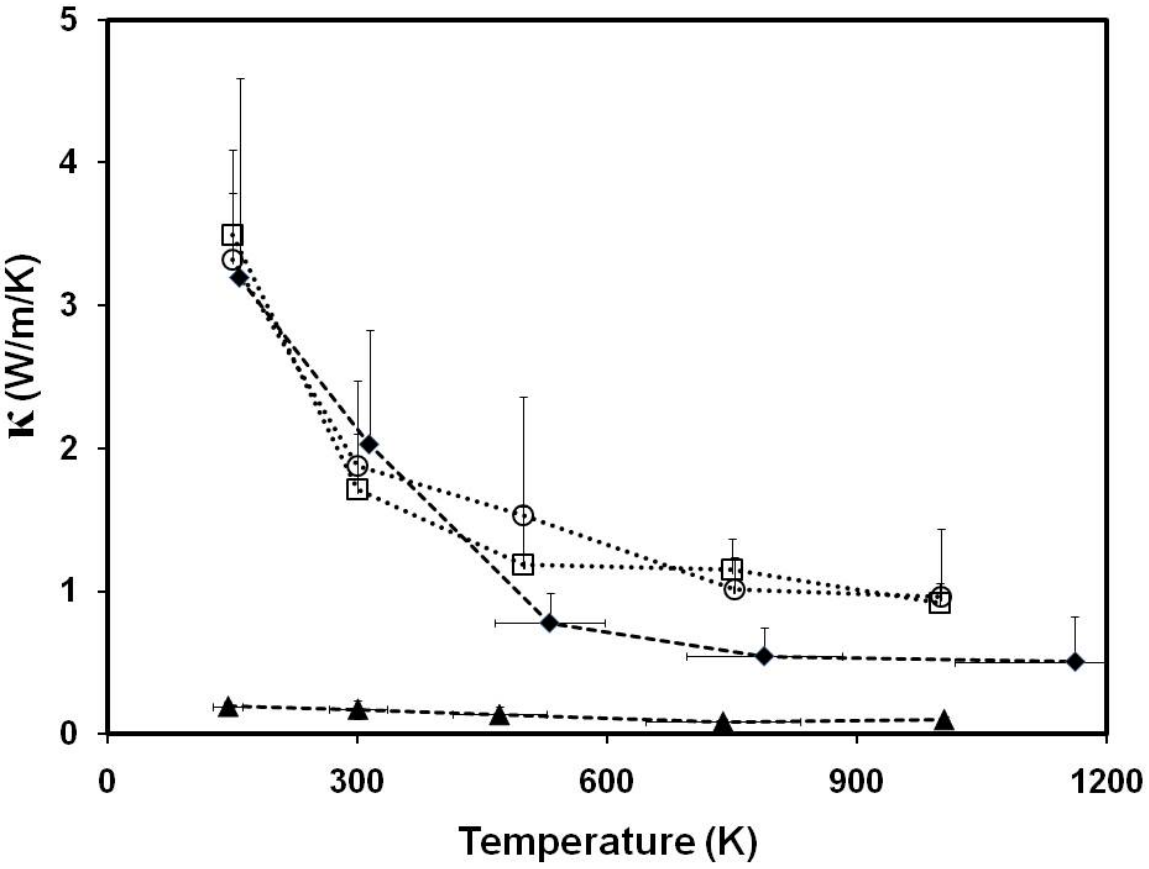

Figure 31: Thermal conductivity as a function of temperature for armchair nanotubes and nanofilaments: (2,2) (♦), (5,5) (▲) nanotubes, and (3,3) (□), (4,4) (○) nanofilaments

with a (4,0) nanotube paired with either hexagonal rings on the side or a (2,0) nanotube paired with a series of (4,0) nanotubes. Figure 32 shows these resulting zigzag nanotube and nanofilament configurations.

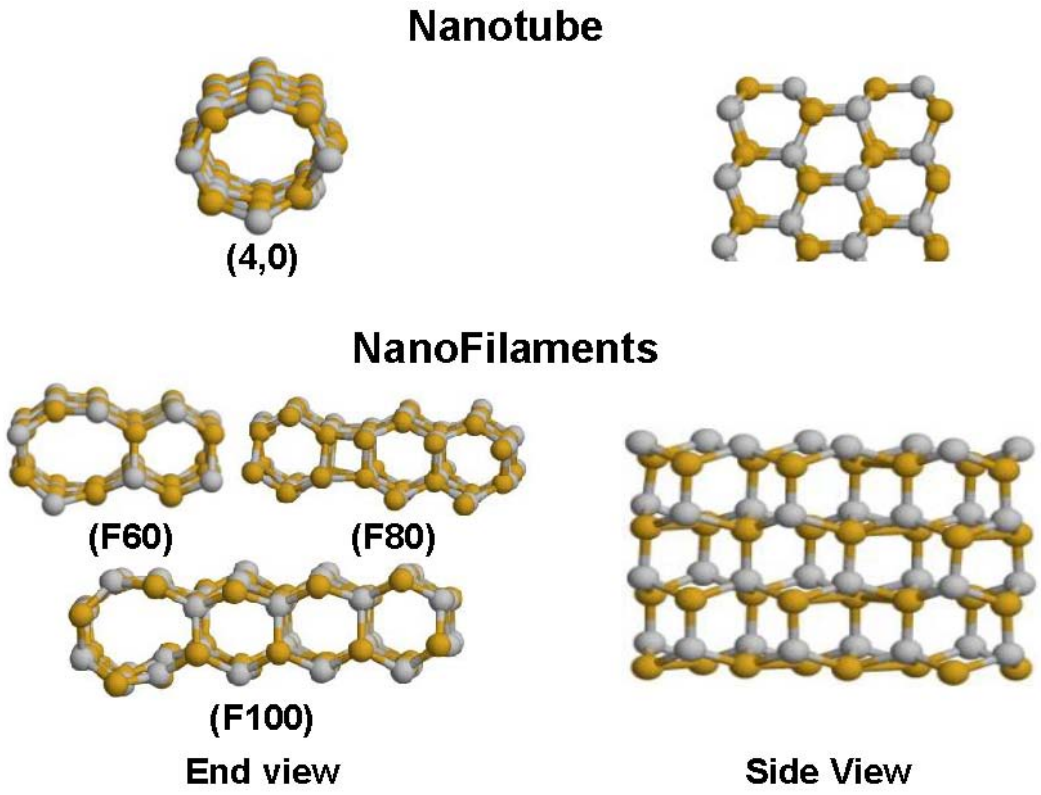

Figure 32: Zigzag nanotubes and nanofilament configurations

Figure 33 shows the dependence of κ with temperature, where ♦ corresponds to the nanotube (4,0), and Δ, ○, and □ correspond to the nanofilaments collapsed from the (6,0), (8,0), (10,0) nanotubes, respectively. A structural change from hexagonal rings of Si-C atoms into rings of 5 or 7 atoms has been observed by other researchers for both types of nanotubes under thermal and mechanical stresses [21,61,65,66,71].

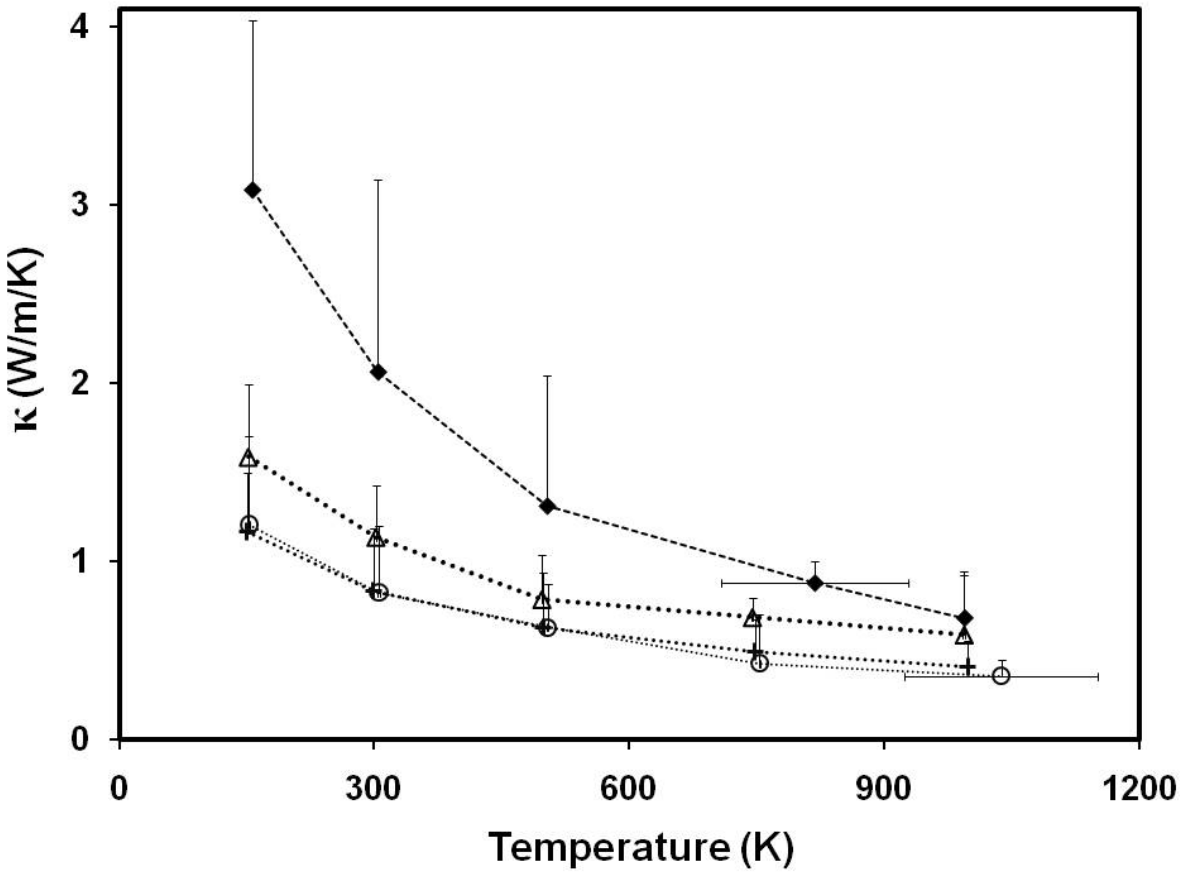

Figure 33: Thermal conductivity as a function of temperature for zigzag nanotubes and nanofilaments: nanotube (4,0) (♦), and nanofilaments (6,0) (Δ), (8,0) (○) and (10,0) (□)

None of the zigzag nanotube and resulting nanofilaments follow the inverse power law for temperature. The power of -0.77 (4,0), and -0.6 for the nanofilaments was observed, suggesting that the zigzag nanotube and nanofilaments are not very sensitive to temperature variations with regards to thermal conductivity.

The average energy per SiC pair at a zero temperature was -11.4 eV for the (4,0) nanotube and -11.6, -11.7, and -11.7 eV for the nanotubes (6,0), (8,0, (10,0) collapsed to nanofilaments. The (4,0) nanotube energy compares well with the tight binding energy of -10.5 eV [20].

5.4 NANOSTRUCTURE THERMAL CONDUCTIVITY CONCLUSIONS

The results in this work have gone farther than published works to determine the thermal conductivity of SiC nanostructures in the temperature band of 150K-1000K. The results show that NEMD techniques can be used to further investigate the κ and thermal response for entire nanodevices. The NEMD potential used is stable and may also be useful in determining the structural stability of nanodevices under a thermal current as well.

While the κ has been shown experimentally for bulk SiC, it was found that when nanostructures are fabricated from SiC, their κ decreases based strictly on the structure used for nanotubes and the orientation of the lattice inside of nanowires. Likewise, the SiC nanostructures investigated also showed a wide variation in how they respond under various temperature conditions from following an inverse power law as found in bulk materials to being almost insensitive to changes in temperature. This temperature sensitivity may be critical to the design and operations of nanodevices and their intended uses in electrical, and mechanical applications and definitely warrants further investigation by other researchers.

CHAPTER 6 COMPUTATIONAL CHALLENGES

6.1 COMPUTATIONAL EFFECTS

During the computational analyses a few special items of concern are reviewed below.

6.1.1 Counteracting PBC effects

Molecular simulations are based on averages over large numbers of atoms for large periods of time. The computing time increased by a factor of n to n^2, where n is the ratio of the number of atoms. However, this is not practical, even with today's computing capabilities, so smaller simulation configurations are commonly used. A concern with a smaller system, the edges of the system can have a dramatic and negative effect on the accuracy of the simulated data, so PBC are used. Commonly, PBC are used with symmetric sized simulations use a repeating computational box, known as a PBC primary cell, which is a square or a cube [14].

The simulations presented in Chapter 3 used a cubic computational box which became the PBC primary cell with PBC imposed equally in all three dimensions. The concern with these simulations was to have the system being as small as possible yet not have the results effected by the use of PBC. Various sizes of systems were tested (as shown in

Figure 13, section 3.2.1) as a macro test to see how the parameters of ρ, κ, or energy were affected by the system size. As a result, the 5 FCC size was chosen for that research.

The simulations presented in Chapter 4 used a square prism computational box representing a cross section of thin film system across the total width of the film. The PBC primary cell was the entire square prism and PBC imposed in two dimensions to simulate the film was infinite in size with the finite width. The work began with a size of 5 FCC in each dimension as well, however with this research, the wavelength of the simulated thermal phonons was being investigated. With the study of dynamical properties, PBC effects can be more pronounced than with mechanical properties.

As a result, the concern was if the size of the directions using PBC was large enough to not experience the effects of the PBC in the tails of the autocorrelation functions [14,73,74]. This occurs when the time lag used in the autocorrelation function, τ_{relax}, exceeds the time that it takes for a wave traveling at the sonic velocity of the material to cross the system, τ_{pbc}.

$$\tau_{pbc} = \frac{L}{v_s} \tag{38}$$

where L is the width of the system and v_s is the sonic velocity. From the low frequency region of the velocity autocorrelation Fourier transform, an estimate of about 3 is obtained for the sonic velocity. To make certain that the system was not subject to these effects, both of these times were closely monitored. The τ_{relax} used was calculated as the decay time of the autocorrelation function as an average over ten time dependent velocity autocorrelation functions with different initial times [72]. For the monatomic

reference system at T = 0.12 and 0.33 using $512\Delta t$, calculation of these two times was repeated for various computational box cross sections showing that $5x5$ FCC unit cell cross sections (100 atoms) yield a $\tau_{pbc} \cong 2.6\ t_A$, which is longer than $\tau_{relax} \cong 0.2\ t_A$, where t_A is the reduced time unit for the system. Other material simulations were also tested and did not violate this condition either. Thus, effects of the boundary conditions are negligible and the use of PBC did not degrade the results.

6.1.2 Software Error Handling

During the initial steps in establishing a new trial or a new configuration, the software had to have several error handling and error prevention routines installed to prevent the configuration from expanding rapidly and essentially ejecting atoms. With a new trial, the positions of each atom were set into a perfect lattice or structure configuration for the postulated density for the trial temperature. Unfortunately, the velocities for each atom could not be set in an exact manner where they would be near an equilibrium or steady state condition on the first few steps, instead, the velocities were chosen from a random normal distribution around the trial temperature. As a result, the possibility existed that two velocities would cause atoms to become too close and produce large forces which, in the next step, would produce a large velocity and eject the atom from the computational box. The error handling installed would temper the forces so that their velocities would not be relatively large. This was done by establishing a minimum distance at which the forces would be calculated. Additionally, a new configuration was initially allowed to

equilibrate at an extremely low temperature (less than 1K) before being warmed to the trial's temperature.

An additional error handling was to periodically do minor corrections of the positions and velocities to ensure that there was no motion of the center of mass of the computational box. Slight movements were observed due to round off errors and the time step being chosen at the upper bounds. This was done by simply summing the positions or velocities then finding the average value and correcting by the opposite value. A system with no movement in the center of mass should have zeros as the summed values. For simulations after equilibration, the sums were on the order of a factor of 10^{-13}. This is expected for runs in double precision.

6.1.3 Energy Conservation Test

A computational box was allowed to reach equilibrium and stored. Then the stored equilibrium configuration is allowed to react for a given time period. The square root of the standard deviation of the energy was plotted for various time step sizes. The result should be a straight line passing through zero for a step size of zero. Figure 34 shows a sample result. From this result, the maximum time step that could be used is where the result remains on the straight line. For simulations, the step size was chosen to be about ¾ of this value.

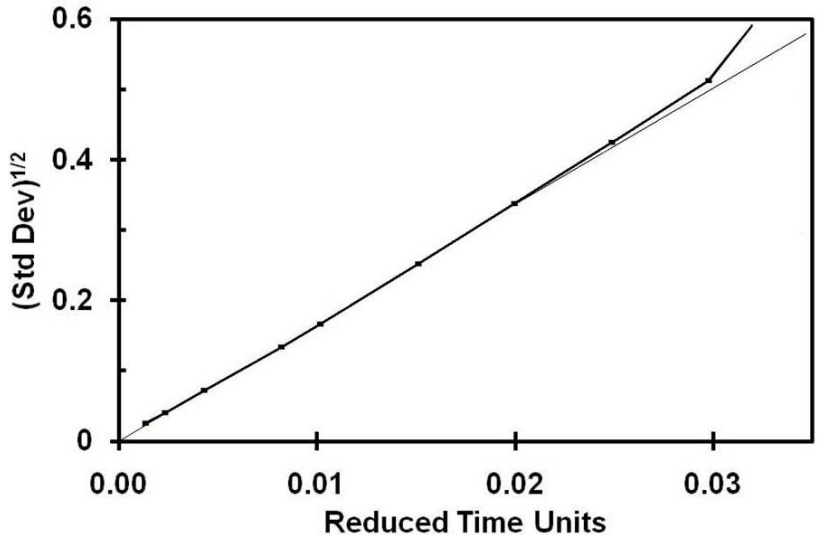

Figure 34: Square root of the standard deviation as a function of time step size

6.2 SOFTWARE USED

6.2.1 Computational Software Environments

All of the computational software routines used in the research study were written from scratch by the author using Fortran 90 and Fortran 95 with the exception of the Fourier Transformation routine provided in Ref. [75].

The majority of the computational software was run on a variety of personal computers using the Intel Pentium 4 ® family of processors. Additionally, some of the code was run on a variety of UNIX based machines located in the GMU Computational Sciences and Informatics Department laboratories. Both the PC and UNIX based machines used a

Fortran compiler and run-time environment developed by the Portland Group Compiler Technology, of Portland Group, Inc (PGI®), a company within STMicroelectronics, Inc, of Wilsonville, Oregon [76].

A multiprocessor parallel computer facility at the GMU Computational Sciences and Informatics Department called "Bach" was also used for some of the runs [77]. Bach uses 64 Intel Itanium 2® processors in a SUSE Linux® operating system. The Bach uses the Intel® Fortran Compiler "ifort" version 9.0.

6.2.2 Fortran Code

The Fortran code developed for the research was limited by the versions of Fortran supported on the compiler versions of the various machines used. Each of the Fortran compilers supported OpenMP [78] which was used to assist in optimizing performance of the code and utilizing the multi-processor capabilities on each of the machines used. The OpenMP support group defines OpenMP as: "a portable, scalable model that gives shared-memory parallel programmers a simple and flexible interface for developing parallel applications for platforms ranging from the desktop to the supercomputer." Appendix B provides several examples of the software developed. Each of these examples was embedded in an OpenMP routine.

The use of multi-processors reduced the time needed to run the computational software. The PC used during the final stages of the research uses an Intel ® Core 2™ Quad CPU Q9300 running Windows Vista® which automatically used all available processors. Runs on the older PCs with Pentium 4 ® processors showed about a 35% decrease in

time required to run the simulations. Previously it was stated that using the fewest number of atoms in a simulation would reduce the time needed to run simulations. Figure 35 shows the processing time required for various system sizes.

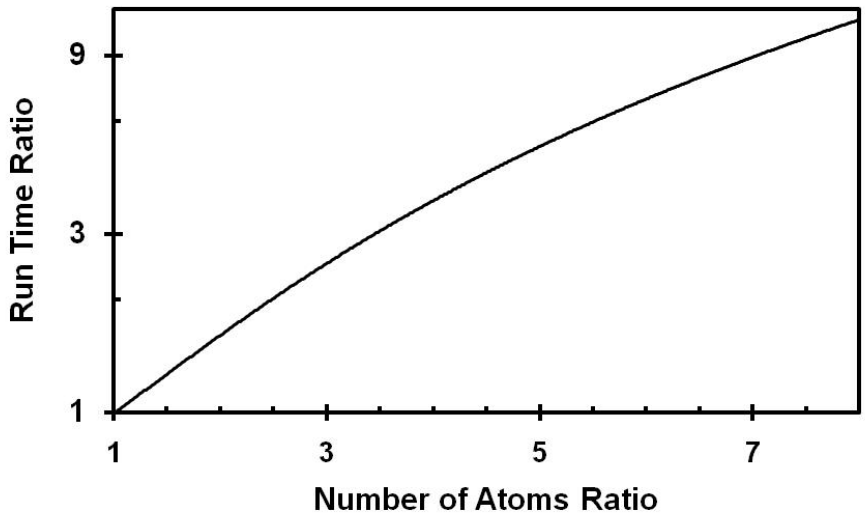

Figure 35: Processing time required for various system sizes

For a computation that compares each atom against every other atom, the number of calculations increases at roughly at n^2, where n is the ratio of atoms. However, in the system used in this research, there is a limit on the range that forces were calculated so the number of calculations would increase by n^2 until the force range was reached, then it would increase somewhat closer to *n* where the increase is due to the overhead of the number of atoms calculated. It can be seen that for the low atom ratios, the time required

increases rapidly, then as the ratio increases, the rate of time increase is more linear. Runs were made using the 3C[100] configuration.

6.2.2.1 Monte Carlo Programmatic Flow

The software programs used the flow diagram for MC programs as shown in Figure 36.

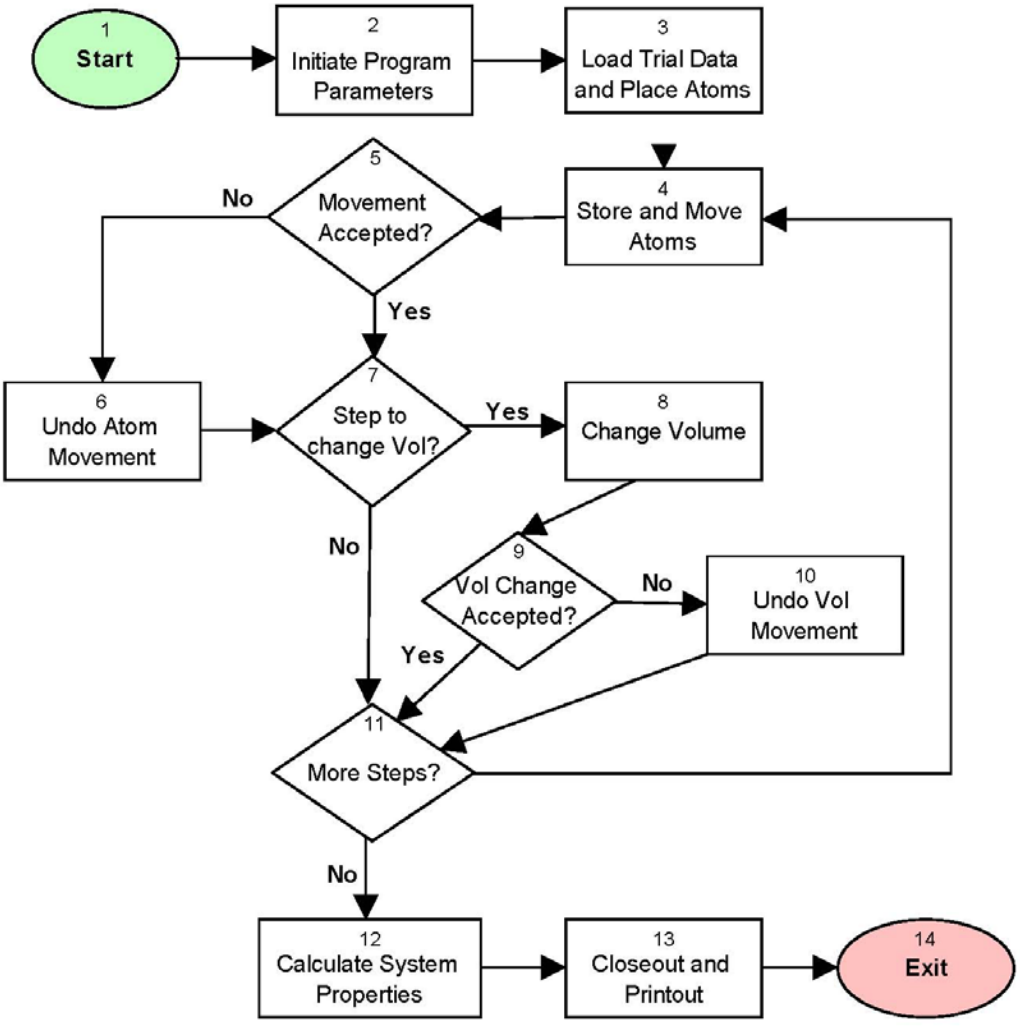

Figure 36: MC programmatic flow diagram

The steps in Figure 36 are as follows:

Step 1: Program call

Step 2: Initiate program parameters. In this step the variables, vectors, and arrays are defined, and pressure and temperature constants and other given properties are established.

Step 3: Load trial data and place atoms. The input file is read which gives parameters needed to determine the run length and other variable parameters. The atoms in the configuration are placed into their initial positions.

Step 4: Store and move atoms. The positions of the atoms are first saved then moved one random position step. The energy of the system is determined.

Step 5: Movement accepted? The selection criteria is established to see if the movement results in a lower energy or a higher energy which is permitted by the acceptance criteria defined in section 2.1.2.2, equation (8), and section 3.1.1.

Step 6: Undo atom movement. If the movement is not accepted, the atom positions are reset to their previous positions.

Step 7: Step to change vol? One MC volume change is done every 3rd atomic movement step. It is determined if this is the third step.

Step 8: Change volume. The volume of the system is increased or decreased by one random size step. The energy of the system is determined.

Step 9: Volume change accepted? The selection criteria is established to see if the volume change results in a lower energy or a higher energy which is permitted by the acceptance criteria defined in section 2.1.2.3, equation (10), and section 3.1.1.

Step 10: Undo volume change. If the volume change is not accepted, the atom positions and volume are reset to their previous positions and size.

Step 11: More steps? If there are ,more MC steps to be performed, the program returns to step 4.

Step 12: Calculate system properties. Properties are calculated from the atomic positions.

Step 13: Closeout and printout. The Data is written to files, then the open data files are closed. Printouts are provided to the screen giving final results and runtimes.

Step 14: Exit.

6.2.2.2 Molecular Dynamics Programmatic Flow

The software programs used the flow diagram for MC programs as shown in Figure 37.

The steps in Figure 37 are as follows:

Step 1: Program call

Step 2: Initiate program parameters. In this step the variables, vectors, and arrays are defined, and constant properties are given.

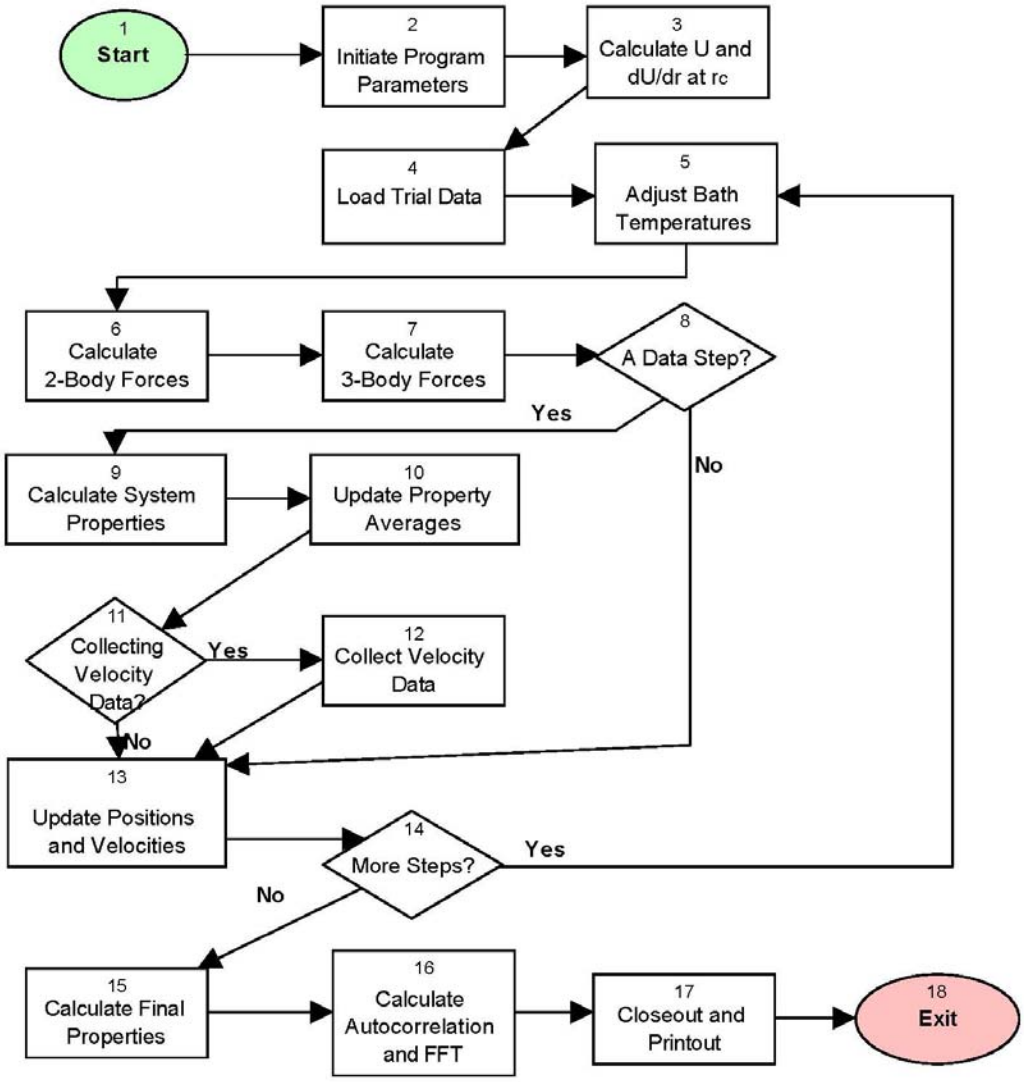

Figure 37: MD programmatic flow diagram

Step 3: Calculate U and $^{dU}/_{dr}$ at r_c. For the force shift, the energy and force are calculated at r_c.

Step 4: Load trial data. The input file is read which gives parameters needed to determine the run length, time step size, and other variable parameters. The atoms

locations are read in and placed into their initial positions. The velocities of all of the atoms scaled to satisfy the selected temperature profile.

Step 5: Adjust bath temperatures. The atom velocities in each thermal bath are adjusted to the bath set temperature.

Step 6: Calculate 2-body forces. The two-body forces are determined for each atomic pair in the system. If atoms are beyond the maximum two-body force cutoff distance, the atomic pair is skipped. The potential for each atom and the forces on each atom are summed.

Step 7: Calculate 3-body forces. The three-body forces are determined for each atomic triple in the system. If any pair of atoms in the triplet are beyond the maximum three-body force distance, the atomic triplet is skipped. The potential for each atom and the forces on each atom are summed.

Step 8: A data step? If the step that is being calculated is during the equilibration or relaxation phases, (aka prior to collecting data), the program skips to step 13, otherwise continues to step 9.

Step 9: Calculate system properties. The heat current is calculated from the atomic positions, atomic potentials, and forces on each pair of atoms.

Step 10: Update property averages. The heat current and temperatures are averaged and variances are calculated.

Step 11: Collecting velocity data? If the current step being calculated is a part of the last steps determined for the collection of vibrational data, then the program moves to step 12. Otherwise the program skips to step 13.

Step 12: Collect velocity data. The velocity is stored for each atom in each direction.

Step 13: Update positions and velocities. The velocities and positions of each atom are updated.

Step 14: More steps? If there are remaining step to calculate, the program returns to step 4. Otherwise, the program continues to step 15.

Step 15: Calculate final properties. The calculated parameters of heat current, and temperature are calculated.

Step 16: Calculate autocorrelation and FFT. From the stored velocity data, the autocorrelation is calculated in each direction in 10 time increments, the FFT of the resulting autocorrelations is calculated and then averaged to find the DOS.

Step 17: Closeout and printout. Data is written to files, then the open data files are closed. Printouts are provided to the screen giving final results and runtimes.

Step 18: Exit.

6.2.2.3 Comparison of MD and NEMD Flow

Figure 38 illustrates the basic flow of the MD and NEMD methodologies. The difference in code development is that the MD code must continue until the parameters are

producing a constant average value for all parameters across the computational box then data can be collected from this equilibrium state. While the NEMD code must first achieve an equilibrium state like in the MD, then a set of parameters, like the temperature bath in this study, and the system allowed to stabilize. The system will have reached the stable steady state condition when the parameters change in a relatively smooth manner from the value at one end to another. Then data can be sampled at various points along the axis of the non-equilibrium condition to achieve a gradient of values.

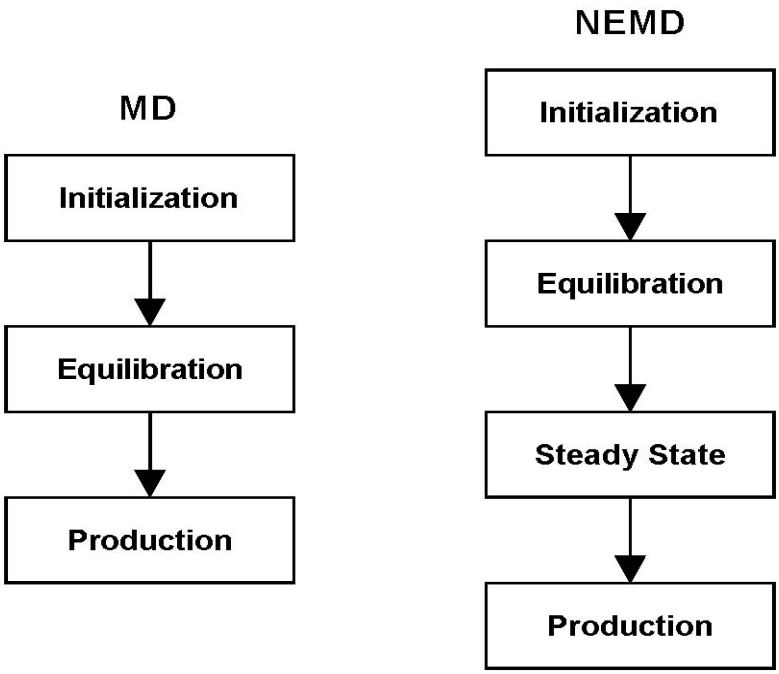

Figure 38: Comparison of MD and NEMD Flow

6.2.3 Graphics Software

Graphics and data reduction was done using a variety of tools which included MATLAB® and Excel®. The MathWorks, Inc, product MATLAB® Student version 6.0 was used. The MATLAB Editor® was used for developing MATLAB code. The MATLAB was used to produce some of the post-processing graphics. Additionally, Microsoft's Excel® (versions in 2000, 2003, and 2007) was used for data reduction, analysis and plotting. For producing representations of atomic configurations, RasMol [79] was used. RasMol was developed in the early 1990's to graphically represent complex atomic structures and proteins. In the past few years, RasMol was updated to run on several operating systems and was renames to become RasWin which was also used in this research.

6.2.4 Supporting Software

Other products used include: Microsoft's Word® and Notepad® were used to develop Fortran code, and Microsoft's PhotoEditor® and Paint® were used for graphics 'clean-up.'

CHAPTER 7 CONCLUSIONS

In conclusion, this study has presented a detailed analysis of the thermal conductivity of changes in material properties and the effects of internal boundaries using MD and MC computational simulation methods. This study has also presented a detailed analysis of the thermal conductivity and possible stability of several configurations of SiC nanowires and nanotubes. This work has been successfully validated against theoretical and experimental work.

Several highlights are as follows for the work done with bulk binary homogeneous LJ systems. Selection of materials by their mass, hard-core atomic diameter, well depth, and relative concentration can change the κ by as much as an order of magnitude. When the hard core radius increased by only 10%, the κ decreased by 90% due to increased phonon scattering. While a 60% increase in mass only decreased the κ by 25% and a 50% decrease in interatomic strength decreased the κ by 25% due to the amount of energy needed to vibrate the system and conduct heat. The effect on κ followed an inverse temperature relationship for mass and interatomic strength variations, yet when the hard core radius increases, the κ becomes relatively insensitive to temperature.

Several highlights are as follows for the work done with thin films. The study showed that for films that are made of a single pure material with no internal boundaries, the frequencies of the phonons carrying heat energy change due to the material as the parameters changed. Increases in hard core radii enhanced the higher frequency (transverse) phonons while increases in interatomic bond strength increased all phonons roughly equally while increases in mass increased the lower frequency (ballistic) phonons. For materials with internal boundaries, mass increases across a boundary enhanced the lower frequency phonons, where changes across a boundary produce the opposite effect as increases in hard core radius and interatomic strength enhanced the higher frequency phonons. Additionally, it was found that these effects were diminished for higher temperatures around half of the Debye temperatures.

Several highlights are as follows for the work done with SiC nanowires and single walled nanotubes. The study showed that the structural changes produced vastly different κ. In nanowires, the orientation of the internal lattice determined whether (1) the κ approximated that of the bulk SiC and followed a inverse temperature relationship or (2) the κ was decreased by more than 50% from the bulk SiC and appearing to have a constant κ of SiC near its melting point. For the nanotubes, the smaller nanotubes approximated the κ of bulk SiC while as the structure increased in size, the κ decreased dramatically. When the nanotubes collapsed into a stable nanofilaments, the κ was slightly enhanced over the expected κ if it had remained a nanotube.

To support this study, all computational software was developed by the author. The use of basic computing methods shows that MD and MC work can be performed on the range of modern PC processors in reasonable amounts of time using the inherent parallel capabilities in those processors. The use of massively parallel computing machines did enhance the processing speed, however, the time improvement for software which uses relatively short parallel steps was not dramatic.

With the growing use of nanotechnology and nanodevices in many fields of engineering and science, a need for understanding the thermal properties of such devices has increased. The results of this study can be used in the design of nano-machines where heat generation and transport is a concern. Follow-on studies could be initiated to investigate specific designs of discrete and very long nano-devices. Further work could be initiated on macro systems where the selection of materials could produce nano-machines which transport heat away from other nano-devices to lengthen their operating life or allow them to operate more efficiently. A further out goal of this work could be to produce macro devices that could be integrated with computer chips to carry away heat to eliminate the need for fans in computers or active cooling systems aboard spacecraft. These devices, coupled with similar work with electrical conductivity of nano-materials could produce these cooling devices which recycle the waste heat into electricity allowing for longer battery life and more ‘green’ devices.

APPENDIX A PUBLISHED PAPERS

A.1 Published Paper: Acta Materialia, vol 54, pp4633-4639, 24 August 2006 [9]

Available online at www.sciencedirect.com
ScienceDirect
Acta Materialia 54 (2006) 4633–4639
Acta MATERIALIA
www.actamat-journals.com

Computational study of heat transport in compositionally disordered binary crystals

John W. Lyver IV [a,b], Estela Blaisten-Barojas [a,*]

[a] Computational Materials Science Center, College of Science, George Mason University, Fairfax, VA 22030, USA
[b] Office of Safety and Mission Assurance, National Aeronautics and Space Administration, Washington, DC 20546, USA

Received 20 March 2006; received in revised form 26 May 2006; accepted 27 May 2006
Available online 24 August 2006

Abstract

The thermal conductivity of compositionally disordered binary crystals with atoms interacting through Lennard-Jones potentials has been studied as a function of temperature. The two species in the crystal differ in mass, hard-core atomic diameter, well depth and relative concentration. The isobaric Monte Carlo was used to equilibrate the samples at near-zero pressure. The isoenergy molecular dynamics combined with the Green–Kubo approach was taken to calculate the heat current time-dependent autocorrelation function and determine the lattice thermal conductivity of the sample. The inverse temperature dependence of the lattice thermal conductivity was shown to fail at low temperatures when the atomic diameters of the two species differ. Instead, the thermal conductivity was nearly a constant across temperatures for species with different atomic diameters. Overall, it is shown that there is a dramatic decrease of the lattice thermal conductivity with increasing atomic radii ratio between species and a moderate decrease due to mass disorder.

Keywords: Binary solids; Compositional disorder; Monte Carlo; Thermal conductivity; Molecular dynamics

1. Introduction

It is known that heat is transported better through solid materials that are pure and crystalline. Any type of impurity, defect, doping or internal boundary within the material nominally increases the resistance to heat transport, and thus reduces the ability to conduct thermal energy. With the growing interest in nanotechnology, the study of thermal conduction properties of systems with reduced dimensions, thin films, nanotubes and superlattices has increased. In nanomaterials and nanostructures, phenomena are highly dependent on the length scale where vibrations between nearest-neighbor atoms occur. The use of molecular dynamics (MD) and the Green–Kubo (GK) methods for calculating the thermal conductivity have shown promise as atomistic approaches for understanding nanosystems at the nanometer scale. For example, there are several recent calculations on pure noble gases with Lennard-Jones interactions and face-centered cubic (fcc) structures in which MD was the method of choice [1–5]. For binary crystals the literature is not so abundant; worth noting is the MD calculation for crystalline β-SiC with point defects [6].

In a crystal the thermal conductivity is composed of two additive contributions: lattice and electronic. The lattice contribution κ_{ph} captures phenomena associated with lattice vibrations and phonon scattering and is dominated by the structural characteristics of the crystal. The electronic contribution κ_e is proportional to the electric conductivity σ_e through the Wiedemann–Franz law [7,8]. The composition of a crystal affects the lattice symmetry characteristics and consequently the lattice vibrations. Therefore, κ_{ph}, the lattice contribution to the thermal conductivity in a crystal, should reflect changes according to its composition. In contrast, since κ_e is a function of σ_e, the conduction properties are expected to remain almost constant for families of solids with similar compositional components. A phenomenon

* Corresponding author. Tel.: +1 703 993 1988.
E-mail address: blaisten@gmu.edu (E. Blaisten-Barojas).

1359-6454/$30.00
doi:10.1016/j.actamat.2006.05.050

that reduces κ_{ph} produces an overall reduction of the thermal conductivity if the electric conductivity is not affected. In dielectrics, and the noble gases specifically, changes in κ_{ph} do not simultaneously affect the electronic conductivity.

This work focuses on simulating the lattice thermal conductivity due to atomic vibrations for binary crystals with compositional disorder. The goal of this work is to identify ranges of combinations of materials and disorder conditions which reduce the lattice thermal conductivity of the simulated binary solid mixtures and may warrant further experimental work. Throughout the remainder of this paper, κ is used to identify the lattice contribution to the overall thermal conductivity.

The effect of compositional disorder on thermal conductivity was investigated using several simple models of binary Lennard-Jones (L-J) solids. Compositional disorder was investigated due to differences in the van der Waal radii (σ), interatomic bond strength (ε) and mass (m) of the two types of atoms. Several relative concentrations of simulated crystalline binary mixtures were studied as a function of selected potential parameters and analyzed across various temperatures. The computational approach taken was to perform atomic-level computer simulations employing a combination of isoenergy MD and NPT Monte Carlo (MC) with a constant number of atoms (N), pressure (P) and temperature (T) to calculate the κ within linear response theory of many-body systems. To validate the work, results were compared to other reported results and experimental data available for monatomic crystals.

This paper is organized as follows. Section 2 describes the methodology used to prepare the binary sample, determine its equilibrium density and allow the sample to reach mechanical equilibrium. Section 3 describes the lattice thermal conductivity results obtained as a function of the parameters used, the lattice disorder models and the various concentrations of the two atomic species. Section 4 concludes the work with a summary.

2. Methodology

A crystalline binary mixture of 500 atoms was simulated in a cubic computational box with periodic boundary conditions in each direction. In the calculations, r_c is the cutoff radius taken as 49% of the width of the computational box. The composition of the binary crystal uses atoms of type "A" as the host and atoms of type "B" as the guest. All parameters were compared relative to the host A atoms. The L-J potential with parameters σ and ε was used as a prototype interaction between atoms. The compositional disorder introduced in the host lattice due to the guest atoms is modeled parameterically by changes of σ, ε and mass. Quantities are expressed in reduced units with respect to the host atoms' L-J parameters σ_A, ε_A and m_A. For example, the mass of Ar is 39.95 a.u. and that of Xe is 131.30 a.u. In reduced units, using Ar as the host atom, the mass of Ar would be 1.0, whereas the mass of Xe would be 3.3. Reduced units of length, energy, temperature, time and thermal conductivity are σ, ε, ε/k_B, $t_o = \sqrt{\sigma^2 m/\varepsilon}$ and $k_B/t_o\tau$, respectively, where k_B is Boltzmann's constant.

Four compositional mixture cases in the computational box were considered with the following characteristics: 100% of pure A atoms, 75% of A atoms and 25% B atoms, 50% of each type, and 25% of A atoms and 75% of B atoms. The L-J parameters for the binary interactions (A–B) are obtained from the combination rules:

$$\sigma_{AB} = \frac{\sigma_A + \sigma_B}{2}; \quad \varepsilon_{AB} = \sqrt{\varepsilon_A \varepsilon_B}. \tag{1}$$

Simulations started at a reduced temperature of 0.5 from a configuration with atoms placed in a perfect fcc lattice. Next, an initial configuration was constructed such that atoms were randomly assigned as type A or B consistent with the relative concentration of the two types of atoms. Throughout this study, to indicate the ratio of parameters, the symbols R_σ, R_ε, R_m are used for σ_B/σ_A, $\varepsilon_B/\varepsilon_A$ and m_B/m_A, respectively. The system was equilibrated by NPT-MC, which allowed for moves of the N atoms in random directions and changes of the entire computational box volume (V). The acceptance criterion between old (V^o) and new (V^n) configurations is given by [9]

$$\begin{aligned}\mathrm{acc}(o \to n) = \min\{1, \exp\{-\beta[U(r^N, V^n) - U(r^N, V^o) \\ + P(V^n - V^o) - (N+1)\beta^{-1}\ln(V^n/V^o)]\}\}.\end{aligned} \tag{2}$$

Here, β is $1/T$, r^N is the vector of the coordinates of all atoms and the potential energy is

$$U(r^N, V) = \frac{1}{2}\sum_{i}^{N}\sum_{i\neq j}^{N} 4\varepsilon_{ij}[(\sigma_{ij}/r_{ij})^{12} - (\sigma_{ij}/r_{ij})^{6}], \tag{3}$$

where σ_{ij} is the core radius, ε_{ij} is the bond strength and r_{ij} is the interatomic distance of an atomic pair using Eq. (1).

The NPT-MC simulations were run between 1 and 3 million steps with a step being N single atom movements and one volume adjustment. The average density and other calculated quantities were determined as an average over the final one-fourth of the NPT-MC trajectory. Therefore, the position of the atoms within the box is consistent with this average density. The density is defined as N/V irrespective of the two types of atoms, which could have different masses, σ, or ε values. Because the computational box is finite, the value of the pressure was adjusted by subtracting the pressure that would be exerted by a structureless infinite-sized sample outside of the computational box [9].

For the monatomic system, the equilibrium structure was an fcc structure for all temperatures. At low temperatures, no stable amorphous phase was found as obtained in Ref. [3]. Because the NPT-MC calculation does not include the mass in the simulation, the equilibrium ρ for binary samples with A and B atoms having only different ε is the same as the density of the monatomic system. Therefore, the NPT-MC calculations were carried out to determine ρ at different temperatures when $R_\sigma \neq 1$. Fig. 1

shows the temperature behavior of the average ρ for equilibrated systems at zero pressure for samples with a 50:50 relative concentration. The curves correspond to different R_σ. The value of ρ of pure Ar reported in Ref. [3] compares well with our results. As expected, when R_σ increases, the volume must also increase, decreasing ρ. The standard deviation (SD) of the average density is very low, of the order of the symbol size used in Fig. 1. These small fluctuations certainly ensure that the smooth decrease of ρ with temperature illustrated in Fig. 1 is indeed realistic.

The next step was to initiate the isoenergy MD study using the output of the NPT-MC runs. Each MD trial was run 350,000 time steps of $\Delta t = 0.005$ to allow the system first to equilibrate at the desired temperature. Next the MD trial continued to run for half a million time steps to calculate the desired heat current operator values from [10]

$$\vec{J} = \sum_{i=1}^{N} E_i \vec{v}_i + 1/2 \sum_{i=1}^{N} \sum_{j \neq i}^{N} (\vec{v}_i \cdot \vec{F}_{ij}) \vec{r}_{ij}, \tag{4}$$

where E_i is the total energy of each atom, $\vec{v}_i$ is the velocity of each atom and $\vec{F}_{ij}$ and $\vec{r}_{ij}$ are the force and interatomic vectors for each atomic pair.

The next step was to calculate the autocorrelation function $C(\tau)$ of the heat current operator, which is defined as

$$C(\tau) = \langle \vec{J}(\tau + t) \vec{J}(t) \rangle \tag{5}$$

where $\langle\ \rangle$ is the time average, $\vec{J}$ is the heat current operator and τ is the time lag from an origin t chosen from the time trajectory. Each autocorrelation run typically used between 2^{16} and 2^{18} time lags. It was found that for R_σ, R_ε, and R_m near a value of one required longer times to compute the autocorrelation function than when disorder sets in.

The lattice thermal conductivity κ was obtained by integrating $C(\tau)$ over the range $[0, t_{\text{traj}}]$, where t_{traj} is the total time for which the autocorrelation function was calculated. This is the GK approach [11,12]:

$$\kappa = \frac{1}{3Vk_B T^2} \int_0^\infty C(\tau)\, d\tau. \tag{6}$$

The GK approach works well for both amorphous and crystalline models as long as the system is homogeneous. GK takes full account of anharmonic properties but is classical in nature. Ladd et al. [13] were the first to use the GK formalism to calculate thermal conductivity for solids with interactions following an inverse-twelfth power law potential. Later, Gillan extended this method for the study of κ in palladium doped with hydrogen [14]. More recently, Chen et al. used this same approach to study the thermal conductivity of pure Ar doped with Xe [15].

Optimally, it would be best to calculate $C(\tau)$ out to infinity instead of just the finite trajectory length, but this is not possible numerically. We observed that $C(\tau)$ could be approximated by an exponentially decaying cosine function $e^{-\zeta t}\cos(\omega t)$ as shown in Fig. 2 and fit the parameters to the numerical MD results. Then the integration in Eq. (6) was done from the actual simulation data for $0 \leqslant \tau \leqslant t_{\text{fit}}$ and used the decaying cosine function for $t_{\text{fit}} \leqslant \tau \leqslant \infty$. The value of t_{fit} was set to be 1.25 times the period of the fitted cosine function. This time t_{fit} defines the system relaxation time.

The NPT-MC samples prepared in the manner described in previous paragraphs represent different types of compositional disorder. For all values of R_ε or R_m simulated, the structure of the equilibrated sample is the fcc lattice. Thus the system disorder is based on a random mixture of atoms A and B, which are positioned on a perfect lattice. In contrast, when size disorder was introduced with R_σ beyond 1.1, the fcc lattice collapses. This is shown in Fig. 3 which depicts the pair correlation function $g(r)$ in which the $g_{AA}(r)$, $g_{AB}(r)$ and $g_{BB}(r)$ values have been

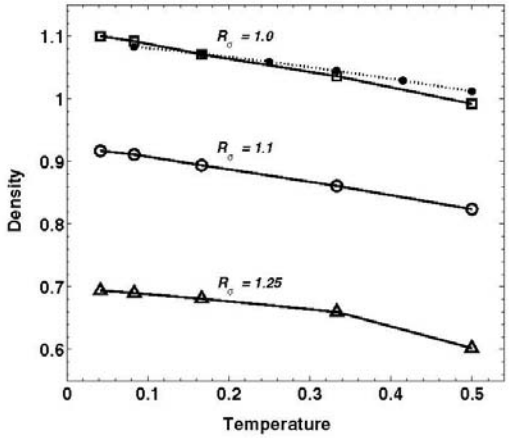

Fig. 1. Density as a function of temperature for radii ratios R_σ of 1.0, 1.1 and 1.25 for the 50:50 mixture of atoms. Crosses are ρ for pure Ar at zero pressure and circles represent results from Ref. [3].

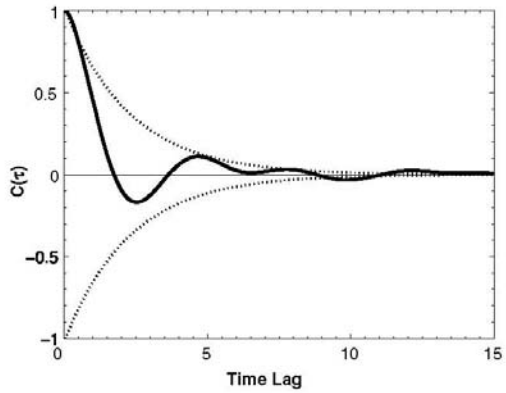

Fig. 2. MD-calculated $C(\tau)$ as a function of time. The dotted lines show the envelope of the exponentially decaying cosine function obtained from the fit of the MD data.

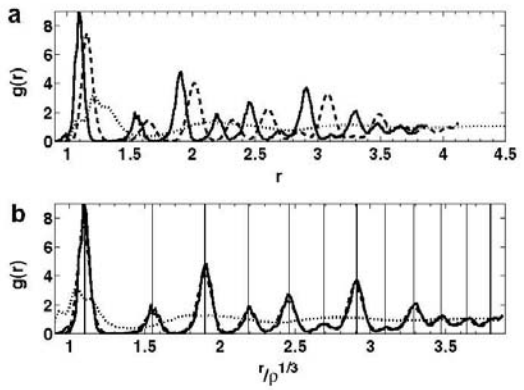

Fig. 3. Radial distribution function $g(r)$: (a) for different R_σ values: 1.0 (solid), 1.1 (dashed) and 1.25 (dotted); (b) same as in (a) plotted as function of scaled distances.

summed together. Fig. 3 shows the case of a 50:50 mixture sample at $T = 0.167$ with $R_\varepsilon = 1$, $R_m = 1$ and three different R_σ values (1.0, 1.1 and 1.25). To compare directly between these functions, a scaling of $\rho^{1/3}$ was applied to the radial dependence. It is very clear that for $R_\sigma = 1.25$, the compositional disorder of the 50:50 sample affects the structure very significantly and the crystal collapses into a homogeneous amorphous solid. The structure of this solid amorphous mixture is very different from the structure found in atomic clusters [16], where the atoms with smaller σ segregated and formed a subcluster surrounded by the large σ atoms.

3. Determination of the lattice thermal conductivity

A sample with $N = 500$ at $P = 0$ with only one type of atom was prepared, and κ was obtained for several temperatures using the steps described in Section 2. These results allowed a validation of our method by comparison with several calculations done recently [3,15,17,18] as well as with experimental results [19]. Fig. 4 shows this comparison, indicating that our results (black stars) are in full agreement with previous calculations and with the experimental results.

In the GK approach, Eq. (6), there is an explicit dependence of κ on the volume of the sample. Sample size effects were studied in Ref. [17] where the authors considered computational box sizes containing between 108 and 4000 atoms. Those authors concluded that in the temperature domain of 20–70 K, the size effects are irrelevant for all practical purposes when calculating κ for a pure Ar system. This is consistent with our findings for computational cells containing 108–2048 atoms. It was found that computational boxes smaller than 108 atoms were too small for meaningful results. Fig. 5(a) and (b) illustrates the dependence of the equilibrium density and potential energy averages as a function of the number of fcc cells (n) on each

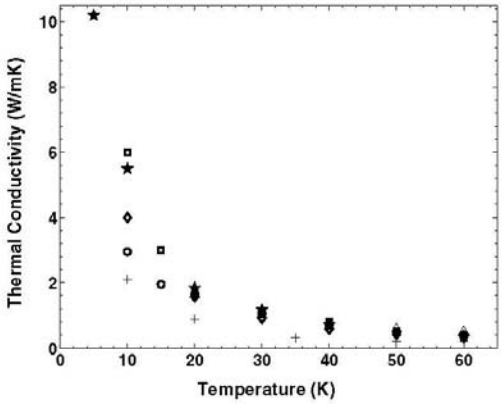

Fig. 4. Thermal conductivity κ as a function of temperature for pure Ar at zero pressure. The results of this work (black stars) are compared to those of other works: Ref. [3] (diamonds), Ref. [15] (circles), Ref. [17] (triangles), Ref. [18] (crosses), Ref. [19] (squares).

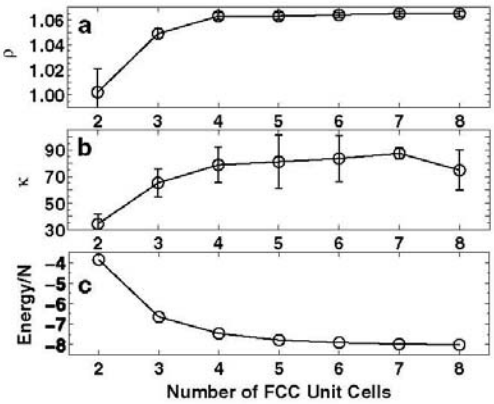

Fig. 5. Effect of computational box sizes. The horizontal axis shows the number of fcc unit cells along each side of the cubic computational box. (a) Density, (b) κ and (c) energy per atom for the ordered monatomic crystal.

computational box edge ($N = 4n^3$). Fig. 5(c) shows κ and its SD as a function of computational box size.

Based on the continued good agreement with both the previously discussed comparisons offset against run times, a system size of $N = 500$ at $P = 0$ was selected for all results reported in this work. The following compositional mixtures were considered: R_σ of 1.0, 1.1, 1.25, 1.5 and 2.0; R_ε of 1.0, 1.25 and 1.5; and R_m of 1.0, 1.6, 2.1 and 3.3. Additionally, we studied different relative concentrations of A and B atoms ranging from 100% A atoms, 75% A with 25% B, 50% A with 50% B, and 25% A with 75% B.

For samples with relative concentrations of 50:50, at a temperature of $T = 0.167$, Fig. 6 illustrates the lattice κ

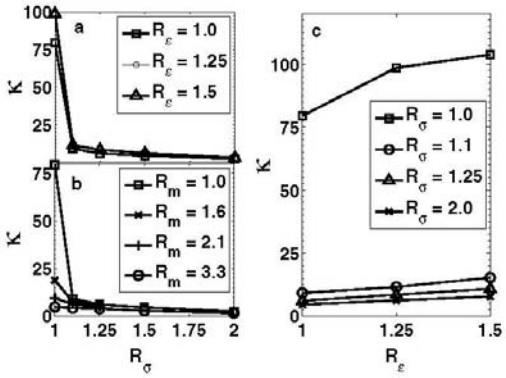

Fig. 6. Thermal conductivity as a function of the parameter ratios: (a) dependence on R_σ for $R_\varepsilon = 1$, 1.25, 1.5, and $R_m = 1$; (b) dependence on R_σ for $R_m = 1$, 1.6, 2.1, 3.3, and $R_\varepsilon = 1$; (c) dependence on R_ε for $R_\sigma = 1$, 1.1, 1.25, and $R_m = 1$.

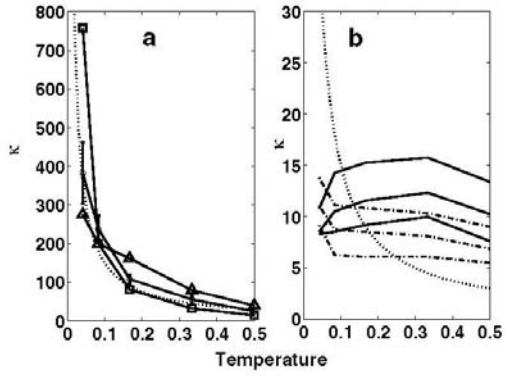

Fig. 7. Thermal conductivity as a function of temperature: (a) structurally ordered case $R_\sigma = 1$, and $R_m = 1$ with $R_\varepsilon = 1$ (squares), $R_\varepsilon = 1.25$ (circles), $R_\varepsilon = 1.5$ (triangles); (b) structurally disordered cases $R_\sigma = 1.1$ (solid lines) and $R_\sigma = 1.25$ (dashed lines). The top, middle and bottom curves are for $R_\varepsilon = 1.0$, 1.25 and 1.5, respectively.

as a function of one parameter ratio (R_σ, R_ε or R_m) while the other two parameter ratios are kept constant. Fig. 6(a) and (b) shows a dramatic decrease of κ with increasing R_σ. In fact, Fig. 6(a) shows that κ decreases by a factor of over 6 between $R_\sigma = 1$ and $R_\sigma = 1.1$ for a constant mass ratio and various values of R_ε. Likewise, Fig. 6(b) shows a dramatic decrease in κ between $R_\sigma = 1$ and $R_\sigma = 1.1$ using different mass ratios. In this case again, κ decreases by factors up to 6 depending upon R_m. While Fig. 6(b) shows a substantial decrease in κ between $R_\sigma = 1$ and $R_\sigma = 1.1$, the two atom types would have to be the same to have $R_\sigma = 1$ and $R_m = 1$, which is a very unrealistic case. On the contrary, Fig. 6(c) shows that, for $R_\varepsilon = 1$ and $R_m = 1$, κ increases slightly as a function of R_σ and increasing R_ε. This increase lies within the SDs of the κ results and might not be a real effect.

The conclusion of the parameter analysis is that at $T = 0.167$, both radii disorder and mass disorder impose a strong depletion of κ. Even a slight difference in atomic radii of only 10% has a major effect on decreasing κ while the mass ratio has a more gradual depleting effect on κ. The mass disorder leaves the crystalline symmetry intact. In comparison, the radii disorder allows the solid to acquire incipient amorphous characteristics as evidenced by the pair correlation function signature illustrated in Fig. 3. In fact for the large difference in atomic radii of 25%, Fig. 3 indicates that the fcc symmetry is already lost and the solid is no longer a crystal.

For monatomic crystalline materials, the expected theoretical dependence of the thermal conductivity with temperature follows an inverse temperature law [7,8]. While previous MD simulations [15] reported κ exhibiting this expected behavior, our results show a departure for any of the proposed samples with disorder. Fig. 7 shows the κ behavior for various values of R_ε of 1.0, 1.25 and 1.5 and $R_m = 1$ for a 50:50 concentration. In Fig. 7 the inverse temperature dependence is plotted with a dotted line to guide the eye. Fig. 7(a) depicts the temperature dependence for $R_\sigma = 1$ with the square, circle and triangle symbols identifying the three values of R_ε (1.0, 1.25 and 1.5), respectively. SDs are shown for the $R_\varepsilon = 1.25$ case and are representative of the other cases. Fig. 7(b) gives results for systems with $R_\sigma = 1.1$ as solid lines corresponding to $R_\varepsilon = 1.0$, 1.25, and 1.5 (top, middle and bottom) and dashed lines for $R_\sigma = 1.25$. SDs are about 1–2 units of κ for all results. It is apparent from these plots that the ordered crystal with no core radius disorder follows the $1/T$ relationship very closely (Fig. 7(a)) while any of the compositionally disordered systems (Fig. 7(b)) present a nearly constant κ as a function of temperature. This degrading of the thermal conduction is similar to that predicted for covalent binary crystals with defects [6] where κ was found to be essentially temperature independent. In our study it should be remembered that compositional disorder in which the atomic radii differ by only 10% produces a dramatic reduction of κ to a minimum value, which keeps fairly constant for the temperatures investigated. In summary, we emphasize that the radii disorder has an extremely strong effect to reduce κ, bringing its value to be a minimum for all calculations with widely varying material parameters.

The last part of this study pertains to changes in the relative concentrations of the A and B atoms. Relative concentrations of A:B atoms of 25:75 and 75:25 were analyzed in addition to the 100% type A and the 50:50 mixture cases discussed above. As the concentration changes, the number of smaller atoms increases relative to the larger atoms having a significant effect on ρ as shown in Fig. 8.

In analyzing mixtures with the 25:75, 50:50 and 75:25 relative concentrations over the range of T, R_σ, R_ε and

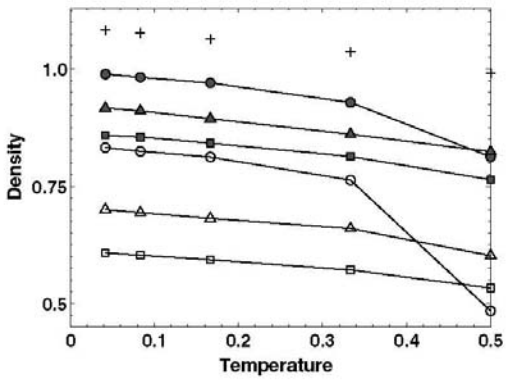

Fig. 8. Density as a function of temperature for different relative concentrations in the mixture. Filled symbols are for $R_\sigma = 1.1$ and open symbols are for $R_\sigma = 1.25$. The circle, triangle and square are for $R_\varepsilon = 1.0$, 1.25 and 1.5, respectively. The case of $R_\sigma = R_\varepsilon = R_m = 1$ is shown as crosses.

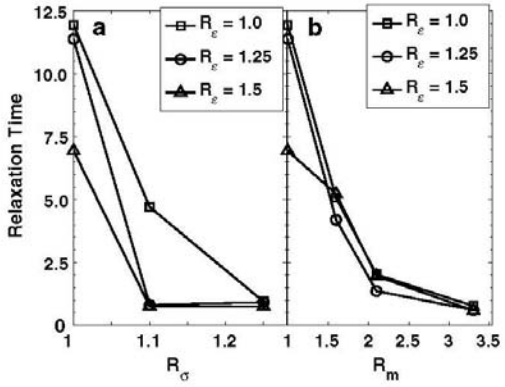

Fig. 9. Relaxation time as a function of parameter ratios for the 50:50 sample: (a) dependence on R_σ with $R_m = 1$ and $R_\varepsilon = 1$ (squares), 1.25 (circles), 2.5 (triangles); (b) dependence on R_m with $R_\sigma = 1$ and three R_ε values as in (a).

R_m, the behavior of κ was very similar to that of the 50:50 case. Table 1 summarizes all results of κ for the various disorder cases at five temperatures. Once again, for these relative concentrations studied, the maximum decrease in κ is through R_σ.

Additionally, as is shown in Fig. 6(c) for the 50:50 relative concentrations, the effect of increasing R_ε while R_σ and R_m remain constant, produced an apparent slight increase in κ. This effect is also present for the other relative concentrations as reported in Table 1.

To compute the lattice thermal conductivity from Eq. (6), the autocorrelation function $C(\tau)$ was approximated by an exponentially decaying cosine function. In Fig. 9, the vertical axis on both plots depicts the system relaxation time and is plotted as a function of R_σ in Fig. 9(a) and R_m in Fig. 9(b). The relaxation time appears to be directly related to the amount of core radii and mass disorder present in the sample. The change in relaxation time due to the ε disorder is small as evidenced by the three curves in Fig. 9(a) and (b).

Table 1
Lattice thermal conductivity for solid mixtures with various relative concentrations and at $T = 0.042$, 0.083, 0.167, 0.333 and 0.500 (top to bottom in each table entry)

Relative concentration	$R_\sigma = 1$, $R_m = 1$, $R_\varepsilon = 1$	R_σ		R_ε		R_m		
		1.1	1.25	1.25	1.5	1.6	2.1	3.3
100% A	476.6							
	200.1							
	79.5							
	31.9							
	14.5							
75% A, 25% B		8.8	5.8	331.5	184.2			
		9.5	7.1	201.1	138.8			
		10.4	6.6	98.9	75.4	22.9	12.4	7.2
		10.6	6.0	37.4	35.8			
		6.8	3.2	16.8	18.1			
50% A, 50% B		8.3	9.1	329.4	230.1			
		8.5	6.3	193.2	164.7			
		8.4	6.0	98.4	113.1	18.9	9.4	4.8
		10.0	6.1	41.8	49.9			
		7.6	5.5	23.5	26.2			
25% A, 75% B		7.5	9.4	231.2	275.1			
		9.0	6.2	331.8	199.6			
		16.9	6.3	107.9	141.3	22.8	14.7	3.6
		11.2	5.8	55.3	79.1			
		8.5	5.4	24.6	39.8			

For any parameter ratio $\neq 1$, the other two parameter ratios = 1. Values are in reduced units.

4. Summary and conclusions

Throughout this work, it has been shown that studying the effects of radii, mass, interatomic interaction disorder and temperature can be demonstrated in a computer-simulated environment. Our work was performed on a PC with a single Pentium 4 processor (3.2 GHz) and each NPT-MC and MD run consumed about 9 and 4 h of processing time, respectively, per data point, making the work reasonable to accomplish.

The results of this work show that compositional disorder at the nanoscale in crystalline binary mixtures decrease the lattice thermal conductivity in a dramatic fashion. Findings in this work are important for tailoring the synthesis of new materials with poor heat conduction characteristics. The relative properties of L-J solid mixtures are summarized below in order of importance for degrading the lattice thermal conductivity:

(1) *van der Waal radii.* Atoms should have different radii. Even a 10% difference brings the lattice thermal conductivity to a minimum constant value and suppresses the inverse temperature depletion. The reason for the dramatic degradation of the heat conduction is the additional phonon scattering imposed at the nanoscale by atoms that are at the threshold of collapsing the crystal structure of the solid.
(2) *Mass.* Atoms should have different masses. Differences of 60% in mass decrease the thermal conductivity by about half at any temperature below the melting point.
(3) *Interatomic interaction strength.* Atoms should have almost equal values. With a 50% difference in strength, thermal conductivity can be increased by about 25%, which is not a desired outcome.
(4) *Temperature.* Temperature is a key factor for any application searching to deplete heat conduction due to atomic vibrations. This work was done for reduced temperatures of up to 0.5, which are below the meting points of the L-J compositionally disordered crystals studied. In this temperature range, when radii disorder exists, the lattice thermal conductivity is essentially temperature independent and markedly degraded due to the enhanced phonon scattering induced by atoms with different radii placed randomly on an fcc crystal.
(5) *Composition relative concentration.* Relative concentration of the two components in the crystal appears to have only a minor effect on the thermal conductivity.

References

[1] Lukes JR, Dy L, Liang X-G, Tien C-L. Trans ASME 2000;122:536–43.
[2] Feng X-L, Li Z-X, Guo Z-Y. Chin Phys Lett 2000;18:416–9.
[3] McGaughey AJH, Kaviany M. Int J Heat Mass Transf 2004;47:1783–98.
[4] Chen Y, Li D, Yang J, Wu Y, Lukes JR. Physica B 2004;349:270.
[5] Heino P. Phys Rev B 2005;71:144302.
[6] Li J, Porter L, Yip S. J Nucl Mater 1998;255:139–52.
[7] Berman R. Thermal conduction in solids. Oxford: Clarendon Press; 1976.
[8] Jonson M, Mahan GD. Phys Rev B 1980;21:4223–9.
[9] Frenkel D, Smit B. Understanding molecular simulation. New York (NY): Academic Press; 1998.
[10] Balescu R. Equilibrium and non-equilibrium statistical mechanics. New York (NY): Wiley; 1979 [Chapter 21].
[11] Green MS. J Chem Phys 1952;20:1281–95;
Green MS. J Chem Phys 1954;22:398.
[12] Kubo R. J Phys Soc Jpn 1957;12:570–86.
[13] Ladd AJC, Moran B, Hoover WG. Phys Rev B 1986;34:5058–64.
[14] Gillan MJ. J Phys C Condens Matter 1987;20:521–38.
[15] Chen Y, Lukes JR, Yang J, Wu Y. J Chem Phys 2004;120:3841–6.
[16] Garzon IL, Long XP, Kawai R, Weare JH. Chem Phys Lett 1989;158:525–30.
[17] Tretiakov KV, Scandolo S. J Chem Phys 2004;120:3765–9.
[18] Kaburaki H, Li J, Yip S. Matter Res Soc Symp Proc 1998;538:503–8.
[19] Christen DK, Pollack GL. Phys Rev B 1975;12:3380–91.

A.2 Published Paper: J. Phys: Condens. Matter vol21, pp345402-345409, 5 August 2009 [10]

IOP PUBLISHING JOURNAL OF PHYSICS: CONDENSED MATTER
J. Phys.: Condens. Matter **21** (2009) 345402 (8pp) doi:10.1088/0953-8984/21/34/345402

Effects of the interface between two Lennard-Jones crystals on the lattice vibrations: a molecular dynamics study

John W Lyver IV[1,2] and Estela Blaisten-Barojas[1]

[1] Computational Materials Science Center and Department of Computational and Data Sciences, George Mason University, Fairfax, VA 22030, USA
[2] Office of Safety and Mission Assurance, National Aeronautics and Space Administration, Washington, DC 20546, USA

E-mail: blaisten@gmu.edu

Received 10 June 2009, in final form 19 July 2009
Published 5 August 2009
Online at stacks.iop.org/JPhysCM/21/345402

Abstract

Effects on the density of vibrational states due to the interface created between two types of solid Lennard-Jones systems is investigated as a function of the atomic masses and model potential parameters. The interface is responsible for a depletion of modes at low frequency and an enhancement at higher frequencies when the potential parameters are increased relative to the reference solid. Opposite trends are observed when the atomic mass increases. When a heat current is established across the interface the density of vibrational states at low frequency is increased and the temperature profile across the binary sample displays a discontinuity at the interface, which is more pronounced as the material parameters become more dissimilar. The thermal boundary resistance (Kapitza resistance) increases as the difference between the two material properties increases and decreases with increasing temperature. It is predicted that, as temperature decreases, the Kapitza length increases as T^{-2} at the nanoscale. Plots of the thermal conductivity as a function of temperature for solids with various parameters are provided, all of them showing the expected T^{-1} behavior.

1. Introduction

Large-scale integrated circuitry, components and sensors rely on internal solid–solid interfaces for controlling the operation of the device and on efficient thermal energy management for dissipating heat generated inside the device. It is then important to examine the ability of a device to transport heat when two solids meet at an interface. An appropriate selection of materials could enhance or restrict the flow of thermal energy. Since the discovery of a thermal boundary resistance at cryogenic solid–liquid interfaces by Kapitza [1], researchers have invested efforts in understanding the cause of the thermal resistance and to quantify its magnitude as a function of both material properties and parameters such as temperature and pressure. Solid–solid thermal boundary resistance has often been referred to as the Kapitza resistance (Ω_K). In solids, this boundary resistance plays an important role in determining heat flow, both in cryogenic and room-temperature applications. The acoustic mismatch model (AMM) and the diffuse mismatch model (DMM) [2, 3] are quite accurate for describing thermal transport at a solid–solid interface at low temperatures. It is also accepted that the AMM is more applicable at a few degrees kelvin, while the DMM works better at higher temperatures. However, at intermediate cryogenic temperatures and above, the experimental Ω_K is larger than that predicted by AMM and DMM. These models lack an appropriate description of the phonon scattering caused by various sources located in the immediate proximity of the interface. More recently, several works have used molecular dynamics atomistic simulations to examine properties such as the boundary resistance at flat interfaces Ω_K [4], diffuse scattering of the vibrational states at each side of the interface [3, 5], structural ordering on each side of an interface [3, 4, 6–9] and the effect of mass changes on each side of the interface on the eventual overlapping of vibrational states and energy transport [10, 11].

In parallel to the above-mentioned atomistic work, a number of authors have addressed a variety of non-

equilibrium molecular dynamics (NEMD) techniques and established these methods as the best for the determination of thermal properties in non-homogeneous systems such as grain boundaries [12–16]. For example, NEMD was used for obtaining the lattice thermal conductivity by simulating the directional heat flow perpendicular to infinite thin films in one-, two-or three-dimensional Lennard-Jones (LJ) systems [4–6, 10–19].

NEMD has been used to determine the Kapitza resistance mostly at grain boundaries or one-dimensional systems [4, 5, 16, 18, 20]. Other studies [5, 16, 18, 21, 22] have proposed that the Kapitza effect is due to reflection of the harmonic phonons at the interface or grain boundary, inelastic effects and anharmonicities. References [5, 16] are studies of a silicon grain boundary simulated with the Stillinger–Weber potential. The authors in [18] simulate the interface of two fcc lattices where one solid is composed of LJ atoms and the other of Morse-potential atoms. Reference [21] is a study of the thermal boundary resistance of an LJ system with geometry similar to the one presented in this paper; however, the acoustic mismatch model is used instead of exploiting directly the NEMD computer experiment results. The NEMD was used in [22] to study the temperature jump at a liquid–solid boundary. Based on these few studies, it is apparent that there is no general understanding of the Kapitza resistance as a function of the atomic parameters entering in the modeling of the materials.

This paper addresses the effects of an interface on the atomic vibrations in Lennard-Jones (LJ) solids, without or with a heat current flowing through the solid sample. Selection of the type of materials could limit, encourage or restrict the flow of thermal energy through a solid–solid interface. For example, the effect of compositional disorder on the lattice thermal conductivity (κ) of binary LJ solids was analyzed recently [23]. The present study expands that work by focusing on the thermal boundary resistance occurring at the interface between two LJ solids as a function of the ratio of atomic parameters of these solids (LJ parameters ϵ, σ and mass). This paper is organized as follows: section 2 describes the equilibrium (MD) and non-equilibrium molecular dynamics (NEMD) methodology used and the geometry of the binary LJ system. Section 3 addresses the effects of the solid–solid interfaces on the density of states of lattice vibrations. Results of the lattice thermal conductivity and the thermal boundary resistance as a function of the LJ parameters and mass are presented in section 4. The summary in section 5 concludes this paper.

2. Molecular dynamics approach: equilibrium and non-equilibrium

For all MD simulations a square-prism computational box elongated along the X axis is used with periodic boundary conditions in the two perpendicular directions Y and Z. Atoms within this computational box are initially located in face centered cubic (fcc) lattice sites and the number density is $\rho = 1.07$ at $T = 0.12$ and $\rho = 1.04$ at $T = 0.33$. Next, the computational box is divided in two equal-size elongated prisms. The dividing plane is located at $X = 0$ and each half-box is filled with atoms of either A or B type. An interface develops between these two systems. The interactions between atoms are of LJ type. Atoms on the positive X axis belong to the reference system and have LJ parameters ϵ_A (potential well), σ_A (hard core radius) and atomic mass m_A. Atoms on the negative X axis belong to a system that has either one LJ parameter (ϵ_B, σ_B) or mass (m_B) different from the corresponding parameter of the reference system. Parameters for the LJ interactions between atoms located on each side of the interface follow the combination rules: $\epsilon_{AB} = \sqrt{\epsilon_A \epsilon_B}$ and $\sigma_{AB} = (\sigma_A + \sigma_B)/2$. Typically the computational box contains 2000 atoms of both types located within a prism of size $5 \times 5 \times 20$ fcc unit cells (4 atoms/unit cell).

The orientation of the one-component crystal is set as [100] along the X direction in the computational box. For the two-component system, the [100] orientation is adopted for both components. For B atoms which have a σ parameter different from the A atoms the number of XY planes and XZ planes in the B region is chosen such that the cross section of the computational box containing B atoms is commensurate with the cross section of the prism containing A atoms. Quantities are expressed in reduced units with respect to parameters of the reference A atoms. Thus, units of mass, length, energy, time, temperature, frequency and thermal conductivity are m_A, σ_A, ϵ_A, $t_A = \sqrt{m_A \sigma_A^2/\epsilon_A}$, ϵ_A/k, t_A^{-1} and $k/(\sigma_A t_A)$, respectively (k is the Boltzmann constant). The time step in the molecular dynamic runs is $\Delta t = 0.005$. A radial cutoff of $3.8\sigma_A$ is adopted. When two different LJ systems are in contact, the following values of the parameter ratios are considered: (i) for the parameter ϵ, $R_\epsilon = \epsilon_B/\epsilon_A = 1.0$, 1.25, 1.5 and 2.0; (ii) for the parameter σ, $R_\sigma = \sigma_B/\sigma_A = 1.0$, 1.1 and 1.2 and (iii) for mass, $R_m = m_B/m_A = 1.0$, 1.6, 2.1 and 3.3.

Because the cross-section edges of the computational box are smaller than its length, effects of periodicity could be significant on dynamical properties. To make certain that our results do not contain unrealistic correlations such as correlation relaxation times τ_{relax} exceeding the time τ_{pbc} for spatial translations to become periodic, both of these times were closely monitored. For the monoatomic reference system at $T = 0.12$ and 0.33, calculation of these two times was repeated for various computational box cross sections showing that 5×5 fcc unit cell cross sections (100 atoms) yield a $\tau_{pbc} \approx 2.6 t_A$, which is longer than $\tau_{relax} \approx 0.2 t_A$. The τ_{relax} value is an average over ten different initial times of the velocity autocorrelation function. Thus, effects of the boundary conditions are negligible. All correlation functions used in this work were followed for $512\Delta t$ to avoid uncertainties that begin to increase rapidly for longer times [24, 25]. From the low frequency region of the velocity autocorrelation Fourier transform, an estimate of about 3 is obtained for the sonic velocity.

The non-equilibrium molecular dynamics set-up consists of a simulated thermostat attached at each end of the elongated computational box such that a temperature gradient would develop across the sample. Each thermal bath contains 200 atoms in fcc positions ($5 \times 5 \times 2$ unit cells) continuing

the computational box. Atoms in each thermal bath move according to a constant temperature MD in which their atomic velocities are scaled at every time step to ensure the temperature desired for that bath. Atoms in-between these two thermal bath regions move with iso-energy MD and data are collected only on these central atoms (typically 1400 atoms) located in the prism-shaped computational box. When a temperature drop exists between the two thermal baths, a thermal energy current is established along the prism and the system is neither in thermal equilibrium nor in a steady state. However, after a certain time the system reaches the steady state and the thermal energy current is constant along the length of the computational box in the direction of the energy flow. This NEMD arrangement has been used by other authors in calculations of the lattice thermal conductivity [11–14, 17, 15, 16, 18, 21, 22].

Steady state data of all studied properties are averaged over 100-atom subsets. Atoms in each subset are located in equal-sized regions sliced perpendicular to the computational box length. For the two-component systems (interface at $X = 0$), the type A atoms (reference) are located on the half-portion of the computational box adjacent to the hot thermal bath that contains A-type atoms only. The other half of the prism-shaped box contains atoms of type B, which are adjacent to the colder thermal bath built of B-type atoms only. As a result of the different dynamics between the atoms in the thermostat and the atoms in the active central region where data are taken, a few planes of atoms adjacent to the thermal baths were not considered in the reporting of results. A similar consideration was adopted by other authors [13, 14, 17, 16].

3. Effect of the interface on the lattice vibrations

The velocity autocorrelation function for N atoms is defined as

$$C(t) = \sum_{i=1}^{N} \langle \vec{v}_i(t) \cdot \vec{v}_i(0) \rangle \Big/ \sum_{i=1}^{N} \langle v_i^2(0) \rangle \qquad (1)$$

where v_i are the atom velocities. This $C(t)$ is calculated at different temperatures with iso-energy MD for the monoatomic systems and for the two-component systems containing an interface separating B atoms from the reference A atoms. Typical MD runs are $500\,000\Delta t$ long to reach equilibrium followed by $20\,000\Delta t$ used for building 30 $C(t)$ from sequential time segments. Each $C(t)$ has a length of $512\Delta t$. Two temperatures are investigated: $T = 0.12$ and 0.33. The density of vibrational states (DOS) is obtained from the Fourier transform of $C(t)$ [26]. The normalized DOS of the reference system containing A atoms is shown in figure 1 (solid line). When the LJ parameters are given the values in [27], the DOS in this work compares very well with the published results [26]. Therefore, the elongated shape of the computational box does not affect significantly the distribution of vibrational frequencies.

When the three variable parameters ϵ, σ, m have values different from the A-type atoms, the atomic vibrational frequencies change with respect to the reference system. Figure 1 shows the normalized DOS of systems entirely composed of B atoms with different values of the three variable parameters compared to the DOS of the reference system plotted as a solid line at $T = 0.12$ (figures 1(a)–(c)) and $T = 0.33$ (figures 1(d)–(f)). Figures 1(a) and (d) show the DOS for three values of ϵ_B with the ratio $R_\epsilon = 1.25$ (circles), 1.5 (squares) and 2.0 (triangles) while the other two parameters σ and mass are equal to the reference system ($R_\sigma = R_m = 1$). In the same manner, figures 1(b) and (e) show the DOS of a system in which $R_\sigma = 1.1$ (circles) and 1.2 (squares) and $R_\epsilon = R_m = 1$. Comparison of the reference system DOS with the DOS of a system in which $R_m = 1.6$ (circles), 2.1 (squares) and 3.3 (triangles) and $R_\epsilon = R_\sigma = 1$ is displayed in figures 1(c) and (f). It is evident from these results that there is a strong overlap between the DOS of the reference system (continuous line) and the DOS of systems with different

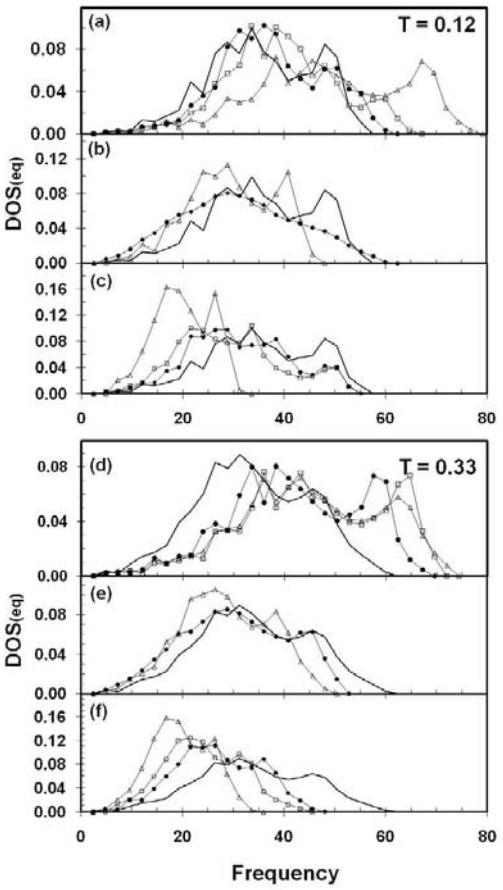

Figure 1. Normalized density of states (DOS) of one-component systems in thermal equilibrium for various LJ parameters. Solid line in all plots pertains to the reference system of A atoms. (a) $R_\epsilon = 1.2$ (●), 1.5 (□), 2.0 (△); (b) $R_\sigma = 1.1$ (●), 1.2 (△); (c) $R_m = 1.6$ (●), 2.1 (□), 3.3 (△).

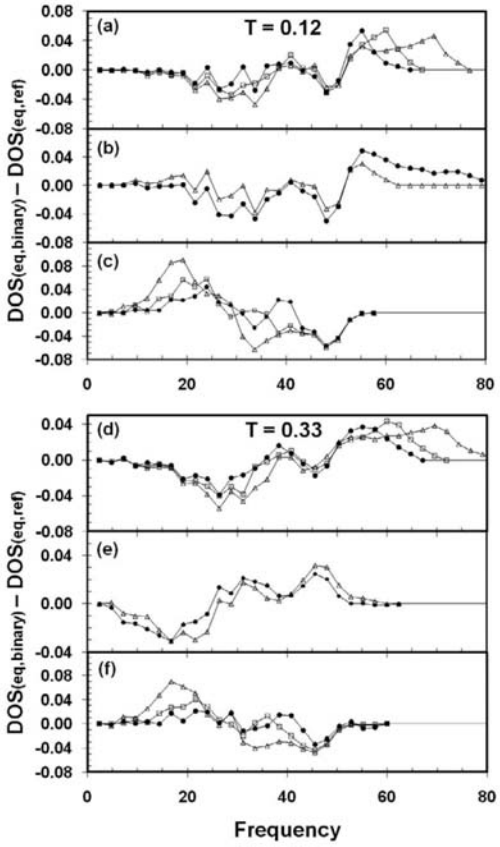

Figure 2. Normalized density of states (DOS) of binary systems in thermal equilibrium relative to the DOS of the one-component reference system for various LJ parameters. (a) $R_\epsilon = 1.2$ (●), 1.5 (□), 2.0 (△); (b) $R_\sigma = 1.1$ (●), 1.2 (△); (c) $R_m = 1.6$ (●), 2.1 (□), 3.3 (△).

parameters. It is to be noted that the DOS is shifted towards smaller frequencies as the mass is increased, which is expected. On the other hand, increases in ϵ and, to a lesser extent, σ with respect to the reference system tend to add high frequency vibrational modes to the DOS.

The presence of an interface affects the DOS. To study this effect, an interface is constructed in the middle of the elongated computational box, perpendicular to its length, by placing A atoms on one-half of the box and B atoms on the other half. Subsequently, this two-component system is equilibrated at two temperatures $T = 0.12$ and 0.33 and the DOS calculated at each of these two temperatures. Figure 2 shows the difference between the normalized DOS of the two-component system calculated for different types of B atoms and the normalized DOS of the reference system containing only A atoms. For interfaces due to changes in ϵ_B, figures 2(a) and (d) show an increase in the DOS of vibration modes at high frequencies

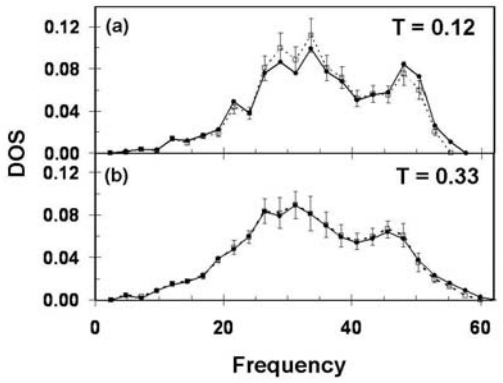

Figure 3. Non-equilibrium DOS of the monoatomic reference system of A atoms (□) compared to the DOS in equilibrium (●) at (a) $T_{avg} = 0.12$; (b) $T_{avg} = 0.33$.

(60–80) and a decrease at lower frequencies around 20–40, both of which persist at $T = 0.33$. The effect is about the same for all R_ϵ values. Interfaces due to the different σ_B shown in figures 2(b) and (e) display DOS changes similar to the changes in ϵ_B but now in different frequency regions. On the other hand, as shown in figures 2(c) and (f), the effect of mass changes produces a depletion of modes in the DOS in the range $30 \leqslant \omega \leqslant 50$ and an increase of mode density in the lower frequency region $10 \leqslant \omega \leqslant 30$. The mass effect is more acute the larger R_m becomes, in agreement with previous findings [11]. In all cases the effect of the interface is identified by DOS changes above and below a characteristic frequency of $\omega_c \approx 30$.

The DOS is also affected when the system is not in thermal equilibrium. To study this effect the reference system composed of only A atoms is connected to the hot and cold thermal baths such that the NEMD set-up allows for the system to reach a steady state after $500\,000\Delta t$. The subsequent $11\,000\Delta t$ are used for production. In the steady state of heat transfer, a temperature gradient develops along the length of the computational box. The temperature at the center of the box is the system average temperature. For this non-equilibrium (NE) system, 16 $C(t)$ of length $512\Delta t$ were sequentially constructed from the production results and the DOS obtained from their Fourier transforms. Figure 3 shows the reference system normalized DOS in thermal equilibrium (filled circles) compared with the non-equilibrium (empty squares) situation at two average temperatures $T = 0.12$ and 0.33. Error bars identify the standard deviation of the sample of 16 correlation functions. It is clearly seen that at the higher temperature the DOS displays marginal changes when the system is in NE. However, at the lower temperature the DOS of the NE system is slightly enhanced around $\omega = 30$. For the binary systems with an interface, figure 4 shows the differences between their NE DOS and the equilibrium DOS. In systems with ϵ and mass changes and at the lower temperature ($T = 0.12$) there is a modest increase of the DOS at frequencies around 30 and a small decrease around 50–60 due to the heat flow. At

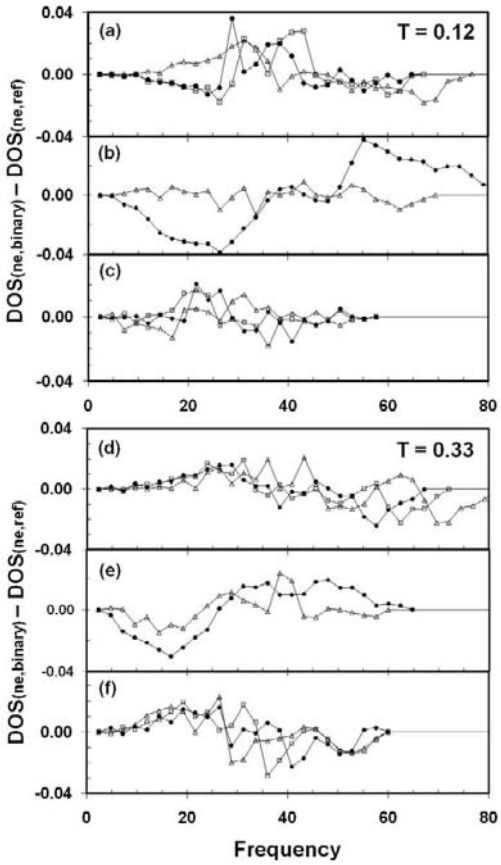

Figure 4. Non-equilibrium DOS of binary systems relative to their DOS in thermal equilibrium for various LJ parameters. (a) $R_\epsilon = 1.2$ (●), 1.5 (□), 2.0 (△); (b) $R_\sigma = 1.1$ (●), 1.2 (×); (c) $R_m = 1.6$ (●), 2.1 (□), 3.3 (△).

$T = 0.33$, the DOS is enhanced in a broader range at the lower frequencies and depleted at higher frequencies for all binary systems involving atoms with two values of the parameter ϵ or the mass. However, two-component systems with different σ (figure 4(b)) display an enhancement of the NE DOS at higher frequencies and a depletion at low frequencies. This effect tends to disappear at higher temperatures.

Summarizing, at $T = 0.12$ the overall effect of a two-atom type interface in equilibrium is to modestly enhance the DOS at frequencies above ω_c and deplete it below this characteristic frequency for R_ϵ, $R_\sigma > 1$ whereas the opposite behavior is demonstrated for $R_m > 1$. When these two-component systems are not in thermal equilibrium, at $T = 0.12$ the trend is an enhancement of the DOS below the ω_c region for systems with different ϵ or mass. This is indicative that the heat flow enhances scattering of the transverse frequency phonons. These trends are smeared out at a higher temperature. On the other hand, interfaces built with atoms that have different σ values display a reverse behavior where the DOS is depleted of modes at frequencies below ω_c and enhanced above it.

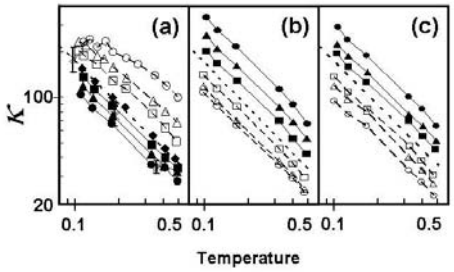

Figure 5. Thermal conductivity as a function of temperature. Solid diamonds pertain to the reference LJ system and dotted line (in (a)–(c)) is the best fit to these values. Crosses and standard deviation are from [23]. (a) $R_\epsilon = 0.7$ (●), 0.8 (▲), 0.9 (■), 1.25 (□), 1.5 (△) and 2.0 (○). Stars and standard deviations are from [23]; (b) $R_\sigma = 0.7$ (●), 0.8 (▲), 0.9 (■), 1.1 (□), 1.2 (△) and 1.25 (○); (c) $R_m = 0.3$ (●), 0.5 (▲), 0.7 (■), 1.6 (□), 2.1 (△) and 3.3 (○).

4. Lattice thermal conductivity and thermal boundary resistance

In the NE situation, a temperature gradient $\vec{\nabla}T$ sets in due to the flow of energy across the computational box. Once the system reaches a steady state, the Fourier law of heat conduction is valid such that

$$\vec{J} = -\kappa\vec{\nabla}T \tag{2}$$

where $\vec{J}$ is the heat current and κ is the lattice thermal conductivity [15, 16]. An atomistic inspection is obtained when $\vec{J}$ is obtained from atomic quantities [28]:

$$\vec{J} = \frac{1}{V}\sum_{i=1}^{N} E_i\vec{v}_i + \frac{1}{2V}\sum_{i=1}^{N}\sum_{j\neq i}^{N}(\vec{v}_i\cdot\vec{F}_{ij})\vec{r}_{ij} \tag{3}$$

where E_i is the total energy of each atom, $\vec{v}_i$ is the velocity of each atom, $\vec{F}_{ij}$ and $\vec{r}_{ij}$ are the forces and interatomic distance vectors between each pair of atoms and V is the volume. Both $\vec{J}$ and $\vec{\nabla}T$ can be calculated in the NEMD set-up described in section 2 and the lattice thermal conductivity κ is then obtained from equation (2). With this geometrical set-up, the heat current components perpendicular to the energy flow should be negligible. Indeed, that is the case in our calculation. The temperature difference between the two thermal baths was chosen to be large with respect to the temperature fluctuations but small enough to reproduce attainable laboratory situations. In our simulations the cold bath temperature is typically about 60% of the hot bath temperature. This choice is similar to the 65%–70% employed in other works [13, 14, 19]. Figure 5 shows the thermal conductivity as a function of temperature for one-component systems with different values of the parameters ϵ, σ and mass. Six different masses and LJ parameters were considered: (i) $R_\epsilon = 0.7$, 0.8, 0.9, 1.25, 1.5 and 2.0

(figure 5(a)); (ii) $R_\sigma = 0.7$, 0.8, 0.9, 1.1, 1.2 and 1.25 (figure 5(b)) and (iii) $R_m = 0.3$, 0.5, 0.7, 1.6, 2.1 and 3.3 (figure 5(c)). In all cases the dotted line corresponds to the reference system $R_\epsilon = R_\sigma = R_m = 1$. Standard deviations are shown on the figure; however, their values of about 3%–7% of the average value are within the size of the symbols. The parameter dependence of κ compares well with our previous work within the Green–Kubo (GK) approach [23]. This alternative method for calculating κ yields large standard deviations at low temperatures, pointing out one of the disadvantages of the GK versus the NEMD approach. The expected inverse temperature relationship for crystalline systems is clearly shown by the log–log plot of figure 5. This can be exploited to interpolate between different LJ systems, as also suggested by other authors [4, 5, 16, 18, 21, 22]. Based on our results such an interpolation yields a power law relationship for each varied parameter (ϵ, σ, mass): $R_\epsilon^{3/2}$, R_σ^{-2} and $R_m^{-1/2}$.

It is well known that solid–solid and liquid–solid interfaces act as a resistance to the heat flow perpendicular to them and give rise to the Kapitza resistance (Ω_K). This effect is measurable because of the discontinuity in the temperature profile occurring at the interface. Such temperature discontinuity is quite distinct across an interface built with two types of atoms and is detectable even for 1D systems where atoms are linked harmonically [4]. Our calculation focuses on Ω_K of binary LJ solid–solid interfaces as a function of ϵ, σ and atomic mass. Figure 6 shows a typical temperature profile at $T = 0.3(R_m = 3.3, R_\epsilon = R_\sigma = 1)$ where the temperature discontinuity at the interface $\Delta T_{\text{interface}}$ is clearly seen. Following [16], Ω_K is calculated as

$$\frac{1}{\Omega_K} = \kappa_0 \frac{\nabla T}{\Delta T_{\text{interface}}} \tag{4}$$

where κ_0 is the bulk thermal conductivity. However, since we know the κ on each side of the solid–solid interface, the atomistic approach for calculating Ω_K is to use the actual κ and ∇T values for the LJ crystal on each side of the interface. In fact, a thermal current sees the interface as two resistances in series because the heat current must be the same on both sides of the interface if no additional energy sources or sinks exist. It follows that

$$\Omega_K = \Delta T_{\text{interface}} \left(\frac{1}{\kappa_A \nabla T_A} + \frac{1}{\kappa_B \nabla T_B} \right) \tag{5}$$

where $\kappa_{A,B}$ and $\nabla T_{A,B}$ are the thermal conductivity and temperature gradient of the LJ systems A and B that meet at the interface. Figure 7 shows the dependence of the temperature jump $\Delta T_{\text{interface}}$ at the interface and the resulting Ω_K of the two-component systems for various temperatures and parameter ratios. It is observed that, as the parameter ratio moves away from the 1:1 ratio (no interface), the temperature discontinuity and the Ω_K become more pronounced. Additionally, as the average temperature in the system is increased, the interface temperature discontinuity and the Kapitza resistance are less pronounced. It can also be seen that the Ω_K increases at about the same rate with changes of R_ϵ, R_σ, or R_m. In general,

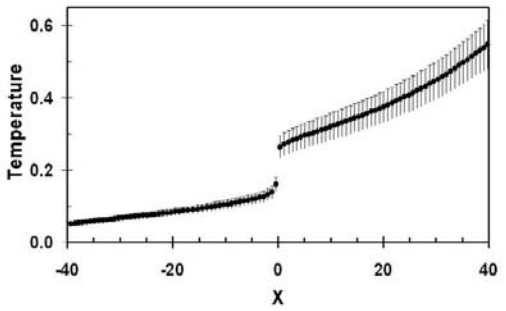

Figure 6. Temperature profile of the NE LJ system with interface at $X = 0$ and $R_m = 3.3$ at average temperature $T = 0.33$. Error bars are the standard deviation of the NEMD run.

the building up of this thermal resistance is assigned to an increased reflectance of phonons by the interface [3, 21]. As discussed in section 3 and shown in figure 2, our equilibrium MD simulation shows that the interface increases the DOS of vibrational states in the region of high frequencies for two-component systems with different ϵ or σ but for systems with different masses the increase occurs at lower frequencies. Based on these results, it immediately follows that two-component systems with different ϵ or σ should display larger Ω_K than the case with different masses at the same temperature. Illustrated in figure 7 is a confirmation of this result. However, in the non-equilibrium situation, when the system reaches the steady state, the DOS of vibrational states is significantly populated in the region of ω_c only for systems with different ϵ and mass, as shown in figure 4. Based on this result, it is then expected that the $\Delta T_{\text{interface}}$ for two-component systems with different ϵ and mass would be larger than for systems with different σ, as is shown in figure 7. Increasing the temperature should reduce the Kapitza resistance and the temperature jump at the interface should be decreased. Our results confirm both effects.

An additional characteristic quantity of interfaces is the Kapitza length $l_K = \kappa \Omega_K$ associated with the effective thickness of material involved in the interface [1, 22]. It has been theorized [22] that, when κ is large, l_K will be large and the effect may be observed but no data were provided for supporting this ansatz. In the example of figure 6, values of κ and Ω_K are 32 and 0.3, respectively, yielding an l_K of about 9. This example was studied for several lengths of the computational prism to determine their eventual effect on l_K. The Ω_K calculated for prism-shaped computational boxes with lengths of 42.3, 73.7, 105 and 136.4 were all within the standard deviation of 11.4%, indicating that this property is basically insensitive to the length of the computational prism and the temperature jump at the interface is observed in all cases. From our results summarized in figures 5 and 7, we predict that l_K varies as $1/T^2$.

We also studied the effect on κ and Ω_K due to changes in the orientation of the crystals on each side of the interface. First, it was determined that one-component systems did not

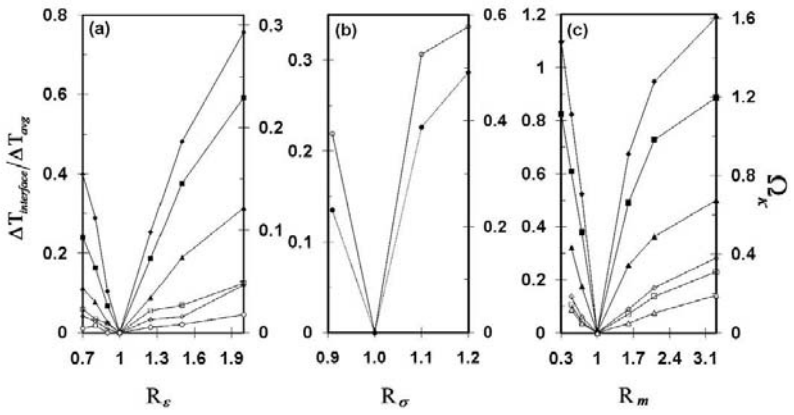

Figure 7. Temperature drop at the interface and Kapitza resistance as a function of system parameters at various temperatures 0.10 (♦), 0.125 (■), 0.165 (▲), 0.33 (□), 0.425 (◇) and 0.5 (○). Temperate drops are plotted relative to the temperature difference between the hot and cold thermal baths.

give rise to a discontinuity in the temperature at the interface when the interface was created by rotating atoms in half of the box to Miller indices [110], [111], [120], [121] and [122] while keeping atoms in the other half of the box at [100] (reference system). Second, the κ for these rotated systems is within the standard deviation of values reported in figure 5. Third, in the case of two-component systems in which the A system is in the [100] orientation and the B system is rotated and its parameters change, the results for the temperature jump and the Ω_K are within 3%–9% of values reported in figure 7. Based on these calculations, we conclude that the relative orientation of the crystal planes meeting at the interface do not affect the thermal properties.

5. Conclusions

In this work we have quantitatively demonstrated the influence of a two-atom type interface between two LJ solid systems on the density of vibrational states as a function of the atomic mass and LJ parameters. A characteristic frequency of $\omega_c = 30$ is predicted below which the DOS is depleted and enhanced above it for R_ε, $R_\sigma > 1$ while the opposite behavior is demonstrated for $R_m > 1$. However, when a thermal energy flow is established the DOS is enhanced below ω_c and depleted above it for the cases R_ε, $R_m > 1$. This is indicative that the heat flow enhances scattering of the transverse frequency phonons only in these two cases. At higher temperatures these effects are less visible.

The NEMD computer experiment of two-component LJ systems sharing an interface leads to very clear observations that allow for identification of the thermal boundary resistance and its dependence on the LJ parameters and atomic mass. Both the Kapitza resistance and the temperature discontinuity at the interface increase as the parameter ratio between properties of the targeted material to the reference material moves away from the value of one. Additionally, both the Kapitza resistance and the interface temperature discontinuity increase with decreasing temperature. We predict that the Kapitza length increases as $1/T^2$ as the temperature is decreased and is independent of the size of the computational box. The relationships contained in this paper may serve as a reference for scientists and engineers in search of novel combinations of materials in problems related to thermal management at the nanoscale.

Acknowledgments

This work was supported in part by the National Science Foundation, grant CHE-0626111. We acknowledge the Supercomputing Center of the College of Science of George Mason University for the computer time and facilities allocated to this project.

References

[1] Kapitza P L 1941 *J. Phys.* **4** 181
[2] Khalatnikov I M 1952 *J. Exp. Theor. Phys.* **22** 687
[3] Swartz E T and Pohl R O 1989 *Rev. Mod. Phys.* **61** 605
[4] Lumpkin M E, Saslow W M and Visscher W M 1978 *Phys. Rev.* B **17** 4295
[5] Schelling P K, Phillpot S P and Keblinski P 2004 *J. Appl. Phys.* **95** 6082
[6] Liang X-G and Shi B 2000 *Mater. Sci. Eng.* A **292** 198
[7] Young D A, Thomsen C, Grahn H T, Maris H J and Tauc J 1986 *Phonon Scattering in Condensed Matter* (Berlin: Springer) p 49
[8] Stoner R J and Maris H J 1993 *Phys. Rev.* B **48** 16373
[9] Chen G, Tien C L, Wu X and Smith J S 1994 *J. Heat Transfer* **116** 325
[10] Matsumoto M, Wakabayashi H and Makino T 2005 *Heat Transfer Asian Res.* **34** 135
[11] Liang X-G and Sun L 2005 *Micros. Thermophys. Eng.* **9** 295
[12] Nishiguchi N and Sakuma T 1990 *J. Phys.: Condens. Matter* **2** 7575

[13] Lukes J R, Li D Y, Liang X G and Tien C L 2000 *Trans. ASME* C **122** 536
[14] Imamura K, Tanaka Y, Nishiguchi N and Maris H J 2003 *J. Phys.: Condens. Matter* **15** 8679
[15] Phillpot S R, Schelling P K and Keblinski P 2005 *J. Mater. Sci.* **40** 3143
[16] Maiti A, Mahan G D and Pantelides S T 1997 *Solid State Commun.* **102** 517
[17] Mountain R D and MacDonald R A 1983 *Phys. Rev.* B **28** 3022
[18] Twu C-J and Ho J-R 2002 *Phys. Rev.* B **67** 205422
[19] Chantrenne P and Barrat J L 2004 *J. Heat Transfer* **126** 577
[20] Amrit J 2006 *J. Phys. D: Appl. Phys.* **39** 4472
[21] Stevens R J, Zhigilei L V and Norris P M 2007 *Int. J. Heat Mass Transfer* **50** 3977
[22] Barrat J L and Chiaruttini F 2003 *Mol. Phys.* **101** 1605
[23] Lyver J W and Blaisten-Barojas E 2006 *Acta Mater.* **54** 4633
[24] Alder B J and van Thiel M 1963 *Phys. Lett.* **7** 317
[25] Zwanzig R and Ailawadi N K 1969 *Phys. Rev.* **182** 280
[26] Dickey J M and Paskin A 1969 *Phys. Rev.* **188–3** 1407
[27] Grindley J and Howard R 1965 *Lattice Dynamics* ed R F Wallis (New York: Pergamon) p 129
[28] Balescu R 1990 *Equilibrium and Non-Equilibrium Statistical Mechanics* (New York: Wiley) chapter 12

A.3 Prepublished Paper [11] (Submitted: June 2010 to Computational and Theoretical Nanoscience)

Lattice Thermal Conductivity in Nanotubes, Nanowires and Nanofilaments: a Molecular Dynamics Study

John W. Lyver, IV [1,2] and Estela Blaisten-Barojas[1*]

[1]Computational Materials Science Center and Department of Computational and Data Sciences, George Mason University, MS 6A2, Fairfax, VA 22030, USA

[2]Office of Safety and Mission Assurance, National Aeronautics and Space Administration, Washington, DC 20546, USA

*blaisten@gmu.edu

Abstract

This paper presents results a non-equilibrium Molecular Dynamics approach to determine the lattice thermal conductivity of nanowires, nanotubes, and nanofilaments of silicon carbide. The nanostructures are modeled with the classical potential proposed in J. Appl. Phys., **101**, 103515 (2007). These nanostructures display very low lattice thermal conductivity, about 50 times smaller than bulk SiC. Among the studied nanostructures, the 3C [$\bar{1}$00] nanowires have the highest thermal conductivity, and the (5,5) nanotubes display the lowest. Dependence on temperature of the lattice thermal conductivity exhibits an inverse power relationship only for nanowires 3C [$\bar{1}$00], 2H [110] and the (4,0), (2,2) nanotubes. All other structures have thermal conductivities decreasing more gently as a function of increasing temperature, except for nanowires 3C and nanotubes (5,5)where the thermal conductivity is almost constant as a function of temperature.

Keywords: thermal conductivity, non-equilibrium molecular dynamics, silicon carbide, SiC nanowires, SiC nanotubes, SiC nanofilaments

1. Introduction.

Nanostructures began to emerge in the mid-1980s as building blocks useful to assemble larger materials and design special macromolecular constructs with novel mechanical and thermal characteristics. Today, nanodevices have emerged as fundamental for achieving improved mechanical, thermal, and electronic controls. Among other properties, the thermal conductivity of the device may be critical to the control function and the stability of the macro-system itself [1]. One postulated application of nanodevices is to act as heat conduits/sinks or field emitting units [2]. An important question is to whether these nanodevices are good or bad heat conductors and at the same time they remain stable at operational temperatures. Silicon carbide (SiC) is a broadly used material in nanoelectronics and has proven to sustain a variety of stable nanostructures [2-4]. SiC nanotubes and nanowires have been fabricated experimentally [2,4], and a multitude of hollow fullerene-like clusters have been predicted which could be useful in building nanodevices [3].

Carbon and silicon are both group-IV elements that exhibit sp^2 and sp^3 bonds. These bonds

cause bulk SiC to be among the hardest materials and to be well suited for devices being operated in extreme environments [5]. In fact, bulk SiC has a wide band gap [6], high thermal conductivity [7], and is resistant to various forms of radiation [8]. It has been postulated that the use of SiC in nanostructures and nanodevices should exhibit equivalent characteristics [3]. Although experimental advances are seen every day, it is still difficult to perform measurements of thermal properties at the nanometer scale. Therefore, computational simulations are useful for adding understanding of properties and mechanisms in systems at the nano-scale. A number of non-equilibrium molecular dynamics (NEMD) studies for the determination of thermal properties in non-homogeneous systems have been published [9-15]. For example, NEMD was used for obtaining the lattice thermal conductivity by simulating the directional heat flow perpendicular to infinite thin films in one-, two-, or three-dimensional Lennard-Jones systems [9,11,16]. However, little has been investigated for thermal characteristics of SiC nanostructures, although a good number of atomistic simulations addressing thermal properties of SiC are available [17-22]. Atomistic simulations of energetic stability and mechanical deformations of SiC nanowires and nanotubes [23-25] have been put forward using the Tersoff potential [26]. Electronic structure studies of SiC nanocages, nanotubes, and nanowires have been published, both within density functional theory [3,27] and tight binding [28] approaches. Studies of thermal conductivity of SiC nano-guides using the Tersoff potential have predicted a strong degradation of the thermal conduction ability [29]. A study of thermal transport in SiC nanotubes within the Green-Kubo approach for calculating the thermal conductivity has been put forward [30]. However, this approach is adequate for homogeneous, isotroptic systems, which is not the case in nanotubes.

This work addresses the determination of the lattice thermal conductivity of four types of SiC nanowires, and a variety of nanotubes with zigzag and armchair chiralities and different diameters. The approach is based on NEMD employing a potential proposed in Ref. [20]. The work builds on our previous NEMD implementation [16] in which we examined thermal properties of thin films due to interfaces between two different LJ films. Additionally, nanowires and nanotubes stable configurations obtained in previous work [28] are used as starting points for the atomistic simulations. This paper is organized as follows: section 2 describes the combination of equilibrium molecular dynamics (MD) and NEMD approaches used for the numerical determination of the lattice thermal conductivity. Section 3 addresses the determination of the lattice thermal conductivity in the different nanostructures and presents our results for nanowires, nanotubes and nanofilaments. The summary in section 4 concludes this paper.

2. Molecular Dynamics Approach: Equilibrium and Non-equilibrium

To simulate the interaction between atoms in SiC, the model potential proposed by Vashishta, et al. is used throughout [20,21]. This model potential includes two-body charge multipole interactions as well as three body terms describing the covalent bond bending/stretching with a version of the Stillinger-Weber potential [31]. Thus, the total potential of the system is given by

$$U = \sum_{i<j}^{n} U^{(2)}(r_{ij}) + \sum_{i,j<k}^{n} U^{(3)}(r_{ij}, r_{ik}) \qquad (1)$$

Here, n is the total number of atoms, $U^{(2)}$ is the 2-body term given by

$$U^{(2)}(r_{ij}) = \frac{H_{ij}}{r_{ij}^{\eta_{ij}}} + \frac{Z_i Z_j}{r_{ij}} e^{-r/\lambda} - \frac{D_{ij}}{2r_{ij}^4} e^{-r/\xi} - \frac{W_{ij}}{r_{ij}^6} \quad (2)$$

where r_{ij} is the distance between toms i and j, H_{ij} is the strength of the steric repulsion of

23.67291 eVÅ for Si-Si, 447.09026 eVÅ for Si-C, and 471.74538 eVÅ for C-C interactions, Z_i is the effective charge of +1.201 e for Si and -1.201 for C, D_{ij} is the strength of the charge-dipole attraction of 2.1636 e^2Å^3 for Si-Si, 1.0818 e^2Å^3 for Si-C, and zero for C-C interactions, W_{ij} is the van der Waals strength of zero for Si-Si and C-C, and 61.4694 eVÅ^6 for Si-C interactions, η_{ij} is the exponent of the steric repulsion term of 7 for Si-Si and C-C, and 9 for Si-C interactions, λ and ξ are screening lengths of 5.0 Å and 3.0 Å, respectively.

The 3-body term $U^{(3)}$ in Eq. 1 is given by

$$U^{(3)}(r_{ij}, r_{ik}) = R^{(3)}(r_{ij}, r_{ik})\, P^{(3)}(\Theta_{jik}) \qquad (3)$$

where $R^{(3)}$ is the bond-stretching interaction and $P^{(3)}$ is the bond bending potential. The contribution $R^{(3)}$ is defined as

$$R^{(3)}(r_{ij}, r_{ik}) = B_{jik} exp\left(\frac{\gamma}{r_{ij}-r_o} + \frac{\gamma}{r_{jk}-r_o}\right)\delta(r) \qquad (4)$$

where, B_{jik} is the interaction strength of 9.003 eV, γ is a unit conversion of 1Å, and $\delta(r)$ is a step function cutting the force when distances between the i-j or j-k atoms are larger than 7.35 Å. The bond bending potential is defined as

$$P^{(3)}(\Theta_{jik}) = \frac{\left(cos(\Theta_{jik}) - cos(\bar{\Theta})\right)^2}{1 + C_{jik}\left(cos(\Theta_{jik}) - cos(\bar{\Theta})\right)^2} \qquad (5)$$

where Θ_{jik} is the bond angle between j-i-k atoms, $\bar{\Theta}$ is the reference angle of 109.47^o and C_{jik} = 5.0. Even though the interior angles in a hexagon are 120°, the 109.47° is the relaxed angle for a Si-C-Si or C-Si-C bonds [19-21].

For all MD simulations elongated SiC tubes, filaments, and wires are laid along the X-axis. No periodic boundary conditions are used. Our initial configurations are nanowires obtained from cuts of the 3C and 2H crystalline polytypes, and nanotubes with either armchair or zigzag chirality. These initial configurations are consistent with optimized and stable geometries optimized under the tight-binding approximation [28]. The alternation of Si and C atoms in these systems is such that bonds of around 1.9 Å [3,20,21,27,28] are the dominant majority.

The first stage of our simulations is the determination of wires and tubes stability under the model potential. This is achieved by equilibrating with constant energy MD the open-end wire or tube systems at various temperatures. Runs to equilibrate the systems are performed for about a half million time steps of $\Delta t = 0.3 \times 10^{-15}$ sec.

The NEMD stage is achieved through a setup consisting of a simulated thermostat attached at each end of the elongated tube or wire that has been equilibrated at a desired temperature. As depicted in figure 1, each thermostat is a continuation of the tube or wire containing about 100-150 atoms that are kept at a constant temperature. One thermostat is kept at relatively high temperature and the other thermostat is kept at lower temperature such that a temperature

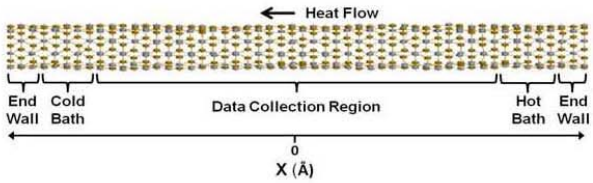

Figure 1. Computational setup for the non-equilibrium molecular dynamics simulations.

gradient would develop across the tube or wire. The thermal baths are sized such that their length along the X-axis is greater than 7.35 Å, the cutoff radius of the 2-body part of the model potential. Atoms in each thermal bath are kept at a desired constant temperature by scaling their velocities at every time step. On the outside ends of the bath, three-to-four planes of atoms are kept fixed in position to prevent deformations of the cross sections of the nanostructures. Atoms in the

region between the two thermal baths move according to iso-energy MD and data are collected only on these central atoms (typically 320 to384 atoms).

When a temperature drop exists between the two thermal baths, a thermal energy flow is established along the elongated tube or wire and the system is neither in thermal equilibrium nor in a steady state. However, after about 200 picoseconds the system reaches the steady state and the thermal energy current is roughly constant along the length of the nanosystem. This NEMD arrangement has been adopted in other lattice thermal conductivity calculations [9-15,29]. However, in our case there are no periodic boundary conditions in any direction as in such works.

3. Lattice Thermal Conductivity of SiC Nanostructures.

Because a temperature gradient sets in once the system reaches a steady state, the Fourier law of heat conduction is applicable, such that:

$$\vec{J} = -\kappa / \vec{\nabla}_T \qquad (6)$$

where $\vec{J}$ is the heat current per unit volume and κ is the lattice thermal conductivity [8,10]. Atomistic inspection of $\vec{J}$ is obtained from [32]:

$$\vec{J} = \frac{1}{V}\sum_{i=1}^{n} E_i \vec{v}_i + \frac{1}{2V}\sum_{i=1}^{n}\sum_{i=1}^{n}\left(\vec{v}_i \cdot \vec{F}_{ij}\right)\vec{r}_{ij} \qquad (7)$$

where E_i is the total energy of each atom, $\vec{v}_i$ is the velocity of each atom, $\vec{F}_{ij}$ and $\vec{r}_{ij}$ are the forces and interatomic distance vectors between each pair of atoms, and V is the volume.

For the non-equilibrium analysis, the data collection section of each wire or tube shown in figure 1 is subdivided in slices along its length. Each slice contains typically 40 to 48-atoms. The purpose of these sub-regions is the ability to average properties locally within each slice. Simulations are started for the equilibrated configuration of all systems. Once the temperature difference between the two thermostats is established, there is a transient time in which the average thermal current (Eq. 7) in each slice is not constant. Similarly, during this transient time, the temperature profile across the length of the system (built from local averages in each slice) is not linear. However, once the steady state of thermal energy conduction is reached, then the thermal current is approximately the same in all slices, and the temperature profile is remarkably linear. A typical case is shown in Figure 2 illustrating both temperature and thermal current profiles across the length of a 3C nanowire at an average temperature of ~300 K. Points in this figure correspond to averages for each slice over 6 ps after the steady state is reached. As a result of the different dynamics between the atoms in the thermostat and the atoms in the active central region where data are taken, a few planes of atoms adjacent to the thermal baths were not considered for reporting of results in the sections to follow. A similar consideration has been adopted in the literature by several authors [11,12,16].

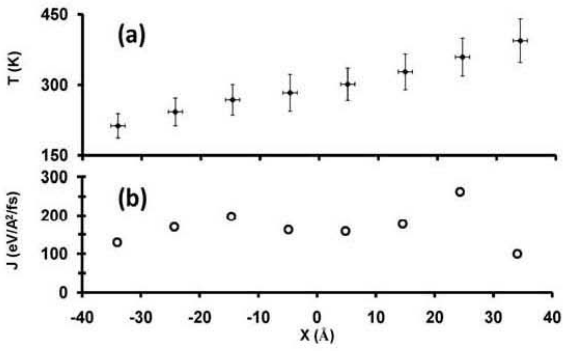

Figure 2. Temperature and heat current across the device. (a) Temperature profile. Error bars identify standard deviations (s.d.). (b) Heat current at an average temperature of ~300K.

With this geometrical setup, the heat current components perpendicular to the energy flow should be negligible. Indeed, that is the case in our calculation where the perpendicular flow is around 1% of the flow along the length of the nanostructure. Additionally, it is confirmed that the longer data are averaged, the smaller the perpendicular flow becomes. The temperature difference between the two thermal baths is chosen to be large with respect to the temperature fluctuations but small enough to reproduce attainable laboratory situations. In our simulations the cold bath temperature is about 40% of the hot bath temperature. This choice is similar to that employed in other works [11,16,29].

Both $\vec{J}$ and T are calculated within the NEMD approach described in the previous section and then the lattice thermal conductivity κ is obtained from Eq. (6). The objective is to find κ at five temperatures: 150 K, 300 K, 500 K, 750 K, and 1000 K.

3.1 Nanowires

Nanowire configurations are obtained by carving the zinc-blende 3C and the wurzite 2H crystalline polytypes of SiC along the [$\bar{1}$00], [$\bar{1}$11] and [001], [110] directions, respectively. These elongated cuts have been demonstrated to be stable [28] and are shown in figure 3. During the MD equilibration process these four nanowires are extremely stable throughout the runs at all temperatures in the range 150 K – 1000 K. Indeed, these wires kept their structure up to temperatures of 1000K. The equilibrium MD average potential energies per SiC pair, extrapolated to zero temperature, have values of -11.75 eV, -11.46 eV for 3C [$\bar{1}$00], [$\bar{1}$11] and -11.98 eV, -11.43 eV for 2H [100], [110] nanowires. These results match qualitatively the tight binding energies per SiC pair of -11.7 eV, -11.0 eV for 3C [$\bar{1}$00], [$\bar{1}$11], and -11.6 eV, -10.3 eV for 2H [001], [110] nanowires calculated in Ref. [28].

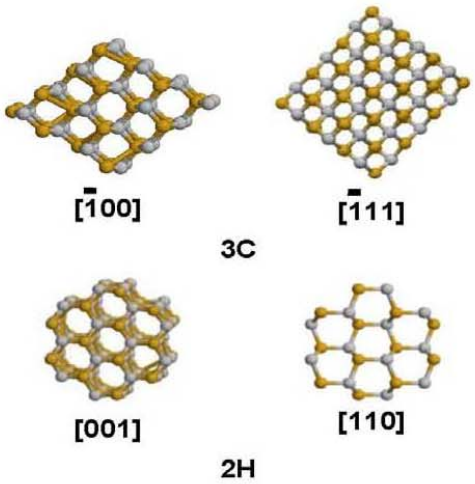

Figure 3. Cross sections of the SiC nanowires cut from the zinc-blende 3C and the wurzite 2H polytypes.

The MD equilibrated configurations of these four nanowires were taken as initial configurations for the NEMD calculation of the lattice thermal conductivity κ. The results of κ as a function of temperature are shown in figure 4. The 3C [$\bar{1}$00] nanowire has the highest thermal conductivity, which is expected since this is the most stable wire among those studied here. The almost constant κ obtained for 2H [001] and 3C [$\bar{1}$11] wires are close to predictions in Ref. [29]. Although the 3C [$\bar{1}$00] and 2H [110] wires, present the expected T^{-1} power law decrease as a function of temperature, our resuls predict thermal conductivities two orders of magnitude lower than in bulk SiC measurements [7,18]. In conclusion, nanowires are poor heat conductors, a property that can be used in a variety of nanodevices.

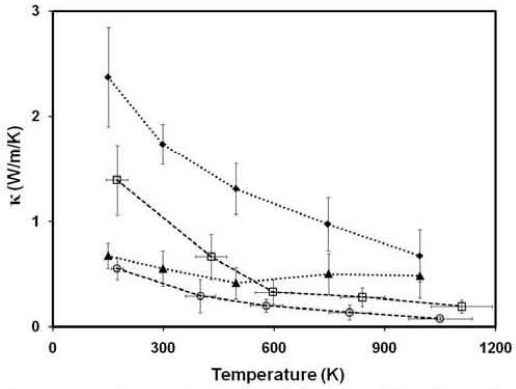

Figure 4. Thermal conductivity as a function of temperature for nanowires: 3C [$\bar{1}$00] (♦), 3C [$\bar{1}$11] (▲), 2H [001] (○), 2H [110] (□). Error bars identify s.d.

3.2 Armchair Nanotubes

Simulations are done on nanotubes with armchair chirality, as shown in figure 5. Four armchair nanotube diameters are considered: (2,2), (3,3), (4,4), and (5,5). When the MD equilibration process is done on these nanotubes, not all nanotubes maintain their initial shape. The armchair (2,2) and (5,5) nanotubes are structurally stable under the model potential and remain in a tubular shape throughout the simulation at all temperatures in the range 150 - 1000 K. However, the (3,3) and (4,4) nanotubes collapse into flatten structures which we refer to as nanofilaments F33 and F44. Moreover, these new structures remain stable and equilibrate well at the considered temperatures. Figure 5 shows the resulting stable nanofilament structures. The average potential energy per SiC pair extrapolated to zero temperature is -11.4 eV for both the (2,2) and (5,5) nanotubes and -11.5 eV, -11.63 eV for the collapsed (3,3), (4,4) tubes. The potential energies of both nanotubes are in qualitative agreement with the tight binding results of 10.0 eV, 10.5 eV [28] and are close to those calculated with MD in Ref. [24]. In both the (2,2) and (5,5) single wall nanotubes, the carbon atoms are slightly pushed toward the outside of the tube surface and the silicon atoms toward the inside. The puckering is about 0.1 Å and decreases as temperature increases.

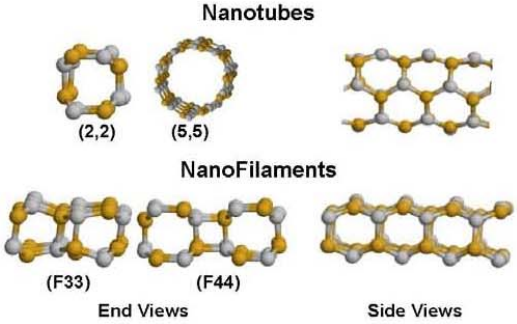

Figure 5. Structure of SiC armchair nanotubes (2,2) and (5,5) and filaments F33 and F44.

The dependence of κ with temperature for these armchair tubes and filaments is shown in Figure 6. The temperature dependence of κ for tube (2,2) follows a power law $\kappa \sim T^{-1}$. In contrast, tube (5,5) presents an almost constant κ as a function of temperature. This prediction is discrepant with results in Ref. [30] where the Green-Kubo (GK) approach was used. We note that the GK is appropriate for isotropic systems, and thus is not adequate for structures such as tubes. The power law relationship of κ for the nanofilaments is $\kappa \sim T^{-0.65}$ indicating a more gentle decrease with increasing temperature. The fluctuations for these tube/filament systems are quite large, as is visually seen in Fig. 6. For clarity, only the positive standard ddeviation (s.d.) is depicted in the figure.

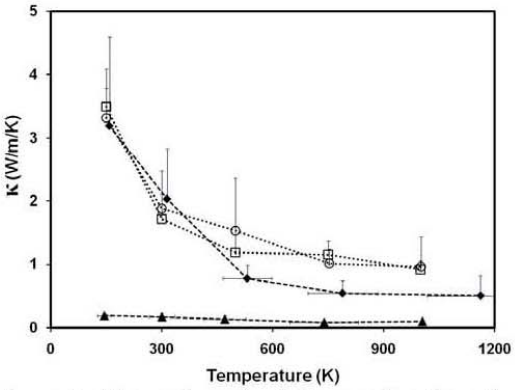

Figure 6. Thermal conductivity as a function of temperature for armchair nanotubes and nanofilaments: (2,2) (♦), (5,5) (▲) nanotubes, and F33 (□), F44 (○) nanofilaments. Error bars identify s.d.

3.3 Zigzag nanotubes

The zigzag nanotube (4,0) remains stable and equilibrated well in a configuration similar to the initial structure while nanotubes (6,0), (8,0), and (10,0) collapsed into nanofilaments that acquired shapes different than those obtained from the armchair nanotubes. We refer to these nanofilaments as F60, F80, F100 as a way to identify their original nanotube configuration. The resulting zigzag filaments have a (4,0) tube twinned on the side with other tubes. Figure 7 shows these resulting nanofilament structures, showing that cross sections of filaments F60 and F100 are comparable, namely a (4,0) distorted tube twinned to hexagonal side tubes. On the other hand, filament F80, has intercalated a (2,2) tube intermixing tubes with differnt chirialities. This effect is consistent with structural changes from hexagonal rings into rings of 5 or 7 atoms observed by other researchers in SiC armchair and zigzag nanotubes under thermal and mechanical stresses [17-19,23]. The average potential energy per SiC pair at a zero temperature is -11.4 eV for the (4,0) nanotube, which compares well with the tight binding energy of -10.5 eV [28]. The extrapolated-to-zero-temperature potential energies of the nanofilaments F60, F80, F100 are -11.6, -11.7, and -11.7 eV indicating that these structures are very stable. The prediction is then than nanofilaments are structurally preferred under the potential model used in this work.

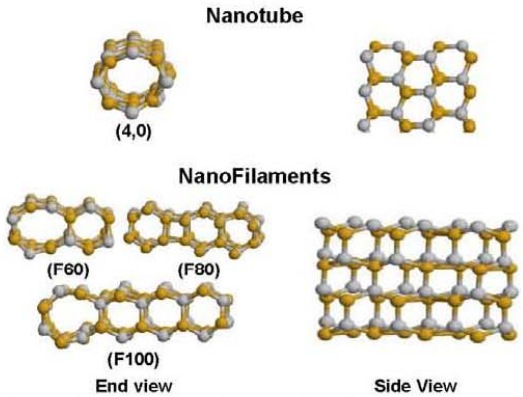

Figure 7. Structure of the SiC (4,0) zigzag nanotube and nanofilaments F60, F80 and F100.

Figure 8 shows the dependence of κ with temperature. The (4,0) nanotube presents a gentle power law behavior as a function of temperature, $\kappa \sim T^{-0.8}$. The decrease in κ due to increasing temperature in the three nanofilaments is quite comparable, smoother than the degradation occurring in the (4,0) nanotubes, and behaving approximately as $T^{-0.65}$. By analyzing Fig. 6 and Fig. 8, one concludes that κ for all nanofilaments behave comparably as a function of temperature.

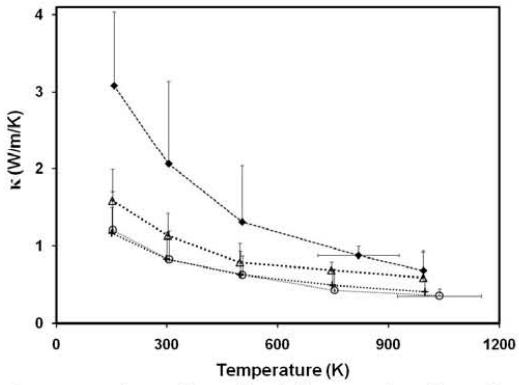

Figure 8. Thermal conductivity as a function of temperature for zigzag nanotube and nanofilaments: nanotube (4,0) (♦), and nanofilaments F60 (Δ), F80 (○), F100 (+). Error bars identify s.d.

4. Conclusions

In this work we have analyzed the temperature dependence of the lattice thermal conductivity for a variety of SiC nanowires, nanotubes, and nanofilaments. Findings show that all of these nanostructures are very poor thermal conductors, showing lattice thermal conductivities two orders of magnitude smaller than bulk values. Additionally, the lattice thermal conductivity dependence with temperature in nanostructures varies greatly with the structure from an inverse-temperature relationship to nearly insensitive-to-temperature variations. This property may be critical to the design and operations of nanodevices and their intended uses in electrical and mechanical applications.

Our results for the lattice thermal conductivity of 3C [$\bar{1}$11] nanowires match closely results published in Ref. [29] that show a basically constant κ in the temperature range 150-1000 K. Additionally, we predict a power law decrease of κ with temperature for the other three nanowires 3C [$\bar{1}$00], 2H [001], and 2H [110]. Our result for κ of nanotube (4,0) is consistent with those obtained for all other nanostructures. However, the value of κ is in disagreement by two orders of magnitude with the prediction of Ref. [30] calculated within the GK approach. Our results show that NEMD techniques can be used to further investigate the κ and thermal response for nanodevices in a reliable fashion.

Acknowledgments

This work was supported in part by the National Science Foundation, grant CHE-0626111.

References

1. D. Srivastava, M. Makeev, M. Menon, and M. Osman, J. Nanoscience and Nanotechnology, 8, 3628 (2008), and references therein

2. D-H. Wang, D. Xu, Q. Wang, Y-J. Hao, G-Q. Jin, X-Y. Guo, K. N. Tu, Nanotechnology 19, 215602 (2008)

3. A. K. Ray and M. N. Huda, J. Comput. Theor. Nanosci. 3, 315 (2006), and references therein.

4. W. Zhou, X. Liu, Y. Zang, Appl. Phys. Lett. 89, 223124 (2006)

5. R. Naslain, J. Lamon, D. Donmeingts, Eds., *High Temperature Ceramic Matrix Composites*, Woodhead, Cambridge, UK, (1993).

6. H. Morkoc, S. Strite, G. B. Gao, M. E. Lin, B. Sverdlov, and M. Burns, J. Appl. Phys. 76, 1363 (1994), and references therein

7. G. Slack, J. Appl. Phys. 35, 3460 (1964)

8. P. Rocco, H. W. Scholz, M. Zucchetti, J. Nucl. Mater., 1474 (1992)

9. R.D. Mountain and R.A. MacDonald, Phys. Rev. B, 28, 3022 (1983)

10. N. Nishiguchi and T. Sakuma, J. Phys.: Cond. Matter, 2, 7575 (1990)

11. J.R. Lukes, D.Y. Li, X.G. Liang, and C.L. Tien, Trans. Am. Soc. Mech. Eng. J. Heat Trans., 122, 536 (2000)

12. K. Imamura, Y. Tanaka, N. Nishiguchi, and H.J. Maris, J. Phys.: Cond. Matter, 15, 8679 (2003)

13. S.R. Phillpot, P.K. Schelling, and P. Keblinski, J. Mat. Sci., 40, 3143 (2005)

14. J.W. Lyver IV and E. Blaisten-Barojas, Acta Materialia, 54, 4633 (2006)

15. A. Maiti, G.D. Mahan, and S.T. Pantelides, Solid State Commun., 102, 517 (2007)

16. J.W. Lyver IV and E. Blaisten-Barojas, J. Phys. Cond. Matt., 21, 345402 (2009)

17. L. Porter, J. Li, and S. Yip, J. Nuclear Mater. 246, 53 (1997)

18. J. Li, L. Porter, S. Yip, J. Nuclear Mater. 255, 139 (1998)

19. J. Rino, I. Ebbsjo, P. Branicio, R. Kalia, A. Nakano, F. Shimojo, and P. Vashishta, Phys. Rev. B, 70, 045207 (2004)

20. P. Vashishta, R. Kalia, A. Nakano, and J. Rino, J. Appl. Phys., 101, 103515 (2007)

21. H-P Chen, R. Kalia, A. Nakano, and P. Vashishta, J. Appl. Phys., 102, 063514 (2007)

22. J. P. Crocombette, G. Dumazer, N. Q. Hoang, F. Gao, and W. Weber, J. App. Phys. 101, 023527 (2007)

23. M. Makeev, D. Srivastava, M. Menon, Phys. Rev. B 74, 165303 (2006)

24. H. Shen, J. Mater. Sci. 42, 6382 (2007)

25. Y. Zhang and H. Huang, Comput. Materials Sci. 43, 664 (2008)

26. J. Tersoff, Phys. Rev. B 39, 5566 (1989)

27. K.M. Alam and A.K. Ray, Phys. Rev. B, 77, 035436 (2008)

28. A. Patrick, X. Dong, T. Allison, and E. Blaisten-Barojas, J. Chem. Phys. 130, 244704 (2009)

29. N. Papanikolaou, J. Phys. Cond. Matt, 20, 135201(2008)

30. H. Shen, Comp. Matl. Sci., 47, 220 (2009)

31. F. Stillinger and T. Weber, Phys. Rev. B, 31, 5262 (1985)

32. R. Balescu, *Equilibrium and Non-Equilibrium Statistical Mechanics*, Wiley, NY (1990) Chap 12

APPENDIX B DEVELOPED COMPUTER CODES

The code provided in this section was developed by the author for the accomplishment of the research presented in this dissertation.

B.1 Lennard-Jones Potential

Calculate the forces between Lennard-Jones atom pairs as described in section 2.2.1.

B.1.1 Annotated Code

```
DO i = 1, N-1                ! Select each pair of atoms
   DO j = I+1, N
      xij = Pos(i,1) - Pos(j,1)
      IF (ABS(xij) .LE. rc) THEN      ! check if within max
distance
         yij = Pos(i,2) - Pos(j,2)
         zij = Pos(i,3) - Pos(j,3)
! Hy is the width of the cubic computational box, Hy2 = Hy/2
         IF (yij .GT. Hy2)  yij = yij – Hy  ! change to
reflection
         IF (yij .LT. -Hy2) yij = yij + Hy
         IF (zij .GT. Hz2)  zij = zij - Hz
         IF (zij .LT. -Hz2) zij = zij + Hz
         rij = SQRT(xij**2.d0 + yij**2.d0 + zij**2.d0)
         IF (rij .LE. rc) THEN
            IF (rij .LE. 0.8d0)  GOTO 902
            SBB = SB(AType(i),AType(j))          ! read σ_AB =
(σ_A+σ_B)/2
            EBB = EB(AType(i),AType(j))          ! read ε_AB = √(ε_A ε_B)
            EBSBB = EBSB(Atype(i),Atype(j))      ! read 24.0* ε_AB / σ_AB^2
            sr6 = (SBB/rij)**6.d0
```

```
            Uij = 2.d0*EBB*sr6*(sr6-1.d0) -
Ushift(AType(i),Atype(j))
            Uatom(i) = Uatom(i) + Uij            ! Potential
energy
            Uatom(j) = Uatom(j) + Uij
            sr1 = EBSBB*(2.d0*((SBB/rij)**14.d0) -
((SBB/rij)**8.d0))
            For(i,1) = For(i,1) + (sr1 * xij)    ! Force on each
atom
            For(i,2) = For(i,2) + (sr1 * yij)
            For(i,3) = For(i,3) + (sr1 * zij)
            For(j,1) = For(j,1) - (sr1 * xij)
            For(j,2) = For(j,2) - (sr1 * yij)
            For(j,3) = For(j,3) - (sr1 * zij)
902         dij = dij                            !  Dummy line
         ENDIF
      ENDIF
   ENDDO
ENDDO
```

B.1.2 Parameters

r_c Force cutoff radius of 48% width of computational cube

B.2 SiC Two-body Potential

Calculates the two-body interaction between atoms in SiC as described in section 2.2.2 as proposed by Vashishta et al. in [8,17].

B.2.1 Annotated Code

```
DO i = 1, N-1          !  Select 1st Atom
   DO j = I+1, N       !  Select 2nd Atom
      xij = Pos(i,1) - Pos(j,1)
                       !  Position of atom in direction X=1, y=2,
z=3
      IF (ABS(xij) .GT. rc) GOTO 999
                       !  pair too far apart, Get new "j" Atom
```

```
      yij = Pos(i,2) - Pos(j,2)
      zij = Pos(i,3) - Pos(j,3)
      rij2 = xij**2.d0 + yij**2.d0 + zij**2.d0
      rij = SQRT(rij2)
      IF (rij .GT. rc) GOTO 999       !  Get new "j" Atom
      rijinv = 1.d0 / rij
      QATij = AType(i) + AType(j)     !  Atom Type C=1 & Si=2
                     !  Find Bond Type: C-C, Si-Si, C-Si
                     !  QV are potential and QF are Force terms
      QV21 = Hij(QATij)*(rijinv**Ada(QATij))
      QF21 = QV21 * Ada(QATij) * rijinv
      QV22 = Qfact1 * Ze(AType(i))*Ze(AType(j)) * rijinv *
&               exp(-rij*lambdainv)
      QF22 = QV22 * (rijinv+lambdainv)
      QV23 = Qfact1 * Dij(QATij) *
&               0.5d0 *(rijinv**4.d0) * exp(-rij*zetainv)
      QF23 = QV23 * ((4.d0*rijinv)+ zetainv)
      QV24 = Wij(QATij) * (rijinv**6.d0)
      QF24 = QV24 * 6.d0 * rijinv
      QV2  = ((QV21 + QV22 - QV23 - QV24 - QVrc(QATij)) -
&               ((rij - rc) * QDVDRrc(QATij)))
                     ! QVrc and QDVDrc are 1st derivatives of
two-body
                       force at the inter-atom distance of rc
      QF2  = (-QF21 - QF22 + QF23 + QF24 - QDVDRrc(QATij))
&               * rijinv
      ETot  = ETot + QV2 + QV2
      PE(i) = PE(i) + QV2
      ForNow(i,1) = ForNow(i,1) - (xij * QF2)
      ForNow(i,2) = ForNow(i,2) - (yij * QF2)
      ForNow(i,3) = ForNow(i,3) - (zij * QF2)
      PE(j) = PE(j) + QV2
      ForNow(J,1) = ForNow(J,1) + (xij * QF2)
      ForNow(J,2) = ForNow(J,2) + (yij * QF2)
      ForNow(J,3) = ForNow(J,3) + (zij * QF2)
      ForIJ(i,j,1) = -xij * QF2  ! force between atomic pair in
x/y/z
      ForIJ(i,j,2) = -yij * QF2
      ForIJ(i,j,3) = -zij * QF2
```

```
      ForIJ(j,i,1) =  xij * QF2
      ForIJ(j,i,2) =  yij * QF2
      ForIJ(j,i,3) =  zij * QF2
912   QF2 = 0.d0                ! dummy line
  ENDDO
ENDDO
```

B.2.2 Parameters

```
Bond parameters are expressed as: C-C/C-Si/Si-Si
Ada  = 7/9/7                (unitless)
Dij  = 0/1.0818/2.1636      (e^2 Å^η)
Hij  = 471.74538/447.09026/23.67291   (ev Å^η)
lambda = 5.0 Å
lambdainv = 1.d0/lambda
rc = 7.35 Å
rcinv = 1.d0 / rc
Wij = 0/61.4694/0         (ev Å^6)
Ze  = -1.201 e
zeta = 3.0 Å
zetainv = 1.d0/zeta
```

B.3 SiC Three-body Potential

Calculates the three-body interaction between atoms in SiC as described in section 2.2.2 as proposed by Vashishta et al. in [8,17].

B.3.1 Annotated Code

```
DO i = 1, N
   DO j = 1, N-1
      IF (atype(i) .EQ. atype(j)) GOTO 910
      DO k = j+1, N
         IF (atype(i) .EQ. atype(k)) GOTO 911
         xij = Pos(i,1) - Pos(j,1)
         IF (ABS(xij) .GT. r0) GOTO 910  !  Get new "j" Atom
```

```
            yij = Pos(i,2) - Pos(j,2)
            zij = Pos(i,3) - Pos(j,3)
            rij2 = xij**2.d0 + yij**2.d0 + zij**2.d0
            rij = SQRT(rij2)
            IF (rij .GT. r0) GOTO 910  !  Get new "j" Atom
            rijinv  = 1.d0 / rij
            xik = (Pos(i,1) - Pos(k,1))
            IF (ABS(xik) .GT. r0) GOTO 911  !  Get new "k" Atom
            yik = (Pos(i,2) - Pos(k,2))
            zik = (Pos(i,3) - Pos(k,3))
            rik2 = xik**2.d0 + yik**2.d0 + zik**2.d0
            rik = SQRT(rik2)
            IF (rik .GE. r0) GOTO 911  !  Get new "K" Atom
            rikinv  = 1.d0 / rik
            rijkinv  = rijinv  * rikinv
            rijk2inv = rij2inv * rik2inv
            xjk = (Pos(j,1) - Pos(k,1))
            yjk = (Pos(j,2) - Pos(k,2))
            zjk = (Pos(j,3) - Pos(k,3))
            rjk2 = xjk**2.d0 + yjk**2.d0 + zjk**2.d0
            rjk = SQRT(rjk2)
            rjkinv = 1.d0/rjk

            COSijk = 0.5d0 *(rij2 + rik2 - rjk2) * rijinv*rikinv
            CosCos = Cosijk - Cos109
            CosCos2 = CosCos * CosCos
            DPDCOS = (2.d0 * CosCos) /
     &                ((1.d0 + (Cijk * CosCos2))**2.d0)
            Pijk   = CosCos2 / (1.d0 + (Cijk * CosCos2))
            Rijk  = Bijk * dexp(1.d0/(rij-r0)) *
     &                dexp(1.d0/(rik-r0))
            RGP = -Rijk * gamma * Pijk
            DRijinv = 1.d0 / (rij * ((rij-r0)**2.d0))
            DRikinv = 1.d0 / (rik * ((rik-r0)**2.d0))
            RoverR = -rjk * rijinv * rikinv

            QRP = Rijk * pijk * 0.3333333333d0
            PE(i) = PE(i) + QRP
```

```
          PE(j) = PE(j) + QRP
          PE(k) = PE(k) + QRP
          Forijk = - (RGP* (drijinv*xij + drikinv*xik))
     &               - Rijk * DPDCOS *
     &               (((rikinv - (rijinv * cosijk)) * xij*rijinv) +
     &               ((rijinv - (rikinv * cosijk)) * xik*rikinv))
          ForIJ(i,j,1) = ForIJ(i,j,1) + (Forijk * 0.5d0)
          ForIJ(i,k,1) = ForIJ(i,k,1) + (Forijk * 0.5d0)
          Forijk = - (RGP* (drijinv*yij + drikinv*yik))
     &               - Rijk * DPDCOS *
     &               (((rikinv - (rijinv * cosijk)) * yij*rijinv)+
     &               ((rijinv - (rikinv * cosijk))*yik*rikinv))
          ForIJ(i,j,2) = ForIJ(i,j,2) + (Forijk * 0.5d0)
          ForIJ(i,k,2) = ForIJ(i,k,2) + (Forijk * 0.5d0)
          Forijk = - (RGP* (drijinv*zij + drikinv*zik))
     &               - Rijk * DPDCOS *
     &               (((rikinv - (rijinv * cosijk)) * zij*rijinv)+
     &               ((rijinv - (rikinv * cosijk)) * zik*rikinv))
          ForIJ(i,j,3) = ForIJ(i,j,3) + (Forijk * 0.5d0)
          ForIJ(i,k,3) = ForIJ(i,k,3) + (Forijk * 0.5d0)
          ForIJ(j,i,1) = ForIJ(j,i,1) - (RGP* (-drijinv*xij))
     &               - Rijk * DPDCOS *
     &               ((-(rikinv - (rijinv * cosijk)) * xij*rijinv) +
     &                 (RoverR * xjk * rjkinv))
          ForIJ(j,i,2) = ForIJ(j,i,2) - (RGP* (-drijinv*yij))
     &               - Rijk * DPDCOS *
     &               ((-(rikinv - (rijinv * cosijk)) *yij*rijinv)+
     &               ( RoverR * yjk * rjkinv))
          ForIJ(j,i,3) = ForIJ(j,i,3) - (RGP* (-drijinv*zij))
     &               - Rijk * DPDCOS *
     &               ((-(rikinv - (rijinv * cosijk)) * zij*rijinv)+
     &               ( RoverR * zjk * rjkinv))
          ForIJ(k,i,1) = ForIJ(k,i,1) - (RGP* (-drikinv*xik))
     &               - Rijk * DPDCOS *
     &               ((-(rijinv - (rikinv * cosijk)) * xik*rikinv)+
     &                 (-RoverR * xjk * rjkinv))
          ForIJ(k,i,2) = ForIJ(k,i,2) - (RGP* (-drikinv*yik))
     &               - Rijk * DPDCOS *
```

```
&                ((-(rijinv - (rikinv * cosijk)) * yik*rikinv)+
&                (-RoverR * yjk * rjkinv))
         ForIJ(k,i,3) = ForIJ(k,i,3) - (RGP* (-drikinv*zik))
&                - Rijk * DPDCOS *
&                ((-(rijinv - (rikinv * cosijk)) * zik*rikinv)+
&                (-RoverR * zjk * rjkinv))
911      Xij = 0.d0   !  Need a new "K" atom
      ENDDO
910   Xij = 0.d0   !  Need a new "J" atom
   ENDDO
ENDDO
```

B.3.2 Parameters

```
Bijk = 9.003 ev
Cijk = 5.0                    (unitless)
COS109 = Cosine of 109°
gamma =  1.0Å
r0 = 2.9 Å
```

B.4 Determination of Heat Current:

Calculates the heat current in each slice of the computational box as described in section 2.6.2 with the following microscopic expression [13,23,29-31]:

$$J_\alpha(r,p) = \sum_{i=1}^{N}\left[\frac{p^2}{2m_i} + \frac{1}{2}\sum_{j\neq i}^{N} u(r_{ij})\right]\left(\frac{p_{i\alpha}}{m_i}\right) + \frac{1}{2}\sum_{i=1}^{N}\sum_{j\neq i}^{N}\left[\left(\frac{\vec{p}_i}{m_i}\right)\cdot F_{ij}\right] r_{ij\alpha} \qquad (38)$$

where α = x,y,z, the p_i are the momenta of atoms with mass m_i, $u(r_{ij})$ are the interatomic potential energies, and F_{ij} are the forces between atoms i and j.

B.4.1 Annotated Code

```
DO i = 1, N                  !  Select 1st atom
   AS = ASlice(i)            !  1st atom's slice in the system
   KE = 0.5d0 * mass(Atype(i)) * ((Vel(i,1)**2.d0) +
```

```
&       (Vel(i,2)**2.d0) + (Vel(i,3)**2.d0)) * Qfact3
            ! Qfact3 is a unit conversion of:  eV to kg Å²/s²
   T(AS) = T(AS) + KE       !  Temperature of the slice
                    !  Calculate the 1st term, PE is Potential
Energy
   Jx(AS) = Jx(AS) + ((KE + PE(i)) * vel(i,1))     ! Units: eV Å/s
   Jy(AS) = Jy(AS) + ((KE + PE(i)) * vel(i,2))
   Jz(AS) = Jz(AS) + ((KE + PE(i)) * vel(i,3))
   DO j = 1, N              !  Select 2nd atom
      IF (i .NE. J) THEN
         xij = Pos(i,1) - Pos(j,1)
         yij = Pos(i,2) - Pos(j,2)
         zij = Pos(i,3) - Pos(j,3)
         rij = SQRT(xij**2.d0 + yij**2.d0 + zij**2.d0)
!  Calculate the 2nd term, ForIJ(I,j,α) is the force of atom j on
atom i in the α direction
         Jtemp = 0.5d0 * ((vel(i,1) * ForIJ(i,j,1)) +
&                (vel(i,2) * ForIJ(i,j,2)) +
&                (vel(i,3) * ForIJ(i,j,3)))
         Jx(AS) = Jx(AS) + (JTemp * xij)
         Jy(AS) = Jy(AS) + (JTemp * yij)
         Jz(AS) = Jz(AS) + (JTemp * zij)
      ENDIF
914   xij = 0.d0
   ENDDO
913  xij = 0.d0
ENDDO
Jx = Jx * 0.25d0            !  ¼ factors
Jy = Jy * 0.25d0
Jz = Jz * 0.25d0
```

B.4.2 Parameters

Qfact3 = $0.062415 \frac{kg\,Å^2}{eV\,s^2}$ units conversion

B.5 Calculation of Autocorrelation and Density of States

Calculated the autocorrelation of the velocity in each direction, averaged them and then took the Fourier Transform to determine the density of states as described in section 2.6.1. Normally the vibrational data was taken as 10 time segments (or trials) in calculating the Autocorrelation. The FFT routine was adapted from [74].

B.5.1 Annotated Code

```
DO k = 1, 3                  ! Each direction
   LongC = 0.d0
   C1 = 0.d0
   DO I = 1, N
      Data = 0.d0
      AData = 0.d0
      DO NS = 0, VibrTrial-1     ! Trial number
         DO j = 1, NSize2
!  Nsize is the number of steps, Nsize2 is double the number
!  StepsVibr si the number of stored steps of data
!  Vibr is the array holding the velocity data
            Data(j) = Vibr((NS*(StepsVibr-
NSize)/VibrTrial)+j,i,k)
         ENDDO
         CALL Auto(Data, NSize, AData)  !  Autocorrelation
Subroutine
!  Data is the input raw vibrational data, AData is the output
Autocorrelation
         DO j = 1, NSize
            LongC(j) = LongC(j) + AData(j)  ! average over trials
         ENDDO
      ENDDO
   ENDDO
   LongC = LongC / VibrTrial / AtomsAC
                     !  AtomsAC is number of atoms
   DO I = 1, NSize
```

```
      C1(i+i-1) = LongC(i)       !  convert to complex number
array
   ENDDO
   CALL FFT(C1, NSize, Isign)    !  Fourier transformation
subroutine
                    ! with NSize2 pairs of data elements
967  I = 1
ENDDO
```

```
SUBROUTINE Auto (Data, NSize, C)
   INTEGER NSize, NSize2, T, Tau
   REAL*8  AvgC0, C0, C(20000), Data(20000)

! ------------  Calculate C0 ----------------
   NSize2 = NSize * 2.d0       ! Nsize is the # items in output
   C0 = 0.d0
   DO T = 1, NSize2
      C0 = C0 + Data(T)*Data(T)
   ENDDO
   C0 = C0 / NSize2
! ----------------  Calculate C(τ)  ------------------
   C  = 0.d0
   DO Tau = 1, Nsize
      DO T = 1, Nsize2 - Tau
         C(Tau+1) = C(Tau+1) + Data(T)*Data(T+Tau)
      ENDDO
      C(Tau+1) = C(Tau+1) / (NSize2 - Tau)
   ENDDO
   C = C / C0
   C(1) = 1.d0

   RETURN
   END

SUBROUTINE FFT(Data, NN, Isign)
!  data is old fashion Complex vector of [r I r I r I r I . ...]
!       with NN pairs of data elements
```

```
!  Isign is 1 for an FFT and -1 for an Inverse FFT

   INTEGER  i, Isign, Istep, j, m, N, NN, Mmax
   REAL*8  TempI, TempR, WR, WI, WPR, WPI, WTEMP, THETA
   REAL*8  Data(66000)

   N = 2 * NN        ! length of Data array of NN complex ele
   j = 1
   DO i = 1, N, 2
      IF (j .GT. i) THEN
         TempR = Data(j)
         TempI = Data(j+1)
         Data(j) = Data(i)
         Data(j+1) = Data(i+1)
         Data(i) = TempR
         Data(i+1) = TempI
      ENDIF
      m = NN
101   IF ((m .GE. 2) .AND. (j .GT. m)) THEN
         j = j - m
         m = m/2
         GOTO 101
      ENDIF
      j = j + m
   ENDDO
         ! Begin the Danielson-Lanczos section of the routine
   Mmax = 2
102  IF (N .GT. Mmax) THEN   ! Outer loop executes log2(NN) times
      Istep = 2 * Mmax
      Theta = 6.28318530717959d0 / (Isign * Mmax)
      WPR = -2.d0 * SIN(0.5d0 * Theta)**2.d0
      WPI = SIN(Theta)
      WR = 1.d0
      WI = 0.d0
      DO M = 1, Mmax, 2
         DO i = m, n, Istep
            j = i + Mmax     ! Danielson-Lanczos formula
            TempR = WR * Data(j) - WI * Data(j+1)
```

```
            TempI = WR * Data(j+1) + WI * Data(j)
            Data(j) = Data(i) - TempR
            Data(j+1) = Data(i+1) - TempI
            Data(i) = Data(i) + TempR
            Data(I+1) = Data(i+1) + TempI
         ENDDO
         Wtemp = WR          !  Trigonometric recurrence
         WR = WR * WPR - WI * WPI + WR
         WI = WI * WPR + Wtemp * WPI + WI
      ENDDO
      Mmax = Istep
      GOTO 102
   ENDIF

   RETURN
   END
```

B.5.2 Parameters

None

B.6 Maintain Constant Temperature in Thermal Baths

This routine reset the temperature within each thermal bath back to the set temperature.

This is only a section of the routine for a single bath.

B.6.1 Annotated Code

```
KE0 = 0.d0                  ! Kinetic Energy of Bath
DO i = 1, N
   KE0 = KE0 + (mass(Atype(i)) * ((Vel(i,1)**2.d0) +
&              (Vel(i,2)**2.d0) + (Vel(i,3)**2.d0)))
   AtomCount = AtomCount + 1     !  count number of atoms
```

```
ENDDO
KE0 = KE0 * 0.5d0 * qfact5 / AtomCount
                              ! Qfact5 is a unit conversion
Tfactor = (Tmid / KE0)**0.5d0          ! Tmid is the Bath
Temperature
Vel = Vel * Tfactor
```

B.6.2 Parameters

Qfact5 = > 724.2713 Kelvin = $1\frac{eV}{s\ \text{Å}^2}$

BIBLIOGRAPHY

BIBLIOGRAPHY

[1] Lukes JR, Li DY, Liang XG, and Tien CL, Trans. Am. Soc. Mech. Eng. J Heat Trans., **122** (2000) 536

[2] Feng X-L, Li Z-X, Guo Z-Y, Chin. Phys. Lett., **18** (2000) 416–9

[3] McGaughey AJH, Kaviany M, Int J Heat Mass. Transf., **47** (2004) 1783–98

[4] Chen Y, Li D, Yang J, Wu Y, and Lukes JR, Physica B, **349** (2004) 270

[5] Heino P, Phys. Rev. B, **71** (2005) 144302

[6] Berman R, *Thermal Conduction in Solids,* Clarendon Press, Oxford (1976)

[7] Jonson M, and Mahan GD, Phys. Rev. B, **21** (1980) 4223–9

[8] Vashishta P, Kalia R, Nakano A, and Rino J, J Appl. Phys., **101** (2007) 103515

[9] Lyver JW and Blaisten-Barojas E, Acta Materialia, **54** (2006) 4633

[10] Lyver JW and Blaisten-Barojas E, J Phys. Cond. Matt., **21** (2009) 345402

[11] Lyver JW and Blaisten-Barojas, *publication pending*

[12] Frenkel D, and Smit B, *Understanding Molecular Simulation,* Academic Press, New York (1998)

[13] McQuarrie DA, *Statistical Mechanics*, Harper Collins, NY, (1973), Ch. 17 and 21

[14] Haile JM, *Molecular Dynamics Simulations*, J Wiley, NY (1992)

[15] Verlet L, Phys. Rev., **159** (1967) 98

[16] Stillinger F and Weber T, Phys. Rev. B, **31** (1985) 5262

[17] Keating P, Phys. Rev., **145** (1966) 637

[18] Rino J, Ebbsjo I, Branicio P, Kalia R, Nakano A, Shimojo F, and Vashishta P, Phys. Rev. B, **70** (2004) 045207

[19] Inavshchenko V, Turchi P, Shevchenko V, Ivashchenko L, and Rusakov G, Dia. and Rel. Mat., **12** (2003) 993

[20] Patrick A, Dong X, Allison T, and Blaisten-Barojas E, J Chem. Phys., **130** (2009) 244704

[21] Alam KM and Ray AK, Phys. Rev. B, **77** (2008) 035436

[22] Green MS, J Chem Phys, **20** (1952) 1281–95; Green MS, J Chem. Phys., **22** (1954) 398

[23] Kubo R, J Phys. Soc. Jpn., **12** (1957) 570–86

[24] Ladd AJC, Moran B, and Hoover WG, Phys. Rev. B, **34**(8) (1986) 5058

[25] Tretiakov KV, and Scandolo S, J Chem. Phys. **120** (2004) 3765–9

[26] Gaigeot MP, Vuilleumier R, Sprik M, and Borgis D., J Chem. Theory and Comp., **1** (2005) 772-789

[27] Gillan MJ, J Phys C: Condens. Matter, **20** (1987) 521–38

[28] Chen Y, Lukes JR, Yang J, and Wu Y. J Chem. Phys., **120** (2004) 3841–6

[29] Mori H, Phys. Rev., **112** (1958) 1829

[30] Balescu R, *Equilibrium and Non-Equilibrium Statistical Mechanics*, Wiley, NY (1990) Ch. 12 and 21

[31] Schofield P, Proc. Phys. Soc., **88** (1966) 149

[32] Mountain RD, and MacDonald RA, Phys. Rev. B, **28** (1983) 3022

[33] Pan R, Xu Z, Zhu Z, and Wang Z, Nanotechnology **12** (2007) 285704

[34] *CRC Handbook of Thermoelectrics*, Introduction, Edited by D.M. Rowe, CRC Press, (1995)

[35] Garzon IL, Long XP, Kawai R, and Weare JH. Chem. Phys. Lett., **158** (1989) 525–30

[36] Kaburaki H, Li J, and Yip S, Matter Res. Soc. Symp. Proc., **538** (1998) 503–8

[37] Christen DK, and Pollack GL, Phys. Rev. B, 12 (1975) 3380–91

[38] Li J, Porter L, and Yip S, J Nucl. Mater, **255** (1998) 139–52

[39] Kapitza PL, J Phys. USSR, **4** (1941) 181

[40] Khalatnikov IM, J Exp. Theoret. Phys, **22** (1952) 687

[41] Swartz ET and Pohl RO, Rev. Mod. Phys., **61** (1989) 605

[42] Lumpkin ME, Saslow WM, and Visscher WM, Phys. Rev. B, **17** (1978) 4295

[43] Schelling PK, Phillpot SP, and Keblinski P, J Appl. Phys., **95** (2004) 6082

[44] Liang X-G and Shi B, Mat. Sci. and Engr. A, **292** (2000) 198

[45] Young DA, Thomsen C, Grahn HT, Maris HJ, and Tauc J, *Phonon Scattering in Condensed Matter*, Springer, Berlin (1986) Ch. 49

[46] Stoner RJ and Maris HJ, Phys. Rev. B, **48** (1993) 16373

[47] Chen H-P, Kalia R, Nakano A, and Vashishta P, J Appl. Phys., **102** (2007) 063514; Chen G, Tien CL, Wu X, and Smith JS, J Heat Transfer, **116** (1994) 325

[48] Matsumoto M, Wakabayashi H, and Makino T, Heat Transfer – Asian Rsrch., **34** (2005) 135

[49] Liang X-G, and Sun L, Microscale Thermophysical Engr., **9** (2005) 295

[50] Nishiguchi N, and Sakuma T, J Phys.: Cond. Matter, **2** (1990) 7575

[51] Imamura K, Tanaka Y, Nishiguchi N, and Maris HJ, J Phys.: Cond. Matter, **15** (2003) 8679

[52] Phillpot SR, Schelling T, and Keblinski P, J Mat. Sci., **40** (2005) 3143

[53] Maiti A, Mahan GD, and Pantelides ST, Solid State Comm., **102** (2007) 517

[54] Twu C-J, and Ho J-R, Phys. Rev. B, **67** (2002) 205422

[55] Chantrenne P, and Barrat JL, J Heat Trans., **126** (2004) 577

[56] Amrit J, J Phys. D: Appl. Phys., **39** (2006) 4472

[57] Stevens RJ, Zhigilei LV, and Norris PM, Int. J Heat Mass Transfer, **50** (2007) 3977

[58] Barrat JL, and Chiaruttini F, Mol. Phys., **101** (2003) 1605

[59] Dickey JM, and Paskin A, Phys. Rev., **188**(3) (1969) 1407

[60] Grindley J, and Howard R, edited by Wallis RF, *Lattice Dynamics*, Pergamon Press, NY (1965)

[61] Srivastava D, Makeev M, Menon M, and Osman M, J Nanoscience and Nanotechnology, **8** (2007) 1

[62] Zhong Z, Wang X, and Xu J, Num. Heat Trans. Part B, **46** (2004) 429

[63] Dresselhaus MS, Dresselhous G, and Avouris PH, *Carbon Nanotubes-Synthesis,Structure, Properties, and Applications*, Topics in Applied Physics Vol. 80, Springer, Berlin (2001)

[64] Srivastava D, Menon M, and Cho K, Phys. Rev. Lett., **83** (1999) 2973

[65] Mylvaganam K, and Zhang L, Carbon, **42** (2004) 2025

[66] Thostenson E, Ren Z, and Chou T-W, Comp. Sci. and Tech., **61** (2001) 1899

[67] Berber S, Kwon Y-K, and Tomănek D, Phys. Rev. Lett., **84** (2000) 4613

[68] Papanikolaou N, J Phys. Cond. Matt., **20** (2008) 135201

[69] Halicioglu T, Phys. Rev. B, **51** (1995) 2717

[70] Slack G, J Appl. Phys, **35** (1964) 3460

[71] Shen H, Comp. Matl. Sci., **47** (2009) 220

[72] Alder BJ, and van Thiel M, Phys. Letters, **7** (1963) 317

[73] Theodorou DN, and Suter UW, J Chem. Phys., **82**, (1985) 955

[74] Berne BJ, and Harp GD, Adv. Chem. Phys., **17** (1970) 63 and 130-132

[75] *Numerical Recipes: The Art of Scientific Computing*, Third Edition, Cambridge University Press (2007)

[76] Webpage for Portland Group, Inc's, PGI Workstation®: http://www.pgroup.com/products/pgiworkstation.htm

[77] Webpage for GMU Bach: http://www.scs.gmu.edu/bach/

[78] Webpage for the OpenMP Application Program Interface (API) support group: http://openmp.org/wp/about-openmp/

[79] Website for RasMol and RasWin: http://rasmol.org/

CURRICULUM VITAE

John W. Lyver, IV graduated from Lower Merion High School, Ardmore, Pennsylvania, in 1974. He received his Bachelors of Science from the United States Naval Academy in 1978. He is employed by the National Aeronautics and Space Administration and is retired from the United States Navy. He received a Master of Science in Computers and Electronic Engineering from George Mason University in 1988, and a Master of Science in Computational Science and Informatics in 2008. He is a licensed Certified Safety Professional in Systems Safety.